UNIVERSITY of HULL

Proceedings SimBio-M 2024

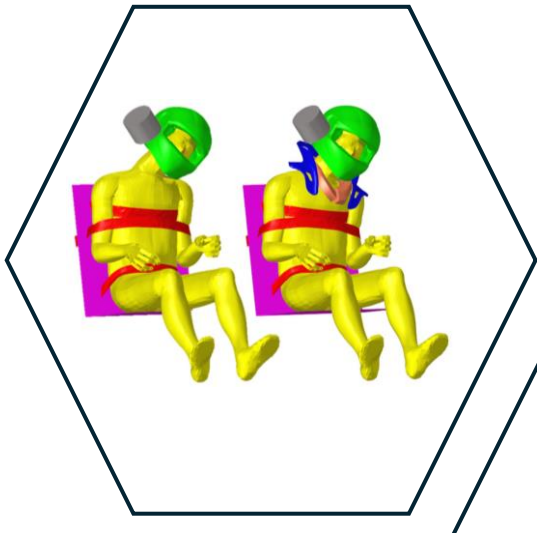

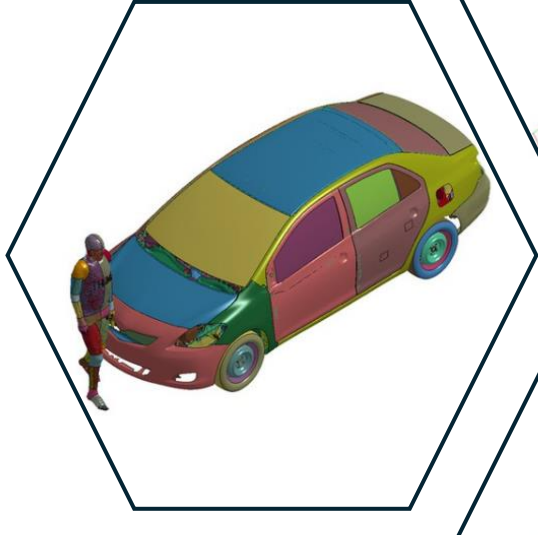

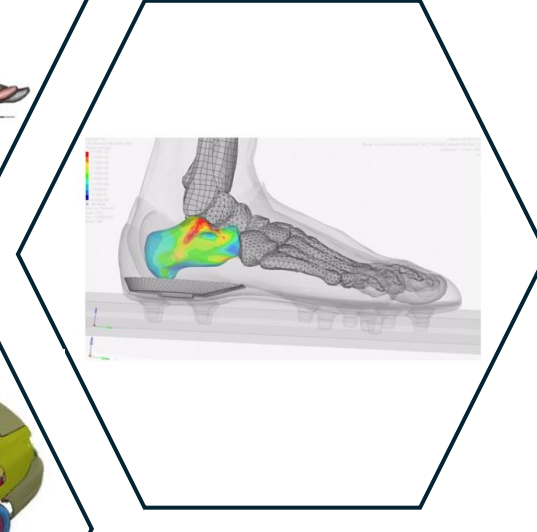

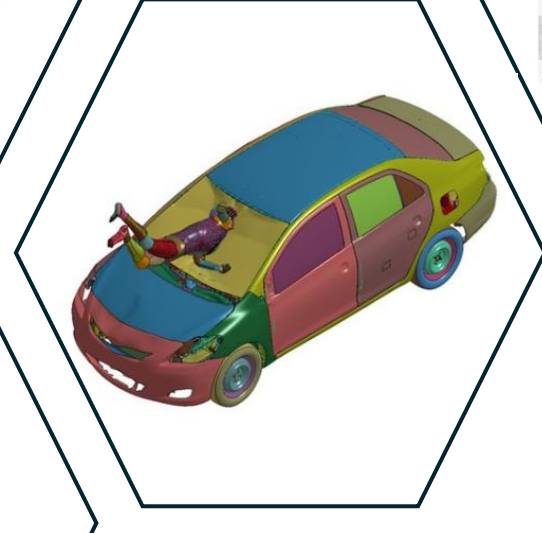

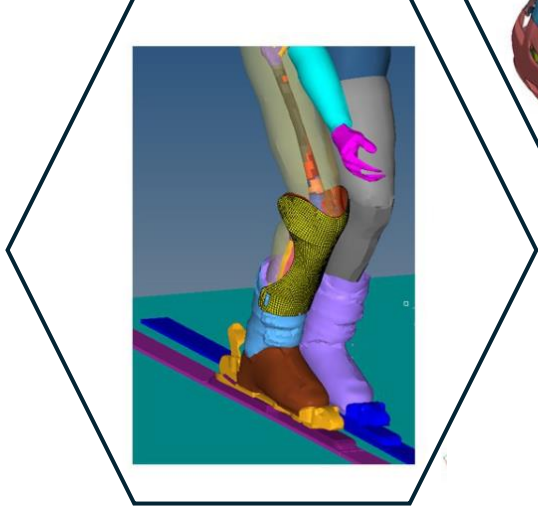

Simulation in **Bio**sciences
-**M**ultiphysics
-**M**echanics
-**M**aterials
-**M**edicine
-**M**anufacturing

Coventry University

Université Gustave Eiffel

Aix*Marseille université
Socialement engagée

Proceedings SimBio-M 2024

Cottingham Road,
Kingston upon Hull
HU6 7RX, UK
https://www.hull.ac.uk/

ISBN - 978-1-906422-44-8

Proceedings SimBio-M 2024

Keynote Speakers

Prof Jörg Fehr (University of Stuttgart)

"Active Human Models for the Assessment of Injury Patterns in Whiplash Trauma: Simulation and Experiment".

Prof Gianluca Tozzi (University of Greenwich)

"Advances in imaging-based measurements and artificial intelligence for the characterisation of musculoskeletal tissues and biomaterials"

Modeling the Best Cancer Therapeutics - The Artificial Intelligence Pathway

Aimee Pascaline N Unkundiye[1], Gillian Pearce[2], Amit K Chattopadhyay[1]

[1]*Aston University, Dept of Applied Mathematics and Data Science, Birmingham, B4 7ET;*

[2]*Aston University, College of Engineering and Physical Sciences, Birmingham, B4 7ET;*

ABSTRACT

This study explores the application of artificial intelligence (AI) modeling to predict and develop personalized treatment strategies for targeted chemotherapy and radiation therapy in the treatment of cancerous tumors. The research evaluates the efficacy of fluorodeoxyglycose coated magnetic nanoparticles (Fe3O4-mNP) as a cancer treatment modality, in comparison to traditional therapies like saline treatment and magnetic nanoparticles (mNPs). Modeling computationally extracted (synthetic) data from previous experimental studies on MAC-16 tumor-bearing mice, we combined predictions from three Machine Learning models (Decision Trees, Random Forest, Multilinear Regression) with a Deep Learning model (Adaptive Neural Network), to identify the best containment regimen for cancerous tumors. Our results show that Fe3O4-mNP treatment significantly reduces tumor volume and demonstrates superior tumor control compared to standard chemotherapy. Among the models, the adaptive neural network showed the highest predictive precision (R^2 = 0.9908), outperforming the others in tracking tumor dynamics through the logistic growth and exponential decay phases. These results suggest that mNP-based therapies offer a promising, targeted alternative to traditional chemotherapy, with reduced side effects and substantially reduced resistance to therapeutics.

Keywords: Artificial Intelligence, Magnetic Nanoparticles, Tumor Growth Prediction, Personalized Treatment, Cancer Therapy, Deep Learning

INTRODUCTION

The emergence of AI and advanced mathematical models has opened new avenues for personalized medicine, particularly in the field of cancer treatment. Over the years, substantial progress has been made in understanding the mechanisms underlying tumor growth and response to treatment. However, Cancerous tumors remain a major global health [1] concern with recent estimates indicating that 1 in 2 people will develop cancer at some point in their lives, as reported by the Cancer Research UK in 2024 [2]. Despite advances in traditional cancer therapies such as chemotherapy, radiotherapy, and immunotherapy, these treatments are often accompanied by significant limitations [3, 4]. Common limitations include severe side effects, drug resistance, and variability in efficacy over different forms of cancer. Also, during surgical removal of a tumor, a margin of normal cells around the tumor is always removed since tumor cells can infiltrate and spread into surrounding tissues. However, this can also lead to the destruction of healthy tissue.

This highlights the urgent need for more targeted and less invasive therapies that can overcome these challenges and improve patient outcomes [5, 6]. Recent research has focused on the development of nanoparticle-based cancer treatments, which offer the potential to enhance drug concentration within tumors and simultaneously reduce their side effects [7]. The key to effective treatment lies in minimizing uptake by non-target cells and reducing the rapid clearance of therapeutic agents by the kidneys. Together, these factors extend the lifetime of the agents in circulation and accelerate their accumulation in solid tumors.

Our research focuses on uncoated iron oxide magnetic nanoparticles Fe3O4-mNP [1, 8], which have shown promise due to their magnetic properties and ability to be directed toward specific areas of the body. Fe3O4-mNP can selectively target cancer cells while preserving healthy tissue, offering a

more precise and potentially more effective treatment option. Although healthy cells may also absorb sugar coated nanoparticles Fe3O4-mNP, cancerous cells exhibit significantly faster and higher levels of uptake, thus maximizing therapeutic efficacy while minimizing collateral damage. Furthermore, by directly injecting these nanoparticles into the tumor, the risk of spreading to surrounding healthy tissue is minimized.

This study aims to evaluate the therapeutic potential of Fe3O4-mNP as cancer treatments. Specifically, we assess whether Fe3O4-mNP can indeed address the limitations associated with traditional therapies by providing a targeted and minimally invasive approach that reduces tumor size while preserving healthy tissue. Through the use of Artificial Intelligence (AI) driven predictive models, researchers will analyze tumozr growth and decay dynamics to understand how nanoparticle-based therapies impact tumor progression over time. By comparing the efficacy of these nanoparticles with saline treatment regimens, the study will provide valuable insight in identifying the more potent treatment and its potential as a viable cancer treatment option.

Ultimately, this study is significant as it explores noninvasive, personalized treatments that could revolutionize cancer therapy by improving patient outcomes while minimizing side effects. By integrating machine learning and deep learning models, we aim to accurately predict tumor shrinkage timelines and the efficacy of different treatments, pushing the boundaries of cancer therapy.

MATERIALS & METHODS

Experimental procedures across previously reported studies, specifically those conducted by Zhu, et al, Hay, et al and Chattopadhyay, et al [1, 9, 10], involved intratumural injection of nanoparticles in varying doses, followed by regular tumor volume measurements. The modeling study [1] essentially data modeled the experimental outcomes from the other two studies, comparing the evolution of the tumor volume to understand the efficacy of the respective treatment forms.

Machine Learning models Decision Trees (DT), Random Forests (RF), Multilinear Regression (MLR), and a Deep Learning model in the form of the Adaptive Neural Network (ANN) were trained to predict tumor growth and response to treatment using these data points. Statistical analyzes were conducted using self-written codes in MATLAB and Python, focusing on two tumor growth phases - the logistic growth and exponential decay models. This inherently computational study as also its earlier counterpart in Chattopadhyay2024 have only used proportional synthetic data that were computationally generated scanning the experimental data plots, thus adhering to ethical governance throughout.

RESULTS AND DISCUSSION

The experimental data revealed significant differences in tumor progression among different treatment groups. Specifically, untreated tumors exhibited continuous growth, while saline-treated tumors showed slower progression.

In contrast, tumors treated with Fe3O4-mNPs demonstrated substantial volume reduction over time, highlighting the potential efficacy of Fe3O4-mNPs.

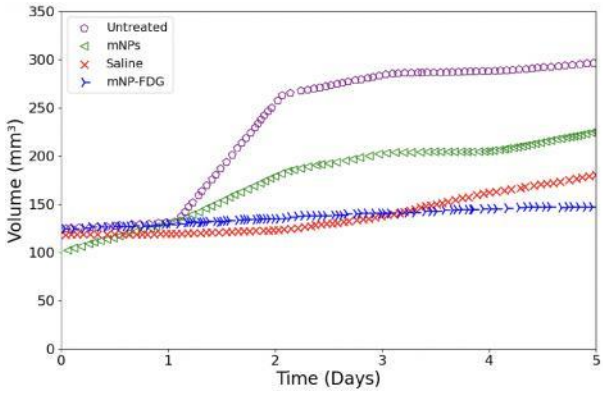

(a) Tumour volume progression over 5 days under various treatments by Chattopadhyay et al. [1].

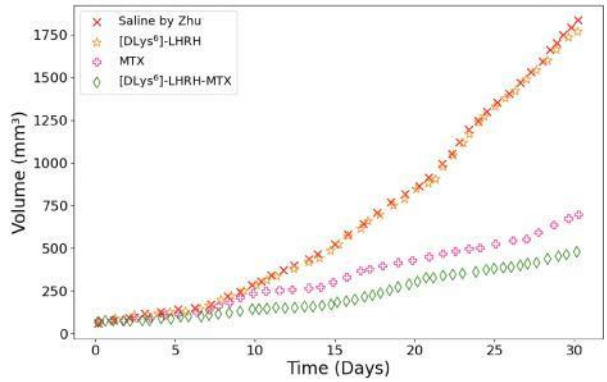

(b) Tumour volume response under progression under various treatments by Zhu et al. [10].

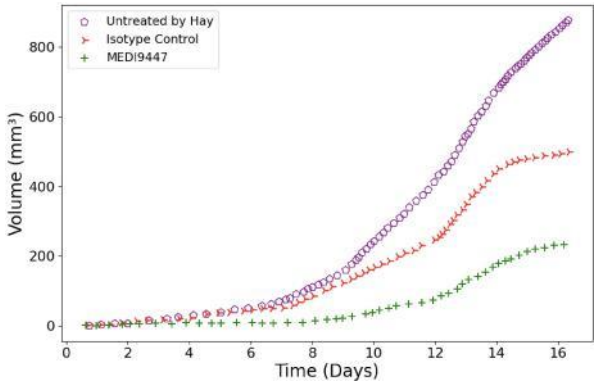

(c) Tumour volume progression under various treatments by Hay et al. [9].

FIG. 1: Time evolution of tumor volumes under various treatment protocols, with data extracted using Grabit from MATLAB [1, 9, 10].

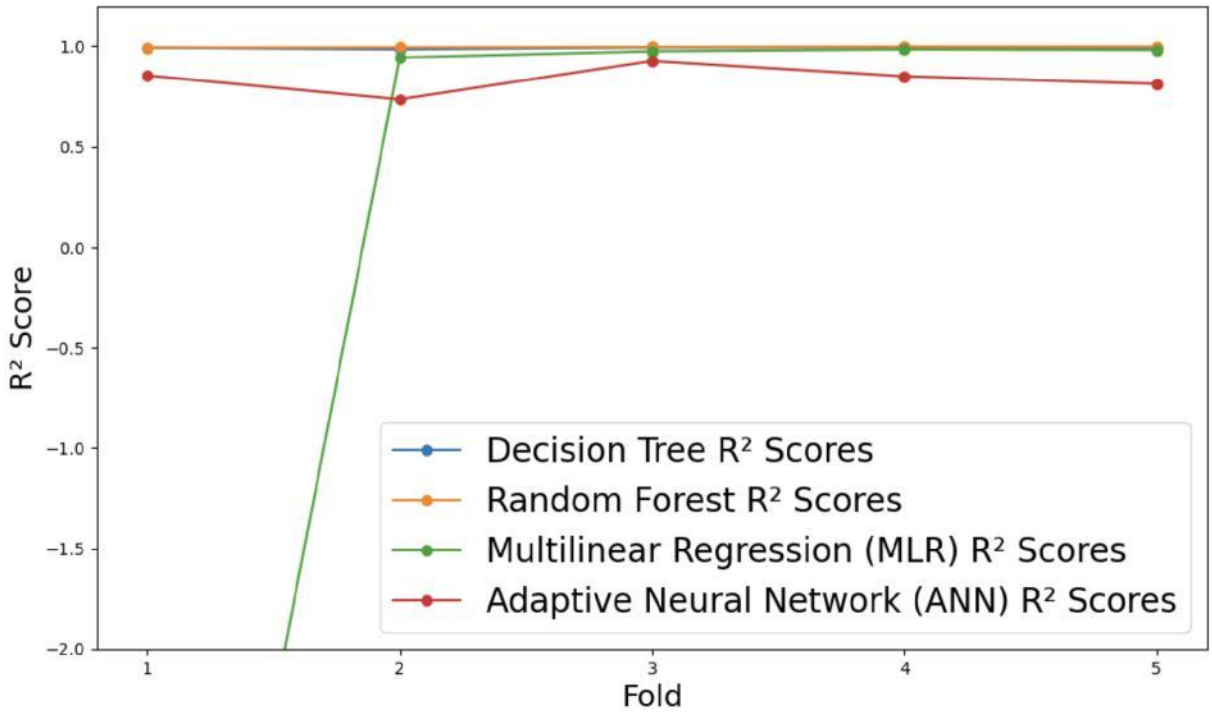

FIG. 2: Cross-validation of model accuracy: Comparison of predictive performance across machine learning models in tumor volume analysis.

Among the predictive models tested, the Adaptive Neural Network (ANN) displayed the highest accuracy, achieving an R^2 = 0.9908 and RMSE of 4.02, effectively capturing both the logistic growth and exponential decay phases of tumor progression. In contrast, the Decision Tree (DT) model had the lowest accuracy, with R2 = 0.8495 and RMSE = 16.26, demonstrating a propensity for overfitting. The Multilinear Regression (MLR) model initially underfit and then overfit the data, impacting its predictive reliability.

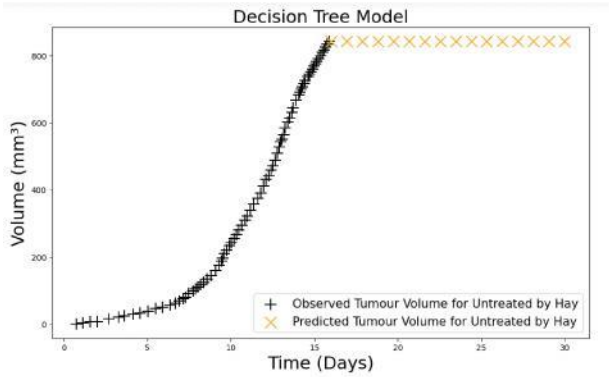

(a) Decision Tree predictions

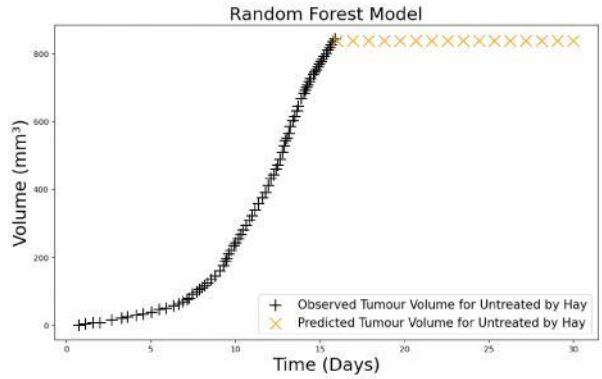

(b) Random Forest predictions

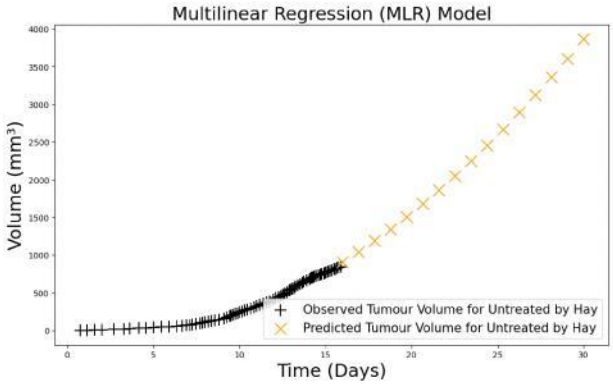

(c) Multilinear Regression model predictions

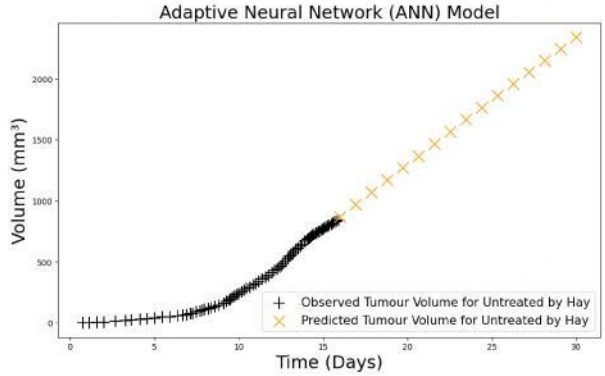

(d) Adaptive Neural Network Model predictions

FIG. 3: Comparison of model predictions for untreated tumor volume growth, based on data from Hay et al [9]

As shown in Figure 3d, which presents the predicted tumor growth using ANN model, a disconnect is observed around day 12-13. This deviation may be attributed to the model's sensitivity to initial conditions or the inherent variability in tumor growth dynamics, which may not have been fully captured in the early stages of prediction.

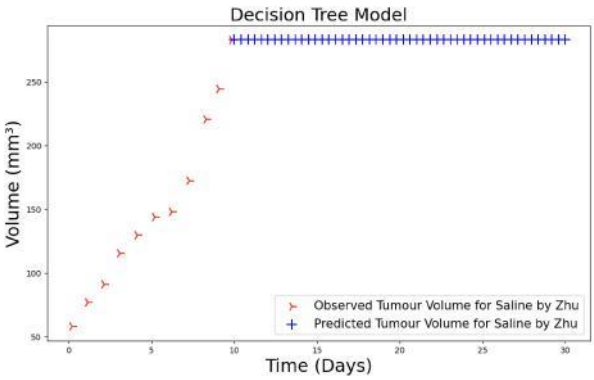

(a) Decision Tree predictions

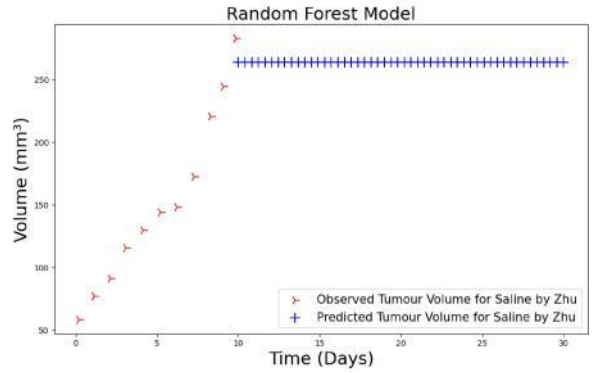

(b) Random Forest predictions

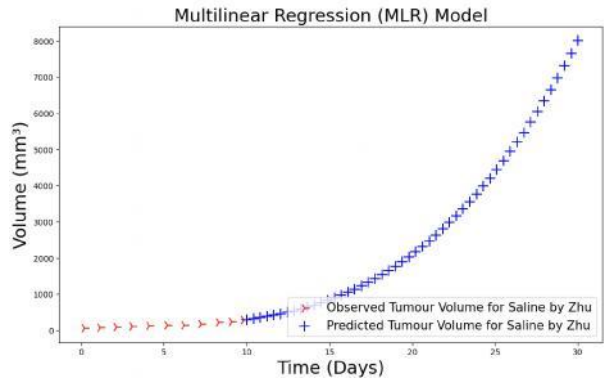

(c) Multilinear Regression model predictions

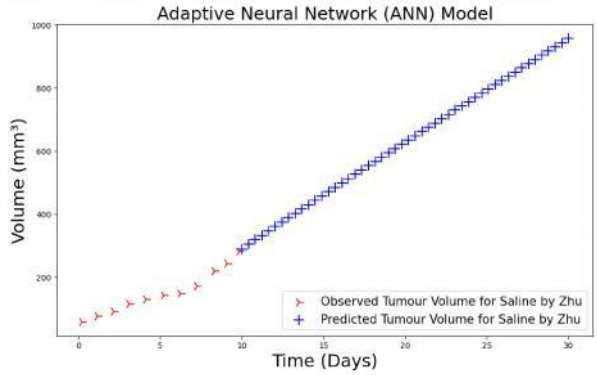

(d) Adaptive Neural Network Model predictions

FIG. 4: Comparison of model predictions for tumor volume growth, based on Saline treatment from Zhu et al [10]

As expected from cross-validation results, the ANN was particularly effective in capturing both the logistic and the exponential phase of the tumor progression, outperforming both MLR and RF models. As shown in figures 3 and 4, the tumor volumes predicted by ANN are closely aligned with expected patterns from the logistic and the exponential phase of the tumor in figure 5. Specifically, for saline treatments by Zhu et al.[10], the ANN reconfirmed that it is the most effective in figure 4d were more accurate in reflecting the actual tumor volumes as observed over a 30-day period compared to other models, as seen in 1b[10].

The logistic and exponential growth phases are illustrated in Figure 5, which further details the tumor progression trends and confirm the expected predictions. For the Fe3O4-mNP treatment, the available dataset covered only a 5-day period, which was insufficient for generating reliable predictions over a 30-day span. To overcome this limitation, mathematical modeling techniques were employed to extrapolate the predictions for the entire 30-day period. These extended projections, as shown in Figure 5e, indicated a substantial reduction in tumor volume by day 25, confirming the efficacy of Fe3O4-mNPs as the best comparative treatment regimen.

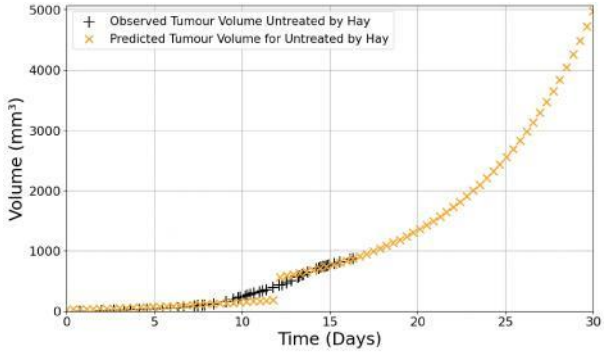

(a) Predicted Tumour Growth (Untreated) based on Hay et al. (2012) [?]

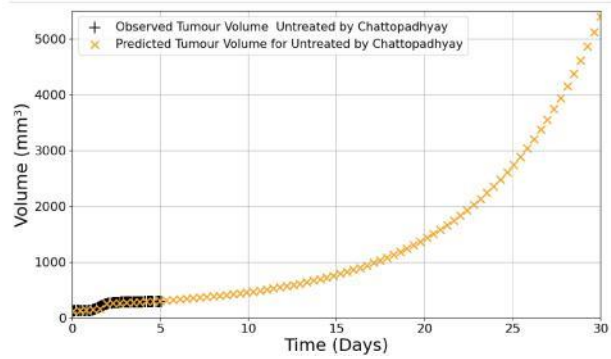

(b) Predicted Tumour Growth (Untreated), based om Chattopadhyay et al. [1]

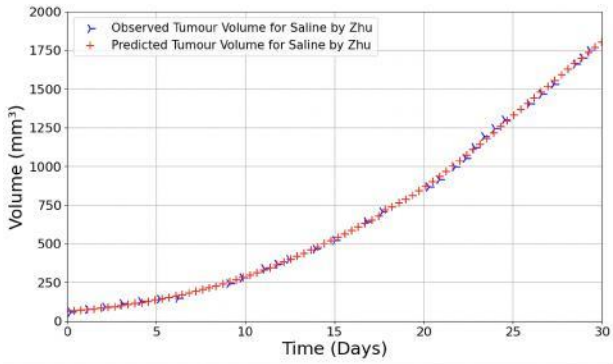

(c) Predicted Tumour Growth with Saline Treatment, based on Zhu et al [10]

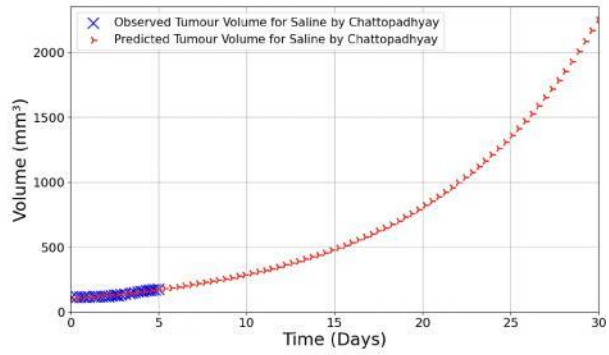

(d) Predicted Tumor Growth with Saline Treatment, based on Chattopadhyay et al. [1]

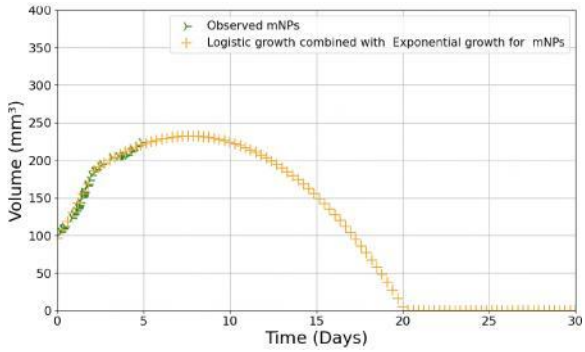

(e) Predicted Tumor Growth under Fe3O4-mNP, from Chattopadhyay, et al. [1]

FIG. 5: Comparison of Predicted Tumour Growth Across Different Studies and Treatment Conditions.

The efficacy of Fe3O4-mNP therapy is highlighted by the differential uptake rates of nanoparticles by cancer and normal cells. While both types of cells take up Fe3O4-mNPs, the cancer cells' higher metabolic demand for glucose leads to a faster and more extensive absorption of Fe3O4-mNPs, allowing for targeted treatment delivery. This ensures that the majority of the therapeutic effect is concentrated in the tumor, thereby minimizing adverse effects on surrounding healthy tissues.

The Fe3O4-mNP treatment showed a targeted therapeutic effect, with cancer cells preferentially absorbing nanoparticles due to higher glucose metabolism, thereby minimizing impact on surrounding healthy tissues. This targeted approach contrasts with conventional surgical excision, which may result in the loss of healthy cells and increased complication risk.

The findings in this research demonstrate the value of AI and mathematical models in predicting and developing personalized treatment strategies. The use Fe3O4-mNPs showed better results, making it a potential alternative to traditional treatments. By accurately predicting tumor growth patterns and treatment responses, this approach supports informed decision-making, allowing for more precise treatment planning. While Fe3O4-mNPs show significant potential for targeted tumor therapy, offering improvements in both treatment effectiveness and safety, further research is required to fully validate their efficacy and optimize their clinical application in the field of precision medicine.

CONCLUSIONS

The study demonstrates that iron oxide magnetic nanoparticles potentially provide a highly effective, targeted treatment option for cancer. AI-driven models, especially Adaptive Neural Networks, show great promise in predicting tumor dynamics with high accuracy, offering potential for personalized treatment planning. These findings have significant implications for developing more effective, non-invasive cancer therapies with fewer side effects.

Additionally, the localized delivery of Fe3O4-mNP injection potentially results in minimal spread of the nanoparticles to nearby normal cells, which further supports the treatment's safety profile. This targeted approach stands in contrast to traditional surgical treatments, where the excision of tumor margins can result in the unnecessary loss of healthy cells, thereby increasing potential complications and affecting overall patient health.

The findings suggest that AI models, particularly deep learning, can play a critical role in optimizing personalized treatment strategies. Iron oxide Fe3O4-mNP based therapy exhibited not only enhanced efficacy but also reduced side effects, offering a promising alternative to traditional chemotherapy. A key outcome of this study is to establish the genericity of the AI modeling approach initially adopted in [1], now remodeled on alternative data sources but still converging to similar outcomes as in the original study [1]. This not only confirms the potency of this formulation but also lends it tenable to address other forms of cancer modeling and relevant predictions.

Future work should focus on expanding the dataset to include a wider range of tumour types and exploring combination therapies that integrate Fe3O4-mNPs with traditional treatments. Further development of AI models could enhance predictive accuracy, leading to more personalized, effective cancer treatments. In summary, this AI-powered study highlights the potential of Fe3O4-mNP-based therapies not only to minimize the collateral damage typically associated with cancer treatments but also to offer a compelling strategy against drug resistance, a growing concern in cancer therapy today.

REFERENCES

[1] Chattopadhyay, A.K., Pascaline, A., Pearce, G. and Russell, S. (2024). Predicting the Progression of Cancerous Tumours in Mice: A Machine and Deep Learning Intuition. *arXiv.org*. Available at: https://arxiv.org/abs/2407.19277 [Accessed 15 Sep. 2024].

[2] Imogen Powell Brown (2024). Leading on Cancer: Why the next UK Government must set out a new strategy for cancer - Cancer Research UK - Cancer News. [online] Cancer Research UK - Cancer News. Available at: https://news.cancerresearchuk.org/2024/06/19/ leading-on-new-strategy-for- cancer/.

[3] Altun, I˙., & Sonkaya, A. (2018). The most common side effects experienced by patients receiving the first cycle of chemotherapy. *Iranian Journal of Public Health*, 47(8), pp.1218–1219.

[4] Anand, U., Dey, A., Chandel, A.K.S., Sanyal, R., Mishra, A., Pandey, D.K., De Falco, V., Upadhyay, A., Kandimalla, R., Chaudhary, A., Dhanjal, J.K., Dewanjee, S., Vallamkondu, J., & Pe´rez de la Lastra, J.M. (2022). Cancer chemotherapy and beyond: Current status, drug candidates, associated risks and progress in targeted therapeutics. *Genes & Diseases*, 10(4). doi: https://doi.org/10.1016/j.gendis.2022.02.007.

[5] Singh, D., Vignat, J., Lorenzoni, V., Eslahi, M., Ginsburg, O., Lauby-Secretan, B., Arbyn, M., Basu, P., Bray, F., & Vaccarella, S. (2022). Global estimates of incidence and mortality of cervical cancer in 2020: A baseline analysis of the WHO global cervical cancer elimination initiative. *The Lancet Global Health*, 11(2). Available at: https://www.thelancet.com/journals/langlo/ article/PIIS2214-109X(22)00501-0/fulltext.

[6] Zhang, B., Shi, H., & Wang, H. (2023). Machine learning and AI in cancer prognosis, prediction, and treatment selection: A critical approach. *Machine Learning and AI in Cancer Prognosis, Prediction, and Treatment Selection: A Critical Approach*, 16(16), pp.1779–1791. doi: https: //doi.org/10.2147/jmdh.s410301.

[7] Iragorri, N., de Oliveira, C., Fitzgerald, N., & Essue, B. (2021). The out-of-pocket cost burden of cancer care—A systematic literature review. *Current Oncology*, 28(2), 1216–1248. https: //doi.org/10.3390/curroncol28020117.

[8] Aras, O., Pearce, G., Watkins, A.J., Nurili, F., Medine, E.I., Kozgus Guldu, O., Tekin, V., Wong, J., Ma, X., Ting, R., Unak, P., & Akin, O. (2018). An in-vivo pilot study into the effects of FDG- mNP in cancer in mice. *PLOS ONE*, 13(8), e0202482. https://doi.org/10.1371/journal. pone.0202482.

[9] Hay, C.M., Sult, E., Huang, Q., Mulgrew, K., Fuhrmann, S.R., McGlinchey, K.A., Hammond, S.A., Rothstein, R., Rios-Doria, J., Poon, E., Holoweckyj, N., Durham, N.M., Leow, C.C., Diedrich, G., Damschroder, M., Herbst, R., Hollingsworth, R.E., & Sachsenmeier, K.F. (2016). Targeting CD73 in the tumor microenvironment with MEDI9447. OncoImmunology, 5(8), p.e1208875. doi: https://doi.org/10.1080/2162402x.2016.1208875.

[10] Zhu, S., Wang, Q., Jiang, J., Luo, Y., & Sun, Z. (2016). A conjugate of methotrexate and an analog of luteinizing hormone releasing hormone shows increased efficacy against prostate cancer. *Scientific Reports*, 6(1). doi: https://doi.org/10.1038/srep33894.

Assessing the Tribological Performance of Sanitary Pads

Akingbeja Fadele O, Sarah R Crossland

University of Hull, School of Engineering, Hull, HU6 7RX

ABSTRACT

The impact of tribological performance on comfort and user satisfaction in material-skin interactions is an established field of study. Work in this field has translated to the investigation of incontinence products, but the performance of sanitary pad products has been largely overlooked despite the substantial user group. With the push for sustainability in personal care products, reusable products are a growing market that should be a key focus for product development.

This study investigated the frictional characteristics of three reusable and five disposable sanitary pads in contact with silicone skin surrogate and PLA reference pin, to work towards understanding the impact of material composition selection on comfort. Repeat tests were conducted on dry and increasingly saturated samples to measure the coefficient of friction on both disposable and reusable pads. With one reusable product being assessed following three sequential wash and dry cycles to assess frictional response to cleaning.

Reusable pads showed a lower coefficient of friction comparative to disposable pads regardless of top cover composition with silicone surrogate interactions. Across both product types, favourably friction coefficients were seen in bamboo composition top covers. Thickness and material composition both contribute to the variance seen in interactions and require further investigation into how to optimise material properties for sanitary products from a comfort perspective. Washing cycles applied to one reusable product, showed a marginal reduction in friction, indicating smoothing or coating of the fibres may be taking place and could impact comfort perception, which should be assessed further to understand the impact on product lifetime comparative to absorbency potential.

Keywords: friction, absorbency, tribology, sanitary, menstruation

INTRODUCTION

Approximately 11,000 disposable sanitary products are used per menstruating user within their lifetime (AHPMA, 2019), of which sanitary pads make up a large market share. During the menstrual cycle, these products are essential for maintaining comfort, hygiene, and protection (Woo et al., 2019). Whilst comfort is identified as a key contributing factor to user satisfaction with products (Ahn and Kim, 2016; Atasağun and Kara, 2022), quantification approaches to comfort are limited due to the subjective nature of the subject and complexity of factors which influence this.

The use of tribology as a performance indicator for skin-material interactions, in lieu of comfort scoring, has gained traction in recent years (Baby et al., 2021; Li et al., 2012). Tribology is a growing area of exploration in relation to incontinence product interactions (Morecroft et al., 2023), but has yet to see the development in the field sanitary products despite their similar environmental conditions with few studies conducted (Atasağun and Kara, 2022; Farage et al., 2009; Tang et al., 2020).

Sanitary pads, both disposable and reusable, usually consist of several layers, each with a distinct function. These layers consist of the absorbent core, the rear sheet for leak protection and the top sheet that comes into touch with the skin. Whilst the central function of the product being to maximise absorbency, the choice of top cover material will both contribute to this function and user comfort. The top cover must be able to wick away moisture from the skin to the absorbent core, allow for transition of menstrual blood to the core and reduce irritation on contact with the skin (Woo et al., 2019).

The popularity of reusable sanitary products has grown in recent years in western users, where it was already popular in other markets, due to the push for environmental responsibility and coinciding reduction of single use products in personal care. The balance between comfort and functionality between disposable and reusable products can differ due to their intended use.

Recent studies of incontinence pads have focused on tribology in relation to dry and fully saturated conditions (Morecroft et al., 2023), though this neglects the comfort of the user as saturation increases during use where maximum absorbency and peak frictional behaviour may not align.

The majority of recent research in the sanitary product industry has concentrated on materials science, absorbency, and leak protection, but the impact of comfort to frictional response is a growing area of interest to work towards improving user satisfaction and reduction in skin irritation seen in higher friction interfaces (Atasağun and Kara, 2022; Baby et al., 2021; Farage et al., 2009; Tang et al., 2020; Woo et al., 2019)

With limited research currently undertaken of the tribological response of sanitary pads and the growing market for reusable products, further study is required of the contribution of top cover materials on the frictional response of increasingly saturated products. As such, this study aims to investigate frictional performance for a range of market available disposable and reusable sanitary pad to work towards understanding product comfort. This will form the basis for identification of key performance indicators for a tribologically 'comfortable' sanitary product to feed into further research. To achieve this, testing of a range of disposable and reusable sanitary products was undertaken in dry and increasing saturation environments. To ascertain the impact of material composition on tribological performance a range of differing materials were also selected for study. To further this, initial testing of the impact of repeat washing and drying cycles on frictional response in reusable sanitary pads was also undertaken.

MATERIALS & METHODS

A selection of disposable and reusable sanitary products were chosen to represent a spread of top cover material options available on the consumer market (Table 1). Not all brands made the percentage composition of their top cover materials public and investigation of textile characteristics is beyond the initial scope of this study. The material composition instead was chosen as an indicator of potential differing influencing factors on user comfort.

Table 1: Tribologically studied disposable and reusable sanitary products, including brand name, product type, and top layer composition.

Brand Name	***Product Type***	***Top Layer Composition***
FLO Organic Bamboo	Disposable	Oeko-Tex bamboo
Rael	Disposable	Cotton
Natra-Care Ultra	Disposable	Organic cotton
Lil-Lets Normal	Disposable	Polyester-polyethylene blend
Super Eco by Naty	Disposable	Organic cotton and wood pulp
MQUPIN	Reusable	Organic cotton
Eco Lily	Reusable	Bamboo with charcoal
Femplete	Reusable	Bamboo

A High Frequency Reciprocating Rig (HFRR) tribometer from PCS Instruments Ltd was utilised to support the tribological investigation. This traditionally operates as a ball-on-plate tribometer, with single axis motion across the sample site, however adaptions were made to both the interacting pin and sample holder plate to allow for a bespoke testing approach. This was done to reflect the increased contact area seen in sanitary pad/body interactions to work towards replication of the operating environment within the scope of bench top assessment.

The pin was replaced with a 31.5 mm diameter hemispherical pin with a contoured contacting interface was created in lieu of the body surface. The complexity and variance in body shaping and skin presentation across the population means that reduction of the anatomy to simple geometries was required. Two pins were designed [Solidworks, v2023] with polylactic acid (PLA) base structures and 3D printed [Ultimaker 2 Extended +, Ultimaker]. The first pin was PLA solely (Fig.1), with the second being a 2 mm circumferential reduction of the PLA and coated instead in silicone to return the pin to the same measurements as the first pin. Silicone coating was used as a surrogate for the anatomical skin interface. With skin thickness, and mechanical characteristics offering high variance across the body and cadaveric testing beyond the scope of the study, approximate skin thicknesses of 2 mm was chosen to be representative. Ecoflex 00-30 [smooth-On] silicone was selected as skin surrogate for its similar young's modulus behaviour to skin (Vaicekauskaite et al., 2019).

A sample holder of 55 x 45 mm was designed using Solidworks [v2023] to allow for sufficient movement of the pin on the sample without interactions with the side profiles of the holder to reduce edge effects. The sample holder consisted of a base tray with push fit clamp (Fig.1) to provide stability to the multilayer pads and appropriate surface tension to the sample in situ.

Materials samples were prepared in line with sizing of the bespoke sample holder. A template was used to cut the samples to the correct sizing, which included the full depth of the product including all constituent layers. To prevent displacement of the layers beyond which the clamping mechanism could control, side profiles of reusable samples were hand sewn closed to maintain the absorbent core positioning.

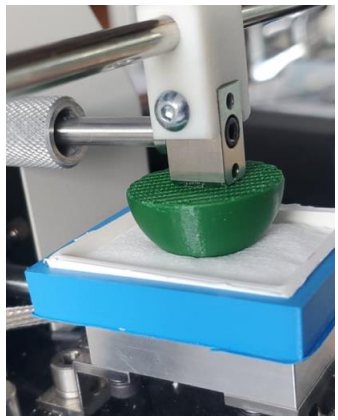

Figure 1: HFRR tribometer [PCS Instruments Ltd] with bespoke sample holder attachments showing a 3D printed PLA pin and sanitary pad clamping sample holder.

During activities of daily living, the body-sanitary pad interface undergoes a variety of interactions of differing contacting pressures and shearing profiles. To represent the extremity of the loading interaction, the seated position was chosen as the basis for investigation. Pressure mapping is a widely used tool in biomechanics and has been used to map the pressures exerted during seating in wheelchair users (Yu et al., 2014). These measures can be used in to inform expected pressures in seating and were taken to determine the loading profile of the tribometer. Loading was applied to replicate 200 mmHg pressure considering the contacting area between pin and sample (Yu et al., 2014). A 1.5 mm reciprocating stroke length was used to represent motion under loading. The testing was run at the lowest operating frequency and time of the instrumentation (10 Hz for 60 seconds), with the duration allowing each test to achieve a stabilised coefficient of friction.

Initial tests of each material were conducted on a dry sample, with saturation then increased in 2 ml increments up to a saturation level of 10 ml. Saline solution was used in place of menstrual blood (DeLoughery et al., 2024), reducing ethical implications, procurement, sample handling challenges and the impact of blood viscosity and clotting on standardisation of testing protocol. For the sample size comparative to the full product size and approximate expected maximum saturations, it is assumed that the 10 ml total dosing will bring the product to near full saturation and was kept at this end point to maintain consistency across samples.

Disposable products were discarded after use and repeats on five clean samples through to full saturation was taken. Due to procurement availability of new unwashed reusable products in the study, only three repeats were undertaken on these products. This was because it was assumed that the washing process would introduce changes in the frictional properties of the materials being studied, hence only unwashed products were considered. All trials were repeated with both the PLA and silicone coated PLA pins for comparison.

To scope the impact washing may produce on frictional outputs, one of the reusable products, Femplate, was chosen to be taken forward for wash cycle trials. Following the initial saturation testing on this pad, it was hand washed using 2.5 ml of biological detergent (easy Bio, easy) dissolved in 400 ml of cold tap water for two minutes prior to air drying. The increasing saturation study was then repeated, followed by another subsequent wash cycle. In total this amounted to three rounds of frictional assessment on previously washed samples.

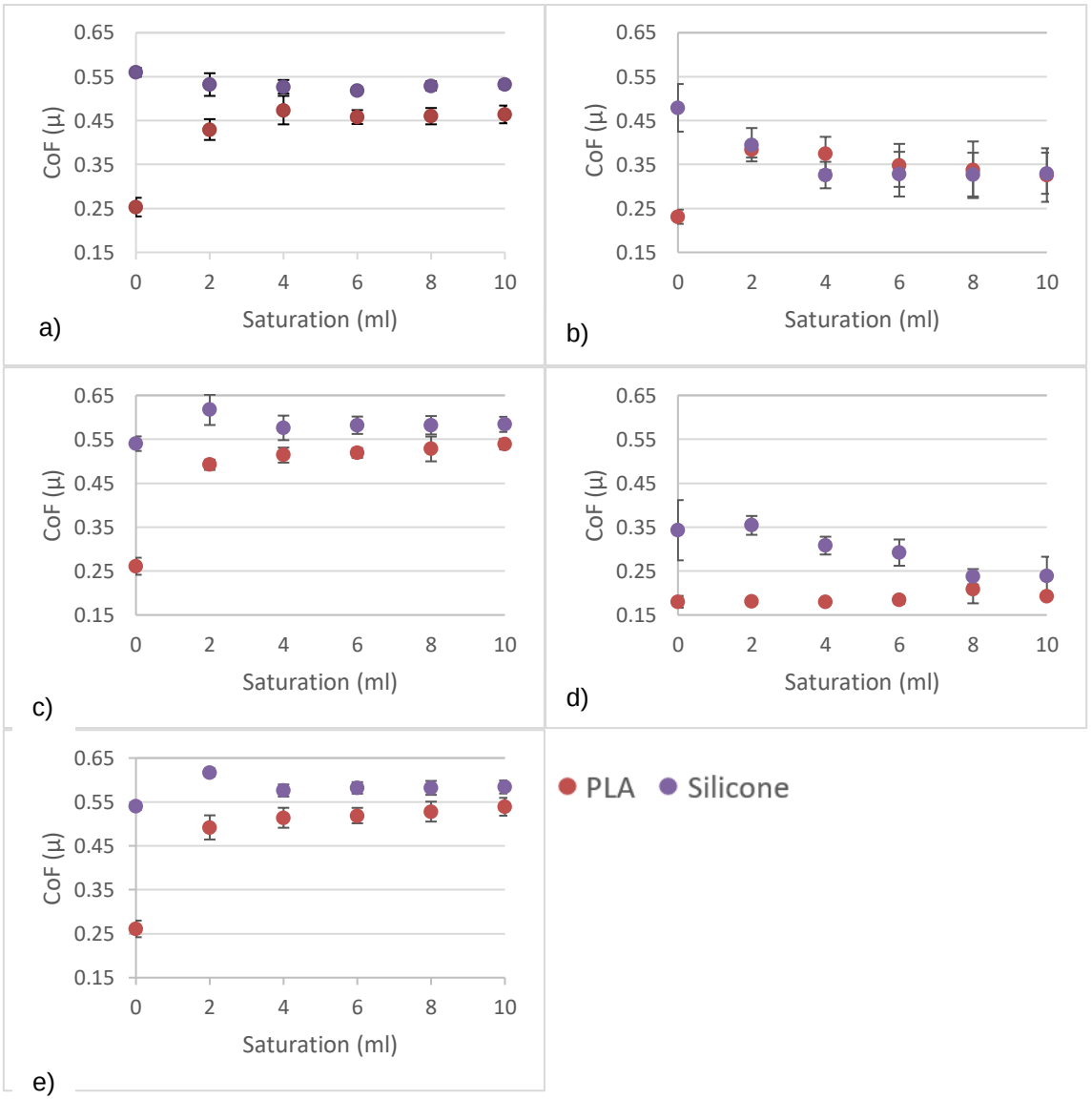

Figure 2: Graphs of friction against increasing salination saturation for PLA and Silicone pins including standard deviation for the disposable sanitary pads a) Super Eco by Naty, b) Flo Organic Bamboo, c) Rael, d) Natra-Care Ultra and e) Lil-Lets Normal.

RESULTS AND DISCUSSION

For the disposable sanitary pads, Fig. 2, across all samples interactions with the silicone pin gave a substantially higher friction response than the PLA pin in dry conditions. Increasing the saturation of the products in general lead to a reduction in friction for the silicone and increasing friction with the PLA through to plateau. However, the silicone pins remain at a higher overall friction, though this is expected of the surrogate in line with increasing friction in moist or wet conditions for skin (Derler and Gerhardt, 2012). The bamboo (Fig. 2 b) and polyester blend (Fig. 2 e) top cover compositions showed lower coefficients of friction. Cotton blend top covers (Fig. 2 a,c,d) showed comparatively higher frictional response with the silicone surrogate pin. This indicates that the material composition and fibres present play a significant role in comfort which should be investigated further.

Improved frictional response was seen in the reusable pads relative to the disposable (Fig. 3) directly contrasting (Tang et al., 2020), with all three material top layers of organic cotton, bamboo and bamboo with charcoal performing mostly within the expected comfort range for skin-material contacts. The contradiction in values could potentially be due to the differing response of silicone and skin under wet conditions. Whilst these materials are similar fundamentally to those in the disposable products, it is hypothesised that the thickess of the top layers relatively may lead to the improved change in frictional response. As with the disposable products, bamboo composition top cover (Fig. 3 a,b) showed consistently lower frictional response than the cotton comparative (Fig. 3 c), which showed a gradual increase in friction wth increased saturation not seen in other products.

The results of the Femplete repeated wash and dry cycle testing, Fig. 4, showed an anecdotal marginal decrease in friction with increasing washing cycles. This pattern indicates that the washing cycles alters the pad's surface properties, potentially as a result of the fibres becoming softened or slightly degraded, which could lower friction levels overall. It can also be noted that the interactions of the silicone and PLA pins and sample when dry compared to saturation did not deviate signinficantly as with the disposable products.

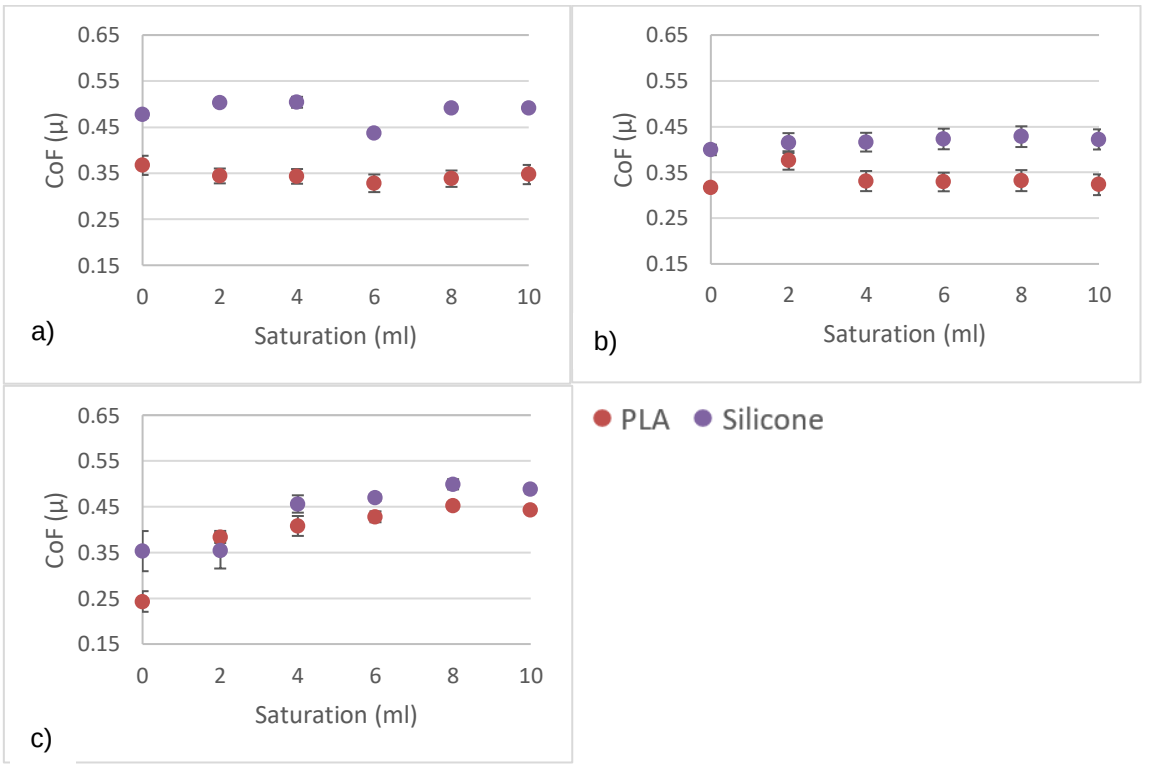

Figure 3: Graphs of friction against increasing salination saturation for PLA and Silicone pins including standard deviation for the reusable sanitary pads a) Eco Lily, b) Femplete, c) MQUIPIN.

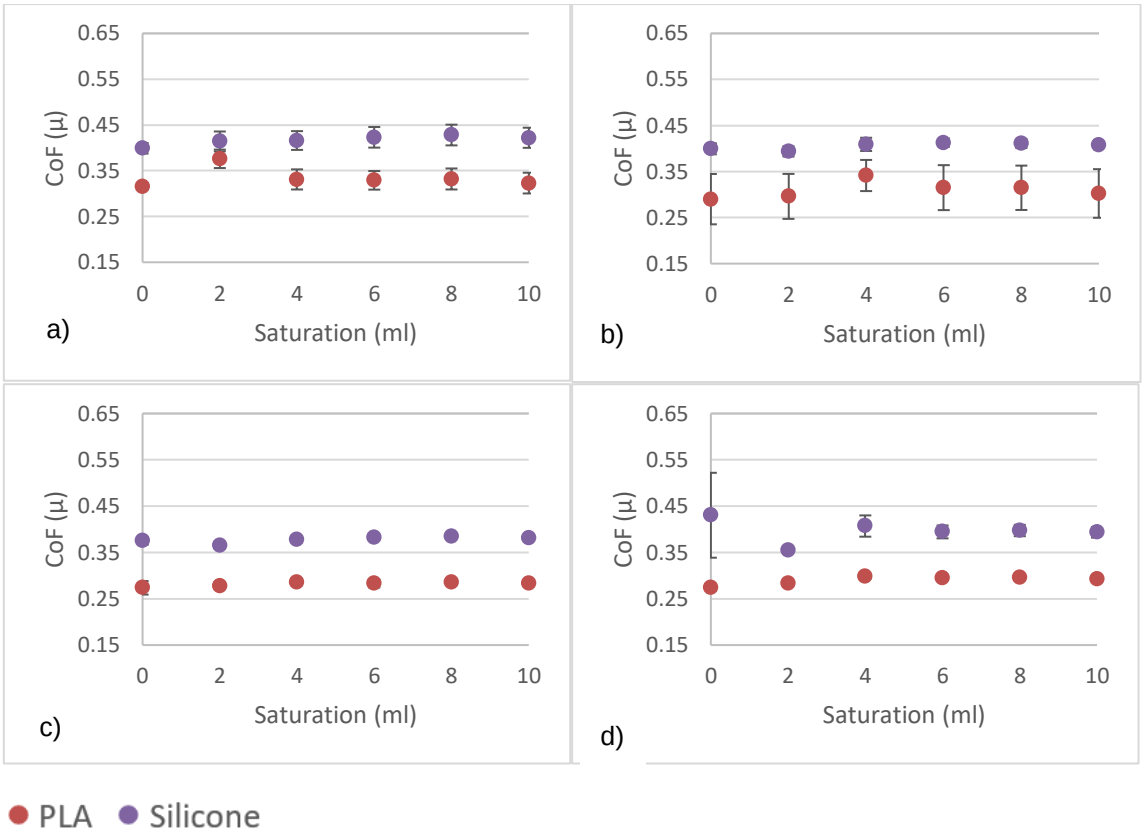

Figure 4: Graphs of friction against increasing salination saturation for PLA and Silicone pins including standard deviation for the reusable sanitary pad Femplete, a) unwashed, b) following one wash and dry cycle, c) following two wash and dry cycles and d) following three wash and dry cycles.

As a result of these initial studies further work must be undertaken to address the limitations present. Firstly whilst silicone is commonly used as an appropriate skin surrogate due to aligned mechanical characteristics, repeated studies should be conducted with animal or cadaveric tissue to assess any potential deviations in frictional response due to the porosity of tissue comparative to silicone when assessing saturation behaviour.

Material composition, thickness and the influence of the absorbant core all play a key role in the surface tribology. Analysis of the saturation response of the core, the wicking ability of the top layer, fibre composition imaging and thickness measurements should be considered to underpin the frictional responses seen and determine optimal top cover characteristics in both disposable and reusable pads.

Expanded studies to investigate the response of washing to a range of resuable products should be considered, including extending the number of cycles the pad undergoes to assess the expected lifetime of the products from a comfort perspective in relation to their expected lifetime for absorbancy.

It is key to note that assumed comfort seen in traditional material-skin friction studies does not necessarily reflect the skin sensitivity of the anatomical focus of this study. With comfort also being a subjective term, building an understanding of the key contributors to comfort in this field is necessary. This should take into account the friction, humidity of environment, skin condition, pubic hair and the impact of menstrual clotting to fully reflect the complex biological environment in which sanitary products are used.

CONCLUSIONS

Frictional response and comfort between skin and materials have long been linked (Baby et al., 2021). In this study, reusable sanitary products appear to offer a perceived increase in comfort to the wearer due to lower frictions comparative to disposable products. For both disposable and reusable products bamboo

composition top layers showed lower relative coefficients of friction than most other trialled materials. The material composition and thickness are key components in the variances seen in these interactions and should be investigated further to assess fibre characteristic impact. It was also seen that washing of the products appears to marginally reduce the friction and warrants further investigation into product lifetime and top cover optimisation through friction behaviour.

REFERENCES

[1] Ahn, S., Kim, Y.M., 2016. A Study of the Perception about Menstruation and Discomforts of Using Disposable Menstrual Pads. Korean Journal of Women Health Nursing 14, 173–180.

[2] AHPMA, 2019. Menstruation Facts and Figures [WWW Document]. URL https://www.ahpma.co.uk/menstruation_facts_and_figures/ (accessed 11.14.24).

[3] Atasağun, H.G., Kara, S., 2022. Investigation of Moisture Management and Frictional Characteristics of Top Layers Used in Disposable Absorbent Hygiene Products. Fibers Polym 23, 2577–2585. https://doi.org/10.1007/s12221-022-0032-7

[4] Baby, R., Mathur, K., DenHartog, E., 2021. Skin-textiles friction: importance and prospects in skin comfort and in healthcare in prevention of skin injuries. The Journal of The Textile Institute 112, 1514–1530. https://doi.org/10.1080/00405000.2020.1827582

[5] DeLoughery, E., Colwill, A.C., Edelman, A., Bannow, B.S., 2024. Red blood cell capacity of modern menstrual products: considerations for assessing heavy menstrual bleeding. BMJ Sex Reprod Health 50, 21–26. https://doi.org/10.1136/bmjsrh-2023-201895

[6] Derler, S., Gerhardt, L.-C., 2012. Tribology of Skin: Review and Analysis of Experimental Results for the Friction Coefficient of Human Skin. Tirbol Lett 45, 1–27.

[7] Farage, M.A., Berardesca, E., Maibach, H., 2009. Skin moisturization and frictional effects of an emollient-treated menstrual pad with a foam core. Cutaneous and Ocular Toxicology. https://doi.org/10.1080/15569520902738408

[8] Li, W., Pang, Q., Jiang, Y., Zhai, Z., Zhou, Z., 2012. Study of Physiological Parameters and Comfort Sensations During Friction Contacts of the Human Skin. Tribol Lett 48, 293–304. https://doi.org/10.1007/s11249-012-0023-8

[9] Morecroft, R., Tomlinson, K., Lewis, R., Carré, M., 2023. Friction between human skin and incontinence pads in the presence of barrier protection products. Proceedings of the Institution of Mechanical Engineers. Part H, Journal of Engineering in Medicine 238, 644. https://doi.org/10.1177/09544119231178477

[10] Tang, K.-P.M., Li, C.-H., Kan, C.-W., 2020. Instrumentation for Measuring the Wet Frictional Property of Sanitary Pads. Fibers Polym 21, 216–223. https://doi.org/10.1007/s12221-020-9623-3

[11] Vaicekauskaite, J., Mazurek, P., Vudayagiri, S., Skov, A.L., 2019. Silicone elastomer map: design the ideal elastomer: SPIE Smart Structures + Nondestructive Evaluation 2019. Proceedings of SPIE, Proceedings of SPIE - The International Society for Optical Engineering 10966. https://doi.org/10.1117/12.2515305

[12] Woo, J., Kim, S., Kim, H., Jeong, K.S., Kim, E., Ha, E., 2019. Systematic Review on Sanitary Pads and Female Health. Ewha Med J 42, 25–38. https://doi.org/10.12771/emj.2019.42.3.25

[13] Yu, C.-H., Chou, T.-Y., Chen, C.-H., Chen, P., Wang, F.-C., 2014. Development of a Modularized Seating System to Actively Manage Interface Pressure. Sensors 14, 14235–14252. https://doi.org/10.3390/s140814235

Development of conductive materials mechanically representative of human skin for sensors to test mechanical performance of Negative Pressure Wound Therapy devices.

Catherine A. Hill[1], Jarinat M. Kasim[1], Ali. Dostan[1], C. Casey[2], Louise A. France[1]

1 University of Hull, Department of Engineering, Hull, HU6 7RX;

2 Smith+Nephew PLC, Hull, HU3 2BB

ABSTRACT

This research focuses on the development of sensing elements, mechanically representative of human skin, to create sensors for measuring the mechanical performance of negative pressure wound therapy (NPWT) devices. The research outlines the development of conductive sensing elements designed to measure strain and pressure, using materials that are mechanically similar to human skin to more accurately assess tissue-device interaction. Silicone was identified as the most mechanically similar material to human skin, and the silicones used, Polycraft Zhermack ZA13 and Polycraft Silskin10, were mechanically tested to validate this against literature. The two different sensing elements are solid conductive silicone for sensing strain and a porous silicone foam coated in conductive polymer coating for sensing pressure. Mechanical forces and displacement were applied to the materials, and the electrical responses were monitored. The results indicate that Silskin10 is better suited for tension applications, providing more reliable strain sensing, while Zhermack demonstrates greater performance in compression, offering enhanced tissue-like flexibility for pressure sensing. These findings highlight the importance of material choice for achieving consistent and accurate sensor performance in NPWT device testing. The study contributes valuable insights into the design of sensors that accurately represent the wound environment and measure the mechanical performance of NPWT devices, emphasizing the need for further research to refine these materials.

Keywords: Wound healing, NPWT, conductive silicones, resistance, tensile testing, compression testing

INTRODUCTION

Chronic wounds, including pressure ulcers, diabetic foot ulcers, and venous leg ulcers, pose significant challenges in modern healthcare, affecting millions of patients globally. These wounds are characterized by prolonged healing times and high incidences of complications, severely impacting patients' quality of life and leading to increased healthcare costs (Julian et al., 2020; Posnett & Franks, 2008; Sen et al., 2009). Traditional treatments frequently fail to achieve effective and sustained healing, necessitating innovative approaches. Negative pressure wound therapy (NPWT) has emerged as a promising intervention, with biological studies demonstrating its potential to enhance wound healing by utilising controlled negative pressure to promote a moist wound environment, reduce oedema, and stimulate tissue granulation (Anghel & Kim, 2016; Brownhill et al.; Dowsett et al.; Gregor et al., 2008; Huang et al., 2014). While existing FDA-approved test platforms focus on evaluating the functionality and safety of NPWT devices, they do not assess mechanical performance (FDA, 2018). This gap in testing methodology leaves a critical need for understanding how the mechanical attributes of NPWT devices contribute to wound healing. Current methods fail to provide insights into the relationship between mechanical performance and healing efficacy, thereby limiting the optimisation of these devices for different wound types and patient conditions (Mulligan, 2011).

This study aims to address these knowledge gaps by developing sensing elements to create a sensor to assess the mechanical performance of NPWT devices, specifically measuring strain and pressure in a manner that reflects the interaction between tissue and device. Whilst sensors in literature do aim to recreate attributes of human skin such as flexibility, they focus on using these properties to enhance sensing systems performance instead of truly representing human skin mechanically (Fortunato et al., 2020; Gao et al., 2017; Gu et al., 2019; Huang et al., 2023). The silicones used in this study were chosen as they aligned with existing literature regarding their mechanical similarity to human skin (Dabrowska et al., 2016). They were also mechanically tested to identify their Young's Modulus to validate this further, with

human skin Young's Modulus typically quoted in a range of 0.005-140 MPa (Kalra & Lowe, 2016). The two sensing elements are: one made from conductive silicone for sensing strain, and another formed from silicone foam coated with a conductive polymer coating for sensing pressure. The sensing elements are based on the principle of exploiting structural and resistive control through high- and low-resistance mixture (Matsuda et al., 2020). This was identified as the ideal method for making sensors entirely from silicones. Experimentation was undertaken to reformulate conductive silicone procedures outlined in the literature to work for these studies chosen silicones (Brensing et al., 2013; Sherif & Almufadi, 2019). How electrical measurements of these elements can be used to measure strain and pressure is demonstrated in Figure 1. It is based on the principle that as the length of the conductive material increased the resistance of the material also increases proportionally.

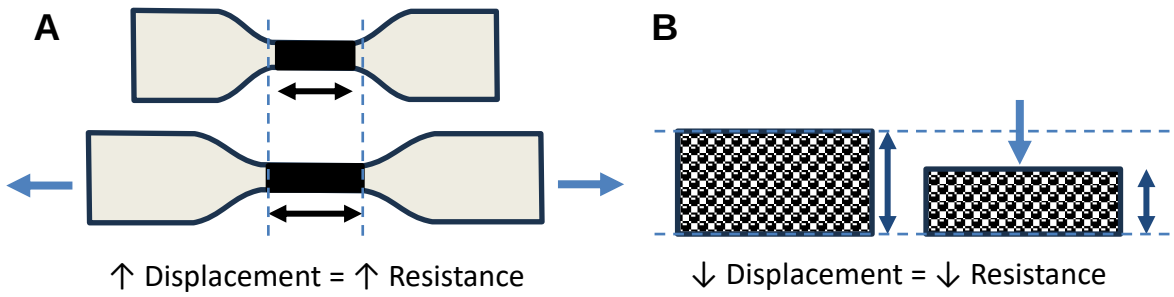

Figure 1: A) Displacement of dogbone in tension increases the length of the conductive material central to dogbone increasing its resistance. B) Displacement of foam in compression decreases the height of the conductive foam decreasing its resistance.

MATERIALS & METHODS

The study aimed to examine the mechanical properties of the silicones and electrical responses of the sensing elements. The two chosen silicones for this study were Polycraft Zhermack ZA13 and Polycraft Silskin10 (MB Fibreglass, UK), selected for their mechanical similarity to human skin defined by Young's Modulus. The silicones were mechanically test through two methods, tension testing using dogbone specimens of type 5A tested to destruction with a pre-load and load of 0.5 mm/sec on a 1kN load cell, in accordance with ISO527-2; and compression testing with a displacement of 2mm/min on the LS1 Universal Tester (Lloyds Instruments, UK).

The sensing elements were manufactured as follows. A low resistance conductive silicone was created through the combination of silicone, carbon black and chloroform, this was then painted along a dogbone of non-conductive silicone. Porous silicone foams were created by a simple porogen leaching process (caster sugar) and then coated with a high resistance polymer consisting of polyvinylidene difluoride (PVDF), dimethylformamide (DMF) and carbon black. To make the high resistance conductive coating, combine PVDF granules with DMF until the PVDF has dissolved. Then combine carbon black and mix thoroughly. Porous silicone foam is then dipped in the solution to coat it and dried in a vacuum oven. To make low resistance silicone paste, add carbon black to chloroform and mix thoroughly. Then mix a 1:1 ratio of silicone and add to the carbon-chloroform mixture using a syringe and mix thoroughly again. This can then be painted on top of non-conductive silicone in the desired shape and or pattern. Mechanical testing of the materials was repeated after the application of conductive materials to assess the impact.

To test the sensing elements, mechanical forces, specifically set loads and displacements were applied to them. The LS1 Universal Tester (Lloyds Instruments, UK) applied tension to the low resistance conductive silicone and applied compression to the high resistance conductive silicone foams. Whilst under these forces resistance was measured using a multimeter (Tenma 72-7780) to assess changes in resistance as a result of applied mechanical stress.

RESULTS AND DISCUSSION

Mechanical Tension Testing

The non-conductive Silskin10 sample exhibited a Young's Modulus of 0.20 MPa, positioning it as a relatively stiff material compared to the flexibility of general human skin. While this stiffness may not closely mimic the feel of natural skin, non-conductive Silskin10 provides a stable structure suitable for static and dynamic model applications in negative pressure wound care testing. Its combination of durability and moderate flexibility allows it to withstand repeated deformation cycles, making it useful for sensor implementations that require consistent response over time without excessive deformation.

The non-conductive Zhermack sample, with a Young's Modulus of 0.11 MPa, offers a softer, more flexible option than Silskin10. This lower modulus aligns it more closely with the softness needed for testing models that simulate human tissue mechanics under negative pressure. Its increased pliability makes non-conductive Zhermack an excellent candidate for dynamic testing environments where material deformation can occur in multiple cycles. This flexibility can enhance the accuracy of simulated responses in wound care models, particularly where more tissue-like compliance is needed.

The conductive Silskin10 sample has a Young's Modulus of 0.22 MPa, making it slightly stiffer than its non-conductive counterpart. This modulus suggests it can endure stress without deforming excessively, which is valuable in static or dynamic testing where sensor reliability is critical. Conductive Silskin10's combination of rigidity and conductivity makes it well-suited for applications where precise electrical feedback is required to simulate wound care scenarios, enabling the monitoring of pressure levels while resisting material fatigue over extended test durations.

In contrast, the conductive Zhermack sample, with a very low Young's Modulus of 0.01 MPa, is exceptionally pliable, closely mimicking the softness of human tissue. This extreme flexibility is advantageous for applications involving complex deformations under dynamic pressure conditions, as it can conform closely to model surfaces and endure significant bending and stretching. Its softness and flexibility are ideal for creating highly sensitive models that replicate the behaviour of wound tissues under varying pressures, providing insights into how negative pressure devices impact wound surfaces.

A summary of the mechanical properties in tension can be found in table 1. For testing negative pressure wound care devices, non-conductive Zhermack offers a soft, flexible option that mimics tissue compliance, particularly useful in dynamic testing environments. Conductive Zhermack, with its low stiffness, is ideal for applications requiring close conformity and high sensitivity in pressure simulations. Non-conductive and conductive Silskin10, while stiffer, provide durability and structural stability, making them suitable for scenarios that demand robust material performance in repeated static and dynamic testing cycles.

Table 1: Mechanical properties of sensor materials in tension

Material	*Mean Young's Modulus (MPa)*	*Standard Deviation*	*References*
Nonconductive Silskin10 Dog bones, n=10	0.20	±0.03	(Blair et al.; Diridollou et al., 2000; Kalra & Lowe, 2016; Luebberding et al.; Ni Annaidh et al., 2012)
Nonconductive Zhermack Dog bones, n=10	0.11	±0.02	
Conductive Silskin10 Dog bones, n=5	0.22	±0.03	
Conductive Zhermack Dog bones, n=5	0.01	±6.18E-07	
General Human Skin	0.005-140		

Mechanical Compression Testing

The non-conductive solid Silskin10 sample has a Young's Modulus of 3.72 MPa, falling within the mid-to-lower range of general human skin's modulus. This stiffness suggests a balance between flexibility and structure, making solid Silskin10 suitable for testing negative pressure wound care devices in both static and dynamic models. Its modulus suggests it can simulate firmer skin regions while providing durability and moderate flexibility, ideal for applications requiring material integrity over multiple deformation cycles.

In comparison, the non-conductive Silskin10 foam exhibits a Young's Modulus of 3.26 MPa. Although close in value to its solid counterpart, this slight reduction in stiffness reflects the foam's enhanced pliability, which can allow for more surface adaptability and conformity under pressure. This makes the non-conductive foam variant slightly more suitable than the solid version in testing environments where a softer, skin-like response is needed, as it better accommodates deformation. The foam's structure provides a balance between resilience and flexibility, making it especially relevant in applications that involve pressure cycling, as its performance more closely approximates the flexible properties of skin.

For Zhermack, the non-conductive solid sample has a Young's Modulus of 1.36 MPa, which is notably lower than both Silskin10 solid and foam variants, positioning it in the lower range of skin stiffness. This relatively soft modulus makes Zhermack more adaptable for dynamic testing scenarios that require a material with greater pliability and softer skin simulation. In contrast, the non-conductive Zhermack foam sample has a Young's Modulus of 3.09 MPa, which is considerably stiffer than its solid counterpart. This increase in stiffness in the foam variant suggests a structure that can better withstand applied pressures, making it suitable for applications where greater mechanical resilience is required while still maintaining flexibility. Thus, the non-conductive foam versions of both Silskin10 and Zhermack tend to exhibit slightly stiffer, more durable properties than their solid counterparts, while offering better conformity to surfaces under pressure.

When comparing non-conductive and conductive foams, the conductive Silskin10 foam has a Young's Modulus of 3.57 MPa, which is stiffer than its non-conductive counterpart. This increased stiffness in the conductive foam suggests that the addition of conductive materials enhances structural stability, providing a firmer response that may slightly reduce pliability. This characteristic is advantageous for applications that require consistent shape retention and mechanical response under variable pressures, as seen in static and dynamic testing for wound care devices.

The conductive Zhermack foam has a Young's Modulus of 3.67 MPa, which is the stiffest among all the foam samples. Compared to the non-conductive Zhermack foam, the conductive version demonstrates a marked increase in stiffness, likely due to the incorporation of conductive fillers that strengthen the foam structure. This increased stiffness can be beneficial in applications where additional rigidity is preferred, making it suitable for testing models that require a high level of durability. However, this enhanced stiffness might slightly reduce the material's compliance compared to the non-conductive Zhermack foam, making it less effective at simulating the more flexible behaviour of skin but more suitable for scenarios needing resilient material responses.

A summary of the mechanical properties in compression can be found in table B. both non-conductive and conductive foam silicones provide enhanced stiffness over their solid counterparts, with non-conductive foams generally being softer and more adaptable than conductive foams. The conductive versions of Silskin10 and Zhermack foams show higher Young's Modulus values, suggesting increased rigidity due to conductive filler materials. This range of stiffness across non-conductive and conductive silicones offers a spectrum of options for wound care device testing, from highly flexible materials that mimic soft skin regions to stiffer, more resilient foams that suit models requiring structural integrity under pressure.

Table 2: Mechanical properties of sensor materials in compression

Material	*Mean Young's Modulus (MPa)*	*Standard Deviation*	*References*
Solid Silskin10 sample, n=5	3.72	±4.73E-07	(Blair et al.; Diridollou et al., 2000; Kalra & Lowe, 2016; Luebberding et al.; Ni Annaidh et al., 2012)
Solid Zhermack sample, n=5	1.36	±2.18E-06	
Non-conductive Silskin10 Foam, n=5	3.26	±3.94E-06	
Non-conductive Zhermack Foam, n=5	3.09	±4.05E-06	
Conductive Silskin10 Foam, n=5	3.57	±4.09E-06	
Conductive Zhermack Foam, n=5	3.67	±4.37E-06	
General Human Skin	0.005-140		

Resistance under tension

The initial resistance of Silskin10 was measured at 204.3 Ω, dropping sharply to 13.45 Ω when subjected to tensile strain, as seen in figure 2. This significant reduction in resistance suggests an improvement in conductivity under stretching, likely due to the orientation and distribution of conductive particles within the silicone matrix. Stretching the material may create conductive pathways, enhancing electrical flow through the substrate. However, Silskin10 displayed a large standard deviation of 507.69 Ω, indicating considerable variability in resistance measurements across tests. This variability points to inconsistencies in the conductive coating or particle distribution, which could compromise its reliability in applications where stable performance is required. Addressing these inconsistencies, potentially by refining the conductive coating application technique or adjusting the formulation to ensure uniform particle dispersion, could improve Silskin10's suitability for consistent strain-responsive sensing.

In contrast, Zhermack exhibited an initial resistance of 127.7 Ω, which increased to 882 Ω following tensile loading, as seen in figure 2. This increase suggests a decrease in conductivity under strain, potentially due to poor integration of the conductive liquid within the silicone matrix. Under tensile strain, the conductive pathways within Zhermack may be disrupted, causing resistance to rise. This response implies that the current coating or embedding method does not effectively maintain conductive integrity under tensile forces, an issue that may require alternative formulations or application techniques to enhance its performance in tensile applications. The contrasting responses of Silskin10 and Zhermack under tension highlight fundamental differences in how these materials interact with the conductive medium under strain, making Silskin10 a potentially better candidate for tension-based applications if its variability can be reduced.

Both materials exhibited increased resistance following repeated testing, suggesting conductivity degradation over time, a common challenge in conductive elastomers subjected to cyclic loading. Silskin10's resistance rose significantly to 1433.7 Ω, while Zhermack's resistance increased to 1304.27 Ω. This increase suggests material fatigue, with structural or compositional breakdown leading to diminished conductivity. This finding indicates that both Silskin10 and Zhermack may experience limitations in long-term applications, as repeated strain appears to compromise their conductive performance. Enhancing the durability of the conductive network within these materials, possibly through reinforcements, more resilient conductive particle coatings, or alternative conductive fillers, may extend their longevity and reliability in applications requiring consistent performance over extended use.

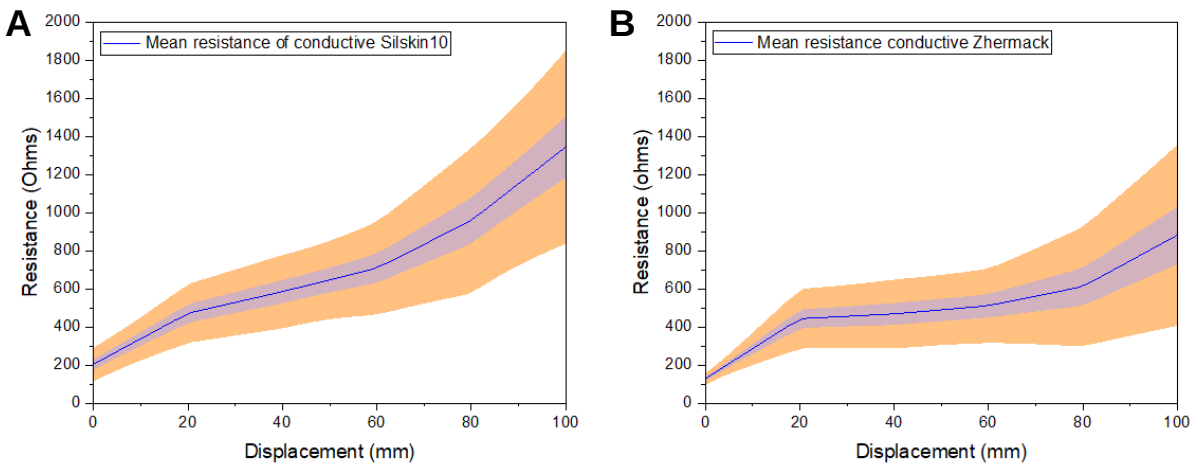

Figure 2: Mean resistance against displacement of conductive solid silicones in tension, where n=5, with standard deviation (blue shaded region) and standard error (orange shaded region) represented by the shaded regions.

Resistance under compression

In compression tests, both materials demonstrated reductions in resistance, although their responses differed in stability and magnitude. Silskin10's initial resistance of 41.39 Ω decreased to 14.05 Ω under compression, indicating that compressive stress enhances its conductivity, as seen in figure 3. This behaviour suggests that compressive forces may compact the conductive pathways, facilitating electron flow. However, Silskin10 displayed a relatively high standard deviation of 25.29 Ω, signalling variability in performance that could arise from irregularities in particle dispersion or inconsistencies in the substrate's microstructure. To reduce this variability, further improvements in the uniformity of conductive particle distribution or the consistency of the silicone matrix could be beneficial.

Zhermack, meanwhile, exhibited a decrease in resistance from 154.74 Ω to 9.13 Ω with a notably lower standard deviation of 3.81 Ω, indicating more stable performance under compressive stress, as seen in figure 3. This consistency in Zhermack's response suggests a well-maintained conductive network that remains intact and efficient under compression, making it a suitable candidate for applications where consistent conductivity under compressive forces is essential. The low variability in Zhermack's resistance under compression points to reliable and stable performance, which is critical in settings such as wound care where materials are frequently exposed to varying pressures and must maintain steady conductive properties.

CONCLUSIONS

Overall, Silskin10 and Zhermack silicones show significant promise for use in sensors for negative pressure wound therapy (NPWT) devices, offering distinct mechanical and electrical properties. Silskin10 is ideal for static and dynamic applications, where consistent material behaviour and reliable electrical feedback are critical. Zhermack, is better suited for dynamic models that simulate the deformability of human tissue. Further research is needed to enhance the electrical stability of both materials. Refining conductive filler distribution or exploring alternative materials could improve long-term reliability. Ultimately with further material investigations, sensors could be manufactured to measure NPWT effectiveness and improve treatment outcomes.

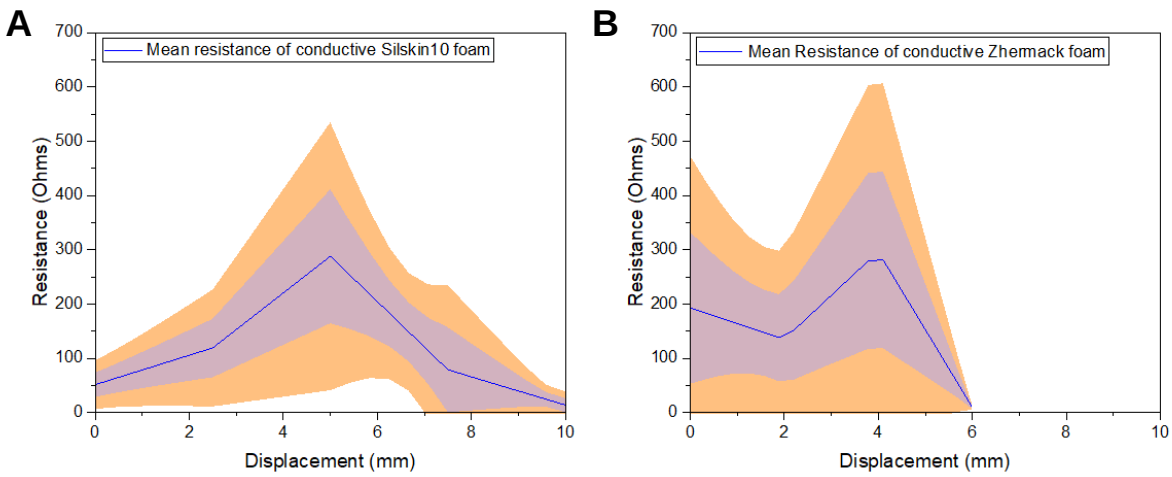

Figure 3: Mean resistance against displacement of conductive silicone foams in compression, where n=5, with standard deviation (blue shaded region) and standard error (orange shaded region) represented by the shaded regions.

REFERENCES

[1] Anghel, E. L., & Kim, P. J. (2016). Negative-Pressure Wound Therapy: A Comprehensive Review of the Evidence. (1529-4242 (Electronic)). https://doi.org/10.1097/PRS.0000000000002645

[2] Blair, M. J., Jones, J. D., Woessner, A. E., & Quinn, K. P. Skin Structure-Function Relationships and the Wound Healing Response to Intrinsic Aging. (2162-1918 (Print)).

[3] Brensing, A., Hauck, S., Ruff, R., Poppendieck, W., & Hoffmann, K.-P. (2013). Comparison of Different Conductive Fillers in Silicone for the Purpose of Replacing Metallic Conductive Structures in Flexible Implants. *Biomedizinische Technik. Biomedical engineering*. https://doi.org/10.1515/bmt-2013-4382

[4] Brownhill, V. R., Huddleston, E., Bell, A., Hart, J., Webster, I., Hardman, M. J., & Wilkinson, H. N. Pre-Clinical Assessment of Single-Use Negative Pressure Wound Therapy During In Vivo Porcine Wound Healing. (2162-1918 (Print)).

[5] Dabrowska, A. K., Rotaru, G. M., Derler, S., Spano, F., Camenzind, M., Annaheim, S., Stampfli, R., Schmid, M., & Rossi, R. M. (2016). Materials used to simulate physical properties of human skin. *Skin Res Technol*, *22*(1), 3-14. https://doi.org/10.1111/srt.12235

[6] Diridollou, S., Patat, F., Gens, F., Vaillant, L., Black, D., Lagarde, J. M., Gall, Y., & Berson, M. (2000). In vivo model of the mechanical properties of the human skin under suction. *Skin Res Technol*, 6(4), 214-221. https://doi.org/10.1034/j.1600-0846.2000.006004214.x

[7] Dowsett, C., Davis L Fau - Henderson, V., Henderson V Fau - Searle, R., & Searle, R. The economic benefits of negative pressure wound therapy in community-based wound care in the NHS. (1742-481X (Electronic)).

[8] FDA. (2018). *Class II Special Controls Guidance Document: Non-powered Suction Apparatus Device Intended for Negative Pressure Wound Therapy (NPWT)*. Retrieved from https://www.fda.gov/medical-devices/guidance-documents-medical-devices-and-radiation-emitting-products/non-powered-suction-apparatus-device-intended-negative-pressure-wound-therapy-npwt-class-ii-special#9

[9] Fortunato, M., Bellagamba, I., Tamburrano, A., & Sarto, M. S. (2020). Flexible Ecoflex®/Graphene Nanoplatelet Foams for Highly Sensitive Low-Pressure Sensors. *Sensors*, *20*(16). https://doi.org/10.3390/s20164406

[10] Gao, Y., Ota, H., Schaler, E. W., Chen, K., Zhao, A., Gao, W., Fahad, H. M., Leng, Y., Zheng, A., Xiong, F., Zhang, C., Tai, L.-C., Zhao, P., Fearing, R. S., & Javey, A. (2017). Wearable Microfluidic

Diaphragm Pressure Sensor for Health and Tactile Touch Monitoring. *Advanced Materials*, *29*(39), 1701985. https://doi.org/https://doi.org/10.1002/adma.201701985

[11] Gregor, S., Maegele, M., Sauerland, S., Krahn, J. F., Peinemann, F., & Lange, S. (2008). Negative pressure wound therapy: a vacuum of evidence? *Arch Surg*, *143*(2), 189-196. https://doi.org/10.1001/archsurg.2007.54

[12] Gu, G., Xu, H., Peng, S., Li, L., Chen, S., Lu, T., & Guo, X. (2019). Integrated Soft Ionotronic Skin with Stretchable and Transparent Hydrogel–Elastomer Ionic Sensors for Hand-Motion Monitoring. *Soft Robotics*, *6*(3), 368-376. https://doi.org/10.1089/soro.2018.0116

[13] Huang, C., Leavitt, T., Bayer, L. R., & Orgill, D. P. (2014). Effect of negative pressure wound therapy on wound healing. *Curr Probl Surg*, *51*(7), 301-331. https://doi.org/10.1067/j.cpsurg.2014.04.001

[14] Huang, Y., Peng, C., Li, Y., Yang, Y., & Feng, W. (2023). Elastomeric polymers for conductive layers of flexible sensors: Materials, fabrication, performance, and applications. *Aggregate*, *4*(4), e319. https://doi.org/https://doi.org/10.1002/agt2.319

[15] Julian, F. G., Graham, W. F., & Peter, V. (2020). Cohort study evaluating the burden of wounds to the UK's National Health Service in 2017/2018: update from 2012/2013. *BMJ Open*, *10*(12), e045253. https://doi.org/10.1136/bmjopen-2020-045253

[16] Kalra, A., & Lowe, A. (2016). An Overview of Factors Affecting the Skins Youngs Modulus. *Journal of Aging Science*, *4*(2). https://doi.org/10.4172/2329-8847.1000156

[17] Luebberding, S., Krueger N Fau - Kerscher, M., & Kerscher, M. Mechanical properties of human skin in vivo: a comparative evaluation in 300 men and women. (1600-0846 (Electronic)).

[18] Matsuda, R., Mizuguchi, S., Nakamura, F., Endo, T., Isoda, Y., Inamori, G., & Ota, H. (2020). Highly stretchable sensing array for independent detection of pressure and strain exploiting structural and resistive control. *Sci Rep*, *10*(1), 12666. https://doi.org/10.1038/s41598-020-69689-2

[19] Mulligan, S. (2011). *Negative wound pressure therapy test system* (Bristol, RI (US) Patent No. U. S. Patent.

[20] Ni Annaidh, A., Bruyere, K., Destrade, M., Gilchrist, M. D., & Ottenio, M. (2012). Characterization of the anisotropic mechanical properties of excised human skin. *J Mech Behav Biomed Mater*, *5*(1), 139-148. https://doi.org/10.1016/j.jmbbm.2011.08.016

[21] Posnett, J., & Franks, P. J. (2008). The burden of chronic wounds in the UK. (0954-7762 (Print)).

[22] Sen, C. K., Gordillo Gm Fau - Roy, S., Roy S Fau - Kirsner, R., Kirsner R Fau - Lambert, L., Lambert L Fau - Hunt, T. K., Hunt Tk Fau - Gottrup, F., Gottrup F Fau - Gurtner, G. C., Gurtner Gc Fau - Longaker, M. T., & Longaker, M. T. (2009). Human skin wounds: a major and snowballing threat to public health and the economy. (1524-475X (Electronic)).

[23] Sherif, H. A., & Almufadi, F. A. (2019). Fabrication and characterization of silicone rubber/multiwalled carbon nanotubes nanocomposite sensors under impact force. *Sensors and Actuators A: Physical*, *297*, 111479. https://doi.org/https://doi.org/10.1016/j.sna.2019.07.004

Investigation of viscoelastically active polyglycolic acid (PGA) surgical sutures

Michael H. Laughton*[1], Stanley I. Okorom[1], Kevin S. Fancey[1], Louise A. France[1]

1 University of Hull, School of Engineering, HU6 7RX, United Kingdom

**e-mail: m.h.laughton-2016@hull.ac.uk*

ABSTRACT

Surgical sutures are vital in many medical procedures and are uniquely located to promote healing within the wound. Our previous work demonstrated a simple thermo-mechanical treatment could induce a prolonged viscoelastic state in commercially available nonabsorbable polypropylene sutures, the released viscoelastic energy resulting in a positive effect on primary human skin cell (fibroblast) motility. This paper now explores the next research stage by applying the thermos-mechanical viscoelastic treatment to an absorbable polyglycolic acid (PGA) surgical suture and investigating its impact on key characteristics over a typical 42-day wound healing period. Testing indicated no significant changes in the tensile strength of PGA sutures. Differences in the elastic modulus were observed; however, the moduli remained comparable to those of other absorbable sutures. Thermal analysis found the treatment did not significantly affect the thermal characteristics and stability of the sutures, both immediately following the treatment and after an extended period. Similarly, the degradation profile of treated sutures remained consistent with those of untreated samples. These findings suggest that the thermos-mechanical viscoelastic treatment does not substantially impact the key characteristics of absorbable PGA sutures. This research demonstrates the viability of future studies to explore the application of our viscoelastic treatment to other absorbable sutures and examine the potential of viscoelastically active sutures to stimulate wound healing without compromising key absorbable suture characteristics.

Keywords: Polyglycolic acid (PGA), absorbable sutures, viscoelasticity, mechanical properties, characterisation

INTRODUCTION

Surgical sutures are a critical element of wound closure in many medical procedures, serving to support and facilitate wound healing. They expedite wound closure and provide support during the healing process by reducing bleeding, averting infections, minimising scarring, and mechanically supporting and approximating tissues together (Xu, Liu, Zhou, & Yu, 2022). The demand for suture materials is on the rise globally, reflecting the increasing number of surgical procedures (Dennis et al., 2016). Despite the availability of alternative options such as surgical staples, glues, and strips, the market trend indicates a preference for sutures, given their level of consistency, stability and versatility. Surgical Sutures account for 45-60% of the global surgical equipment market, a market with an expected valuation of $19.95 billion by 2032 (Baygar, Sarac, Ugur, & Karaca, 2019; Li et al., 2023; PrecedenceResearch, 2023; Wahlstedt, Wahlstedt, Rosenberg, & Devries, 2024).

Modern sutures are highly specialised and designed to meet the demands of a diverse surgical setting, ranging from advanced vascular neurosurgery to routine skin closure. This specialisation has been driven through the development of synthetic polymeric materials, which now lead the market. Synthetic sutures offer an extensive range of improvements, including performance, functionality, and the ability to tailor and tune materials for specific applications and responses (Lee et al., 2017). Current suture research focuses on improving wound healing through the development of new materials, creating drug-eluting sutures or advances in coating technologies (de la Harpe, Kondiah, Marimuthu, & Choonara, 2021; Li et al., 2023). Such techniques, however, often require extensive testing to ensure biocompatibility and safety. Furthermore, the research can face high economic costs and technical requirements, often making it difficult to transfer to industry and achieve commercialisation (Li et al., 2023). An alternative novel thermo-mechanical treatment developed by our group aims to stimulate wound healing by exploiting current suture materials using a more transferable methodology.

Our previous work (France & Fancey, 2021) subjected commercially available polypropylene sutures to viscoelastic deformation, resulting in the storage of viscoelastic energy. Biological findings highlighted improved cell motility and response to treated sutures due to the progressive release of this viscoelastic energy. This energy is believed to influence cellular activity in two ways: (i) mechanical stimulation through viscoelastically induced mechanotransduction (VIM) and (ii) the release of electric charges, stimulating the cell microenvironment.

The next research stage is the application of this treatment to other commercial surgical sutures to determine the broader potential of viscoelastically active sutures. One of the most prevalent suture materials is polyglycolic acid (PGA), and its derivative polyglactin 910, these being particularly favoured for their high tensile strength and adaptable degradation profiles. The absorption characteristics and degradation can be altered by modifying the synthesis /manufacturing processes to adjust their initial molecular weight, crystalline structure (amorphous-crystalline regions), and surface-to-volume ratio (Chu, 2013). This level of adaptability makes PGA and its derivatives suitable for meeting a wide range of surgical demands. This study, therefore, aims to investigate the impact of the treatment on PGA suture mechanical and thermal properties, as well as the implications on absorption and degradation.

MATERIALS & METHODS

Sample preparation & treatment process

PGA Resoquick sutures from the Resorba brand (Advanced Medical Solutions, United Kingdom) with a multifilament structure and a gauge size of 2-0 were selected for this study. This type of PGA suture offers high tensile strength and a rapid absorption profile. Sutures were opened simultaneously, designated as-received (control) and treated (test). The treatment comprised a thermo-mechanical process specifically tailored to the material adapted from (France & Fancey, 2021), consisting of low-temperature annealing followed by creep tensile loading over 24 hours to induce viscoelastic deformation. Control samples were placed adjacent to the rig, unconstrained, exposing control and test samples to the same ambient laboratory conditions (19-21°C, 45-55% RH). Characterisation of the samples from as-received and treated sutures were then examined for a period of 42 days at time intervals: day 0, day 7, day 14, day 28 and day 42.

Mechanical Characterisation

Mechanical properties were investigated through uniaxial tensile testing using an LS1 Digital Material Tester (Lloyd Instrument, Bognor Regis, United Kingdom) with a 1kN load cell. Testing protocols were adapted from both FDA and European agencies' guidelines for surgical suture testing, specifically USP 881(USP., 2018) and EU. Phr. 9.5 (Ph. Eur., 2018). Testing was conducted at an extension rate of 100 mm/min and a gauge length of 50mm, with four samples per group and time point. Captured data were processed to determine relevant suture properties: tensile strength (MPa) and elastic modulus (MPa).

Thermal Analysis

Differential scanning calorimetry was implemented to investigate the potential changes as a result of the thermo-mechanical treatment. A PerkinElmer DSC 4000 (United States) took samples from 5 to 250°C and back to room temperature (~25°C) at a rate of 10°C/min within a nitrogen atmosphere. The crystallinity (X_c) was calculated from DSC traces using the following equation in which ΔH_m is the enthalpy of melting, ΔH_m^o is the heat of fusion enthalpy of 100% crystalline polymer of pure PGA at 183.2J/g (Chen, Xie, He, & Hu, 2021; Nakafuku & Yoshimura, 2004).

$$\boldsymbol{X_c = \frac{\Delta H_m}{\Delta H_m^o} \cdot 100\%} \quad (1)$$

In-vitro Degradation

The effect of the viscoelastic treatment on the degradation properties of the PGA suture was investigated through mass retention whilst under physiologically representative conditions. Directly after treatment, as-received, annealed only and fully treated sutures were cut to 150 mm, and masses measured using an analytical balance XS105 (Mettler Toledo, United States). Individual samples were fully submerged in 13ml of phosphate buffer saline solution, PBS, pH 7.4 (Sigma-Aldrich, United States) in polypropylene falcon tubes. The samples were then stored in a fan-assisted oven to maintain a temperature of 37°C for time points: 0,7,14,28 and 42 days, with day 0 (1-hour) acting as a comparative baseline. At the end of the specified time, samples were removed from the solution, placed on filter paper and allowed to dry for an hour in ambient conditions (19-21°C,45-55% RH). The mass of each sample was measured again and the mass retention determined using the following equation:

$$\textbf{Mass Retention}\ (\%) = \frac{\boldsymbol{Final\ mass\ (mg)}}{\boldsymbol{Initial\ mass\ (mg)}} \cdot \mathbf{100} \quad (2)$$

RESULTS AND DISCUSSION

Mechanical Characterisation

Figure 1 presents the mechanical properties of as-received and viscoelastically active (treated) suture samples across the typical wound healing period of 6 weeks. Mechanical properties are one of the most critical characteristics of a surgical suture and determine clinical relevance and performance. The elastic modulus of treated samples significantly increases compared to as-received samples ($p<0.001$). This increase suggests that the treated sutures may have greater resistance to the deformation and stresses encountered within a wound. Despite this increase in treated suture stiffness, their moduli are comparable to those of other absorbable sutures, implying minimal impact on their handling properties and clinical applications (Greenwald, Shumway, Albear, & Gottlieb, 1994; Naleway, Lear, Kruzic, & Maughan, 2015). The treated suture moduli also display evidence of time-dependency, peaking at ~1.9 GPa by day 7, followed by a continuous gradual decline to ~1.6 GPa by day 42. This trend may be attributed to changes in the internal microstructure of the treated suture as the material undergoes viscoelastic recovery, subsequently leading to differences in the elastic modulus. Additionally, the complex nature of fibre interactions within a multifilament structure likely contributes to these changes. Each individual fibre may experience slight differences in recovery, the variation depending on fibre location within the braided structure. Over time, as the bulk structure undergoes recovery and relaxation, the stiffness may, therefore, decrease, as observed here.

Conversely, tensile strength remained consistent during the study, with no significant differences observed as a result of the treatment process ($p>0.05$). High tensile strength is a key attribute of PGA sutures (Li et al., 2023), often leading to its use in high-tension wounds where other materials would fail. Wound dehiscence can result from premature suture failure, often caused by high tissue tension, potential wound oedema, or external factors like patient movement (Anushya, Ganesh, & Jayalakshmi, 2022; Suzuki & Resnik, 2018). Therefore, the preservation of this property is vital to ensure the practicability and clinical relevance of viscoelastically active PGA sutures.

Thermal Properties

Table 1 summarises the thermal characteristics of as-received and treated PGA sutures over a 42-day period. The results indicate that there were no statistically significant differences between the as-received and treated samples across all investigated properties throughout the duration of the study. Whilst not statistically significant, treated samples often exhibited higher crystallinity compared to their as-received counterparts. This observation aligns with Girard et al. (Girard, Combeaud, & Billon, 2021), who investigated polymeric annealing and mechanical stretching in relation to crystallinity. Furthermore, this aligns with an earlier study exploring viscoelastically stressed nylon fibres that underwent a similar thermo-mechanical treatment (Wang & Fancey, 2018).

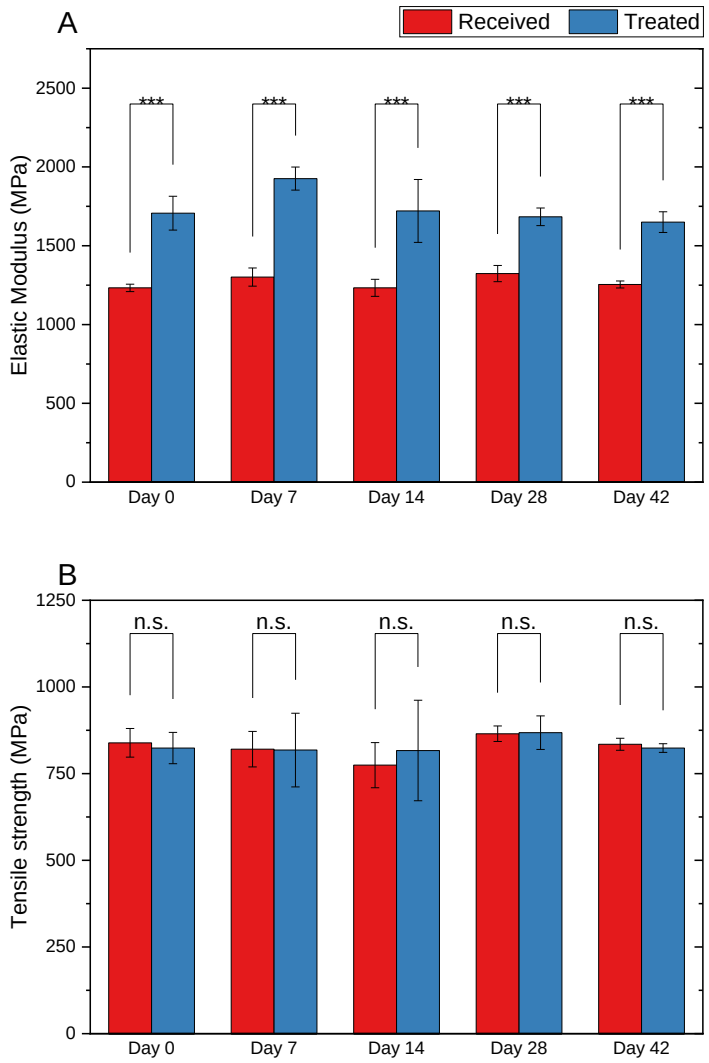

Figure 1: Mechanical properties of PGA sutures as-received and treated on Day 0, 7, 14, 28 and 42. Means presented with standard deviations for Ultimate Tensile Strength and Youngs Modulus in MPa. Two-way ANOVA Tukey-post-test *p<0.05, **p<0.01, ***p<0.001.

Crystallinity also displayed greater variability over time in comparison to melting and crystallisation temperatures, all of which lay within a 1-2°C range. Given crystallinity provides insight into the internal structures and arrangements of polymer chains, these fluctuations may imply changes occurring over the study period. Since these deviations were observed in both as-received and treated samples, the treatment is unlikely to be responsible. It is plausible that the high hygroscopic properties of the PGA material (Chu, 2013), may result in interactions with water vapour present in the laboratory environment, thereby contributing to these deviations. These findings, therefore, suggest that the thermo-mechanical treatment does not significantly alter the thermal attributes and stability of the sutures, both immediately following the treatment and after an extended period.

Table 1: Thermal properties of as-received and treated PGA sutures over 42 days. Melting and crystallisation temperatures and crystallinity are presented as mean (SD).

	Melting temperature (°C)		*Crystallisation temperature (°C)*		*Crystallinity (%)*	
	Received	*Treated*	*Received*	*Treated*	*Received*	*Treated*
Day 0	226.11 (0.26)	226.85 (0.08)	182.98 (2.18)	181.41 (0.25)	48.84 (2.09)	52.75 (3.12)
Day 7	226.84 (0.33)	226.92 (0.26)	181.12 (1.06)	181.69 (0.36)	50.29 (4.93)	47.27 (2.97)
Day 14	226.40 (0.91)	226.87 (0.73)	180.70 (3.54)	181.94 (0.55)	56.85 (9.65)	56.37 (5.88)
Day 28	227.28 (0.23)	227.09 (0.43)	182.39 (1.75)	181.96 (0.31)	51.40 (0.53)	55.05 (1.54)
Day 42	227.02 (0.52)	226.28 (0.26)	182.30 (0.16)	182.62 (0.44)	55.47 (2.71)	56.90 (1.89)

Degradation Study

Degradation behaviour of PGA as-received, annealed-only and fully treated (annealed and creep loaded) samples are summarised in Figure 2. The primary degradation mechanism of PGA sutures is hydrolysis, where water molecules infiltrate into material and cleave the ester linkages (Manoukian et al., 2019). The increase in mass at day 7 demonstrates this initial uptake of water as the material swells and water molecules penetrate deep into the multifilament structure and into the material of individual fibre filament. Following this initial increase, a gradual decline in mass occurs during the remaining days across all sample groups.

Browning and Chu (Browning & Chu, 1986) investigated the effect of annealing (≥150°C) on the degradation properties of PGA sutures, finding a significant increase in the rate of hydrolytic degradation. This study used low-temperature annealing to minimise this and included annealed-only samples for a control-comparison. Although not statistically significant, annealed samples exhibit the greatest difference in mass retention in Figure 2, equating to a ~7% greater loss in mass by day 42. Annealing can increase chain mobility, which may have facilitated greater water penetration, thereby leading to increased hydrolysis, degradation and mass loss.

The viscoelastic suture samples (treated) differ from the annealed samples, sharing a closer degradation profile with as-received samples. This suggests that the mechanical stage of the treatment process may counteract changes caused by annealing alone. It can be speculated that mechanical stretching increases the orientation of polymer chains along the fibre axis, leading to the crystalline regions being orientated parallel to the surface (and axis) and acting as a protective barrier for the less dense amorphous regions (Browning & Chu, 1986).

The masses of as received and treated sutures did not display statistically significant differences across each timepoint ($p>0.05$), indicating that the degradation rate of viscoelastically active sutures is unaffected by the overall thermo-mechanical treatment. It may therefore be suggested that treated sutures could be used in the same clinical indices and cases as the current short-term absorbable PGA sutures with similar degradation profiles and expectations.

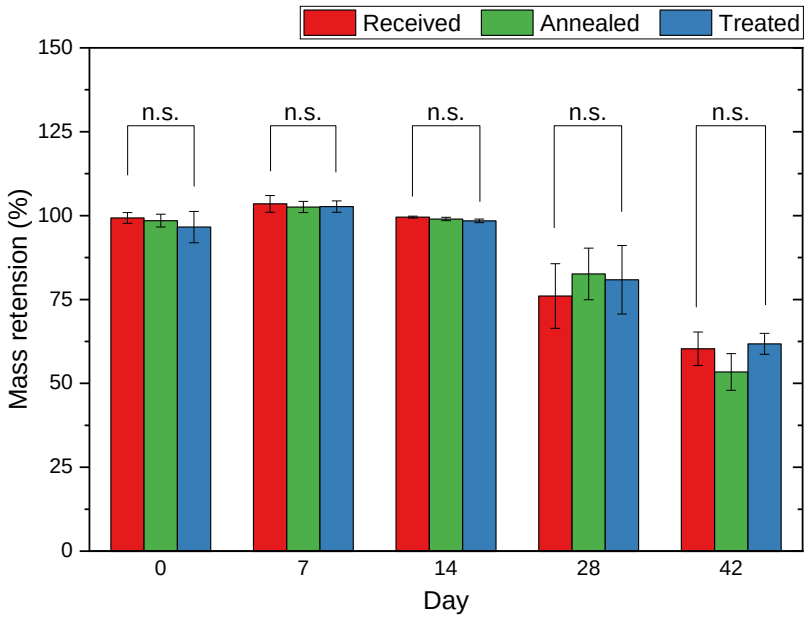

Figure 2: Mass retention of PGA sutures for received, annealed-only and treated across the 42-days. Means are presented with error bars representing standard error of means. Two-way ANOVA Tukey-post-test *p<0.05, **p<0.01, ***p<0.001.

CONCLUSIONS

In order to enhance the understanding of viscoelastically active sutures, this paper has examined the impact of our thermo-mechanical treatment on the mechanical, thermal, absorption, and degradation properties of viscoelastically active polyglycolic acid (PGA) sutures. The results indicate no significant changes in the high tensile strength and performance of PGA sutures. Differences in the elastic modulus were observed, which may be attributed to changes in the internal structure; however, the moduli remain comparable to those of other absorbable sutures. Thermal analysis indicates the treatment does not significantly affect the thermal characteristics and stability of the sutures, both immediately following the treatment and after an extended period (42 days). Similarly, the degradation profile and rate of treated sutures remained consistent with those of untreated samples (as-received, as-packaged). These findings suggest that the viscoelastic treatment does not substantially impact the key characteristics of rapidly absorbable PGA sutures. This research demonstrates the viability of future studies to explore the application of the viscoelastic treatment to other absorbable sutures and examine the potential of viscoelastically active sutures to stimulate wound healing without compromising key absorbable suture characteristics.

REFERENCES

[1] Anushya, P., Ganesh, S. B., & Jayalakshmi, S. (2022). Evaluation of tensile strength of surgical absorbable and nonabsorbable suture materials after immersion in different fruit juices: An in vitro study. *J Adv Pharm Technol Res, 13*(Suppl 1), S108-S111. doi:10.4103/japtr.japtr_267_22

[2] Baygar, T., Sarac, N., Ugur, A., & Karaca, I. R. (2019). Antimicrobial characteristics and biocompatibility of the surgical sutures coated with biosynthesized silver nanoparticles. *Bioorg Chem, 86*, 254-258. doi:10.1016/j.bioorg.2018.12.034

[3] Browning, A., & Chu, C. C. (1986). The effect of annealing treatments on the tensile properties and hydrolytic degradative properties of polyglycolic acid sutures. *Journal of Biomedical Materials Research, 20*(5), 613-632. doi:https://doi.org/10.1002/jbm.820200507

[4] Chen, Y., Xie, K., He, Y., & Hu, W. (2021). Fast-Scanning Chip-Calorimetry Measurement of Crystallization Kinetics of Poly(Glycolic Acid). *Polymers, 13*(6), 891. doi:10.3390/polym13060891

[5] Chu, C. C. (2013). Materials for absorbable and nonabsorbable surgical sutures. In *Biotextiles as Medical Implants* (pp. 275-334).

[6] de la Harpe, K. M., Kondiah, P. P. D., Marimuthu, T., & Choonara, Y. E. (2021). Advances in carbohydrate-based polymers for the design of suture materials: A review. *Carbohydr Polym, 261*, 117860. doi:10.1016/j.carbpol.2021.117860

[7] Dennis, C., Sethu, S., Nayak, S., Mohan, L., Morsi, Y., & Manivasagam, G. (2016). Suture materials - Current and emerging trends. *Journal of biomedical materials research. Part A, 104*(6), 1544-1559. doi:10.1002/jbm.a.35683

[8] France, L. A., & Fancey, K. S. (2021). Viscoelastically active sutures - A stitch in time? *Mater Sci Eng C Mater Biol Appl, 121*, 111695. doi:10.1016/j.msec.2020.111695

[9] Girard, M., Combeaud, C., & Billon, N. (2021). Effects of annealing prior to stretching on strain induced crystallization of polyethylene terephthalate. *Polymer, 230*, 124078. doi:10.1016/j.polymer.2021.124078

[10] Greenwald, D., Shumway, S., Albear, P., & Gottlieb, L. (1994). Mechanical Comparison of 10 Suture Materials before and after in Vivo Incubation. *Journal of Surgical Research, 56*(4), 372-377. doi:https://doi.org/10.1006/jsre.1994.1058

[11] Lee, E. J., Huh, B. K., Kim, S. N., Lee, J. Y., Park, C. G., Mikos, A. G., & Choy, Y. B. (2017). Application of Materials as Medical Devices with Localized Drug Delivery Capabilities for Enhanced Wound Repair. *Prog Mater Sci, 89*, 392-410. doi:10.1016/j.pmatsci.2017.06.003

[12] Li, Y., Meng, Q., Chen, S., Ling, P., Kuss, M. A., Duan, B., & Wu, S. (2023). Advances, challenges, and prospects for surgical suture materials. *Acta Biomater, 168*, 78-112. doi:10.1016/j.actbio.2023.07.041

[13] Manoukian, O. S., Sardashti, N., Stedman, T., Gailiunas, K., Ojha, A., Penalosa, A., . . . Kumbar, S. G. (2019). Biomaterials for Tissue Engineering and Regenerative Medicine. In (pp. 462-482): Elsevier.

[14] Nakafuku, C., & Yoshimura, H. (2004). Melting parameters of poly(glycolic acid). *Polymer, 45*(11), 3583-3585. doi:10.1016/j.polymer.2004.03.041

[15] Naleway, S. E., Lear, W., Kruzic, J. J., & Maughan, C. B. (2015). Mechanical properties of suture materials in general and cutaneous surgery. *J Biomed Mater Res B Appl Biomater, 103*(4), 735-742. doi:10.1002/jbm.b.33171

[16] Ph. Eur., T. E. P. (2018). Ph. Eur. - Sutures Sterile Synthetic. In.

[17] PrecedenceResearch. (2023). Surgical Equipment Market (By Product: Surgical Sutures & Staplers, Handheld Surgical Device, and Electrosurgical Devices; Application: Neurosurgery, Wound Care, Obstetrics & Gynecology, Cardiovascular, Orthopedic, Plastic & Reconstructive Surgery, and Others)—Global Industry Analysis, Size, Share, Growth, Trends, Regional Outlook, and Forecast 2023–2032. Retrieved from https://www.precedenceresearch.com/surgical-equipment-market

[18] Suzuki, J. B., & Resnik, R. R. (2018). 11 - Wound Dehiscence: Incision Line Opening. In R. R. Resnik & C. E. Misch (Eds.), *Misch's Avoiding Complications in Oral Implantology* (pp. 402-439): Mosby.

[19] USP., T. U. S. P., The National Formulation. (2018). USP <881> - Sutures – Tensile Strength. In.

[20] Wahlstedt, E. R., Wahlstedt, J. C., Rosenberg, J. S., & Devries, C. R. (2024). Lifecycle of surgical devices: Global, environmental, and regulatory considerations. *World Journal of Surgery*. doi:10.1002/wjs.12140

[21] Wang, B., & Fancey, K. S. (2018). Viscoelastically prestressed polymeric matrix composites: An investigation into fibre deformation and prestress mechanisms. *Composites Part A: Applied Science and Manufacturing, 111*, 106-114. doi:10.1016/j.compositesa.2018.05.013

[22] Xu, L., Liu, Y., Zhou, W., & Yu, D. (2022). Electrospun Medical Sutures for Wound Healing: A Review. *Polymers (Basel), 14*(9). doi:10.3390/polym14091637

Coevolution and the Mass Ratio Effect in Automotive Safety Research

C E Neal-Sturgess

Emeritus Professor of Mechanical Engineering University of Birmingham

Visiting Professor Transport Safety and Simulations Research Coventry University.

ABSTRACT

An estimated 1.35 million people globally lose their lives in road crashes annually. An important variable in the collision between two vehicles is the relative masses of each of the two vehicles, this is known as the mass Ratio effect and is the subject of this paper.

In their paper Natural selection for least action (Kaila and Annila 2008) they depict evolution as a process conforming to the Principle of Least Action (PLA). From this concept, together with the Coevolution model of Levin and Lewontin, an equation of motion for coevolution in car crash is derived which shows that it is the time rate of change of Momentum ($\Delta V/t$) that determines the average force in the collision.

BACKGROUND

An estimated 1.35 million people globally lose their lives in road crashes annually, according to the World Health Organization (WHO). Road traffic injuries are the eighth leading cause of death globally, impacting all age groups but disproportionately affecting children and young adults aged 5-29. Low- and middle-income countries bear the brunt of the burden, accounting for 93% of global road traffic deaths despite having only 60% of the world's vehicles

Lagrangian mechanics have been the bedrock of analytical science since the work of Euler and Lagrange in the field of calculus of variations in the late 18th Century [Weisstein]. Lagrangian mechanics is based on the Principle of Least Action (PLA), again from the 18th century The principle states that the path taken by a system between events at times t_1 and t_2 and configurations q_1 and q_2 in space-time is the one for which the action is stationary (no change) to the first order and enables the unique equations of motion of the system to be derived. As far as is known all physical systems follow the PLA. It covers all scales of systems from Quantum mechanics through real-world mechanics to Cosmology and also applies to biological systems [D.T. Pham1 and Z.E. Musielak].

Lagrangian mechanics caused much philosophical debate in the 19th and 20th centuries as it appeared to imply there is no free will. This was clarified by the work of Richard Feynman in deriving Quantum Electrical Dynamics (QED), where he derived the concept of “the sum over all histories” [Feynman 1985].

Levin and Lewontin proposed the principle of “Coevolution ” in 1983 [Levin and Lewontin 1983]. Their description of Coevolution as two, coupled, differential equations to express the interaction between the two variables

$$\frac{d}{dt}(C_1) = j(C_1, C_2) \quad (1)$$

And

$$\frac{d}{dt}(C_2) = g(C_1, C_2) \quad (2)$$

was an interesting development. Levin and Lewontin 1985 stated that solving these differential equations would be very difficult. Taking the idea that the second law can be rewritten as an equation of motion [Kaila and Annila 2008] and if Lagrangian's can be defined as:

$$\mathcal{L}_{C1} = \mathrm{F}\{j(C_1, C_2)\} \quad (3)$$

$$\mathcal{L}_{C2} = \mathrm{F}\{g(C_1, C_2)\} \quad (4)$$

Then to find the unique trajectory in space-time [Neal-Sturgess 2021] by using the calculus of variations through Euler-Lagrange [Goldstein 1969] to find an equation of motion for a coupled system gives:

$$\frac{d}{dt}\mathcal{L}_{C1} f\{F(C_1, C_2)\} - \mathcal{L}_{C2} G\{C_1, C_2\} = 0 \quad (5)$$

Hence $\frac{d}{dt}\mathcal{L}_{C1} f\{F(C_1, C_2)\} = \mathcal{L}_{C2} G\{C_1, C_2\}$ (6)

Lagrangians are, in general scalars, however for the special case of "Free Particles" they can be dfined in terms of energy or momentum [Goldstein]. Defining a two vehicle collision as free particles then this description can be used.

As this description is for a two vehicle collision, then the Lagrangians can be reversed giving for the second vehicle:

$$\frac{d}{dt}\mathcal{L}_{C2} G\{C_1, C_2\} = \mathcal{L}_{C1} f\{F(C_1, C_2)\} \quad (7)$$

The Lagrangians will be difficult to define, but it is probable that they will contain a potential term (V), and a kinetic term (T)_ If a two-car collision occurs in plane motion

the potential term is a constant whereas the kinetic term will be dominant; so equations (3) and (4) can be considered solely a function of velocity.

As in general Lagrangians are scalar quantities however for a “Free Particles” Lagranians, can be defined as either Energy or Momentum, which are vector quantities and related [Goldstein]. Choosing Kinetic Energy led to an equation that is only correct for $2m_1=m_2$, however choosing momentum gives: equation (6) becomes

$$\frac{d}{dt}\mathcal{L}_{C1}f\{m_1 \,.\, v_1\} = \mathcal{L}_{C2}G\{k.m_2 \,.\, v_2\} \qquad (8)$$

Hence

$$m_1 \,.\, a_1 = km_2\Delta v_2 \qquad (9)$$

Let $k={}^{1}/_{t}$

hence

$$m_1 \,.\, a_1 = \frac{1}{t}\, m_2\Delta v_2 = m_2\, a_2 \qquad (10)$$

Which gives the well known “Mass Ratio” equation [Shelby 2011]. When two vehicles collide the relative masses of the vehicles is an important parameter, no more so than in a head-on collision. For this the mass ratio equation based on conservation of momentum.

$$m_1\Delta V_1 = m_2\Delta V_2 \qquad (11)$$

Where ΔV is the change in velocity.

When two vehicles of different mass collide, if the lighter vehicle is travelling from left to right and the heavier vehicle is travelling from the right to the left, if after the collision both vehicles have zero velocity, then the lighter vehicle originally travelling left to right will, in the later stages of the collision, be travelling right to left and the two velocities will add together. This means that the change in velocity of the lighter vehicle is higher than the change in velocity of the heavier vehicle, therefore:

$$\frac{m_2}{m_1}\Delta V_2 = \Delta V_1 \quad (12)$$

This is an important parameter in the collision of Petrol/Diesel vehicles (PDV's) with Electric Vehicles (EV's) as in general EV's are heavier than PDV's.

To consider these effects, taking an extreme case:

Let $m_1 = a\ Ford\ KA = 865kg$ and

let $m_2 = a\ JLR\ iPACE = 2{,}208\ kg$

so $\frac{m_2}{m_1}\Delta V_2 = \frac{2{,}208}{865} = 2.54\Delta V_1 \quad (13)$

Now the Abbreviated Injury Score (AIS), which is a scale of 1-6, where 6 is unsurvivable, is proportional to ΔV^3 for restrained occupants [Neal-Sturgess et.al 2001]

Hence for this case $AIS_1 = 16.4AIS_2 \quad (14)$

This would mean that the injuries in the KA would be fatal.

Taking a more mid-range example, the mass of the average family saloon is

1500kg (m_1), compared to a Tesla Model Y Performance (2,003 kg) which gives:

$$\frac{m_2}{m_1}\Delta V_2 = \frac{2{,}003}{1500} = 1.33\Delta V_1 \quad (15)$$

Hence AIS_1 = 2.35 AIS_2 and so this would move an AIS_1 of 2 to 4.7 (approximately 5) which is probably nearly fatal.

DISCUSSION

In a recent article subtitled "The EV Obesity Epidemic" in The Economist, [17 Aug 2023] an argument is made that EV shoppers who not just insist, but demand auto manufacturers to supersize their EV's today are practically dooming other car owners from making the switch-over.

As the age of the vehicle fleet in the UK is around 12-15 years, and the change-over date of 2035 (2030 if Labour wins GE 14th February 2024) so for that length of time and until 2050 there will be a diminishing but still large proportion of petrol/diesel vehicles in the

fleet; and hence increased injury severity. Therefore, from the analysis above, all across the range of vehicle types the mass ratio effects of the heavier electric vehicles will significantly affect the injury severities observed, and vehicle manufacturers should be encouraged to reduce the weight of electric vehicles. In addition to the economic effects from a safety point of view it is in an individual's interest to change to an electric vehicle.

The safety testing of the interactions between Petrol/diesel vehicle is in its early stages but some work has been conducted. The safety of electric vehicles has been examined by O'Malley et.al [O'Malley et.al. 2015] which concentrated on fire risk of EV's, which is now deemed to be low. Chen et.al in an early analysis [Chen et.al. 2015] examined both hybrid and conventional vehicles and found at that time there was little difference between the two, although it was a small sample study. The effect of the mass-ratio has been of interest to the Insurance Institute for Highway Safety (IIHS) for some time, in contrast to the National ~Highway Transportation Safety Administration (NHTSA) who only test vehicles of similar mass. The IIHS website [iihs.org 04/01/2-24] has a section on the safety of electric vehicles and an article by Raul Arbelaez concentrates on the effect of the mass of EV's, and concludes that the effects of the generally heavier mass of electric vehicles (although there are lightweight EV's i.e. Nissan Leaf) because of range extending will increase the severity of injury of occupants of petrol/diesel vehicles in collision with heavier EV's.

This is a theoretical paper projecting what is likely to happen in the future and it is, of yet, too early to compare the projections with real world crashes, but it will be interesting to see the effects in the future.

CONCLUSIONS

All across the range of vehicle types in the fleet the mass ratio effects of the heavier electric vehicles will significantly affect the injury severities observed up to 2045, and vehicle manufacturers should be encouraged to reduce the weight of electric vehicles in the interim time period.

REFERENCES

[1] WHO Global Survey, 3rd December 2023

[2] CRC Concise Encyclopedia of Mathematics (2nd Edition) Weisstein

[3] Classical Mechanics Goldstein 1969

[4] Lagrangian Formalism in Biology: I. Standard Lagrangians and their Role in Population Dynamics (2022) D.T. Pham1 and Z.E. Musielak.

[5] Feynman, R.P.(1985). QED:The Strange Theory of Light and Matter, Penguin

[6] Levin R, Lewontin R. The dialectical Biologist. 1985. University of Harvard.

[7] Nahin, PJ. When Least is Best, Princeton UP(2004).

[8] Neal-Sturgess 2022 A Differential Equation for Mutation Rates in Environmental Coevolution, Journal of the Environment and Public Health

[9] Kaila VRI, Annila A. Natural selection for least action. Proc.R. Soc A (464) (2008): 3055-3070

[10] Read, J., & Teh, N. (Eds.). (2022). *The Philosophy and Physics of Noether's Theorems: A Centenary Volume*. Cambridge: Cambridge University Press. doi:10.1017/9781108665445.

[11] Shelby S G : Delta-v as a measure of traffic conflict severity 3rd International Conference on Road Safety and Simulation, September 14-16, 2011, Indianapolis, USA

[12] Neal-Sturgess C E, Hassan A and Cuerden R: The relationship of AIS to Peak Virtual Power. AAAM 2001

[13] The Economist, [17 Aug 2023]

[14] Crashworthiness Testing of Electric and Hybrid Vehicles: O'Malley S, Zuby D, Moore M, Paine M, Paine D. 24th International Technical Conference on the Enhanced Safety of Vehicles (ESV). Gothenburg , Sweden. 2015

[15] Chen R, Choi K S, Daniello A, Gabler H. An Analysis of Hybrid and Electric Vehicle Crashes in the U.S. 24th International Technical Conference on the Enhanced Safety of Vehicles (ESV): Gothenburg , Sweden 2015.

A Novel Anthropomorphic Biomechanical Model of the Human Body: a Pedestrian-Car Impact Study

Giulia Pascoletti[1], Giordano Franceschini[1], Elisabetta M. Zanetti[1]

[1] *University of Perugia, Department of Engineering, Perugia (ITALY), 06125*

ABSTRACT

Articulated Total Body (ATB) models are commonly used for kinematic analysis, and the outer body geometry is usually a rough approximation of the actual one. This study moves from the hypothesis that a more accurate representation can be used with minimal additional effort in model preparation and computation, while it can bring significant benefits especially in circumstances where the human body undergoes multiple impacts with the outer environment. This anthropomorphic model was previously set up by the authors, and it is obtained from a statistical shape model of a human being which is morphed according to a limited set of measurements such as the height, the weight, the waist circumference, the shoulder width, etc.; the geometric accuracy of the anthropomorphic geometry has resulted to be below 9 mm. The model was here validated against tests performed on cadavers, using specific indices to compare time histories between numerical and experimental data (EEARTH metrics). Some preliminary validation tests, considering experimental tests reproducing pedestrian-car impacts, have shown the capabilities of the model in predicting the actual trajectories. Further efforts will be dedicated to a refinement and customization of contact properties to be applied for impacts between body parts and the environment.

Keywords: anthropomorphic human model, ATB model, statistical shape model, multibody analysis, impacts, car accidents, time histories

Introduction

Articulated Total Body (ATB) models are multibody (MB) models commonly used for the kinematic simulation of the human body behaviour following a fall (de Vette et al. 2024), a car accident (Yang et al. 2006), and various impacts scenarios (Fréchède and McIntosh 2009) related to forensic investigations (de Vette et al. 2024), as well as the mechanical design of protective devices (McNally and Whitehead 2013) or for safety considerations (Sun et al. 2023). In the development of these models, major emphasis has been placed on the accurate replica of mass and inertial properties of the body segments; secondly, also the passive resistive properties of articular joints have been inquired. On the contrary the accurate reproduction of the outer geometry was often overlooked, being considered of minor relevance on the system's outcomes.

However, technologies allowing accurate body scanning are nowadays pretty common (Xhimitiku et al. 2022) and also the mathematical background to set up parametric models of complex shapes, such as the human body, is well established (Huysmans et al. 2020) and has driven to set up statistical shape models already used by ergonomic designers (Danckaers et al. 2019) or by fashion designers (Scataglini et al. 2019). The first option might be of interest when the inquiry is focused on a specific subject whose body is available to be scanned; on the contrary, the second option can be used to predict the outer body geometry through a limited number of input variables corresponding to anthropometric measurements, or whenever a whole population of subjects should possibly be simulated.

The University of Delft has recently set up a statistical shape model of the outer human body (Huysmans et al. 2020), which can be used for ergonomic or fashion design. This model can accept up to 24 input variables, taken from standard anatomic measurements: the weight and the height remain basic input data, and other information can be added such as shoulder width, waist circumference, breast width etc.

Taking this model as a starting point, the writing authors have set up a completely automatic workflow aimed to obtain a multibody model of the human body (Pascoletti et al. 2023). This workflow is described

in detail in (Pascoletti et al. 2022) and it includes: identifying anatomical segmentation planes to separate body parts; calculating inertial properties of each parts; localising physiologic joints with the assignment of degrees of freedom and passive stiffness properties. In these research activities, the benefit coming from the implementation of a more accurate geometric reconstruction has been investigated comparing numerical results obtained with the new anthropomorphic model to the classical ellipsoids-based modelling approach. In particular, numerical simulations replicating a free fall from a height and a fall from a balcony were used as case studies. The results have shown that the proper modelling of the external geometry has a major impact on the simulation's outcomes, especially when the interaction with the external environment has to be considered.

Having so proved the relevance and effects of an anthropomorphic multibody model approach, the study here presented is aimed at providing a first validation of the model, using data in literature (Shang et al. 2020) concerning experimental tests of pedestrian-to-car impact. A significant effort is here paid to establish quantitative indices, able to assess the faithful replication of time histories.

MATERIALS & METHODS

The statistical shape model

The geometric model has been taken form the statistical shape model developed at Delft University (Huysmans et al. 2020); this model allows to predict the actual external shape of the human body with an accuracy equal to 9.24 ± 2.25 mm. It is parametrised on 24 anthropometric measurements but they are not all needed: the model accepts whatever number of known measures. All geometric models share the same mesh topology (Pascoletti et al. 2023) and include additional nodes in correspondence of skin body landmarks.

The multibody model

The individual solid bodies corresponding to parts of the human body are obtained from the whole external geometry using segmentation planes. These planes are automatically individuated based on skin body landmarks. Once the whole body is segmented in 17 components (Pascoletti et al. 2023) (figure 1a), joints' positions are automatically located, based on anatomic landmarks; the respective degrees of freedom and passive stiffnesses have been established based on literature and were reported in detail in a previous work (Pascoletti et al. 2019). Inertial properties are assigned assuming a uniform density for the whole body volume, obtained from the ratio between the weight and the total volume enclosed by the body mesh:

$$\rho_{body} = \frac{Subject\ Weight}{Total\ Body\ Volume}$$

The multibody model was setup using Adams (Hexagon Adams Software rel. 17).

Simulations

Simulations were finalised to replicate the actual experimental setup in order to validate the model. In these simulations, the anthropomorphic model replicating each cadaver was created, based on anthropometric data of the five cadavers used for these tests. The articulated total body was kept suspended at the head up to the first impact with a car. The initial body position was not known exactly, and it was replicated based on photographic documentation of experimental tests (figure 1b).

The profile of the impacting cars (three different models were investigated) was retrieved on the web and the volume of the car was created as an extrusion of this profile. The cars advanced at constant speeds between 20 – 30 km/h.

Contact forces were implemented between each body segment and the environment, that is the car and the ground geometries.

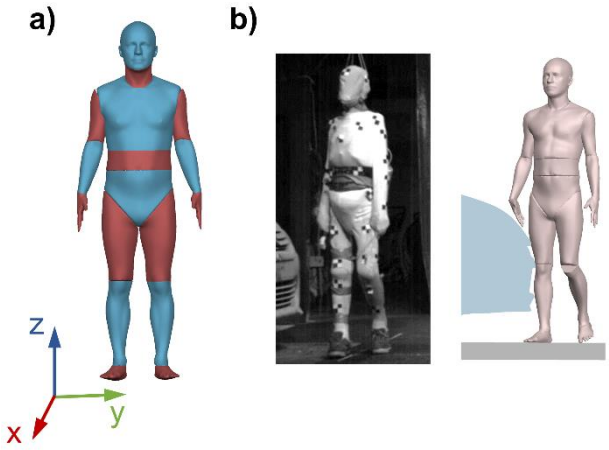

Figure 1: a) Anthropomorphic ATB model; b) Example of MB model initial configuration (test 4)

The output of the analysis was the mechanisms of impact of the whole cadaver, which was compared to the one retrievable in literature (Crocetta et al. 2015) for a qualitative check. Secondly, detailed data concerning the head trajectory and velocity were used for a quantitative validation, according to the only numerical data which have been publicly shared on the web (Shang et al. 2020).

Experimental and numerical time histories were compared making use of a specific metric, the EEARTH metric E (Zhan, Fu, and Yang 2011), commonly used for assessing the agreement between two time histories.

Using both qualitative and quantitative outcomes, it was possible to highlight the strengths and criticisms of the MB model and optimize respective modelling parameters.

RESULTS AND DISCUSSION

First of all, the impact kinematics was assessed for all the simulations and compared at relevant time instants with the experimental results. Figure 2 shows an example of this comparison for test 4.

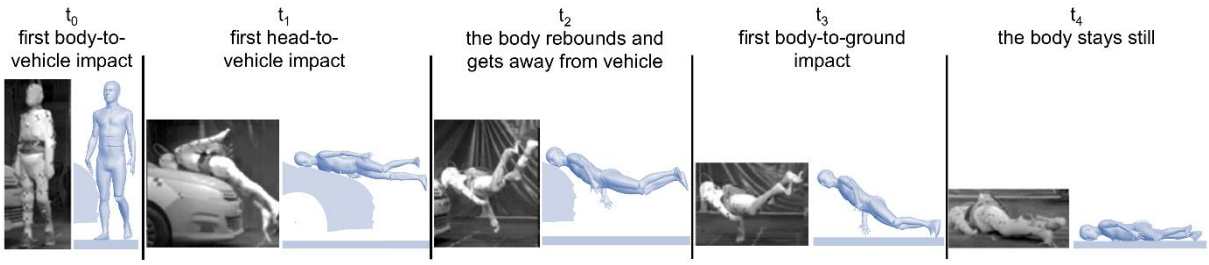

Figure 2: Global kinematic comparison (test 4)

The same mechanisms of impact as in the cadavers' tests were obtained with the multibody model, capturing so the whole impact phenomenon.

With reference to the local kinematics, data obtained for the head centre of mass were analysed. The comparison of the time histories showed a good agreement for the displacement parameters (horizontal and vertical) with values of the E metric around 80%. Also the horizontal velocity seemed to be comparable between numerical and experimental results, having reported 65% as the lowest E value. On the other side, metric's values below 50-60% were observed for the horizontal head's velocity, highlighting the need of further investigating multibody model parameters.

More specifically, the time histories of these velocity component were further investigated, and it was pointed out that the major differences between numerical and experimental data were related to the two main peaks, representing the impact of the head and the ground respectively.

These peaks were mainly affected by the interaction between the head segment geometry and the respective environment geometries. The way these bodies interact is governed by the definition of the contact forces that are based on the implementation of some contact parameters into the multibody software. As first attempt, these parameters were defined based on some information found in literature, and then an optimization was performed in order to see if the numerical response could be improved.

Different contact parameters combinations have been tested and respective numerical results compared to experimental ones. Figure 3 reports and example of this optimization process for test 4, showing that at the end of the analysis the horizontal velocity curve was closer to the experimental time history, and particularly peaks are in a better agreement.

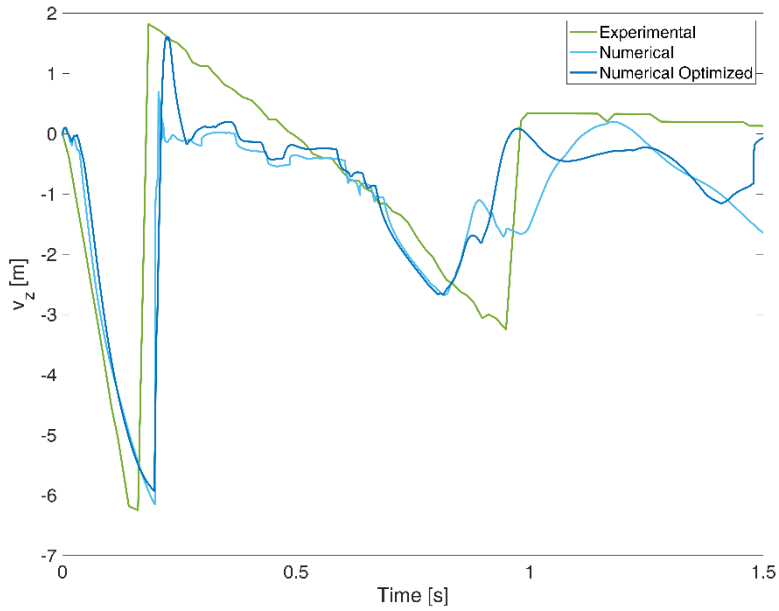

Figure 3: Horizontal velocity optimization (Test 4)

The optimized curves were compared quantitatively using the E metric, which improved for all the tests. Table 1 reports these results, pointing out that the only test which was not possible to significantly improve in terms of horizontal velocity was test 3. The reason of this disagreement between experimental and numerical data was related to the fact that during the test on this cadaver, the impact between the head and the car was not detected. This could be related to the failure to identify the experimental impact using the head accelerometer data.

Table 1: E and E_{opt} scores for the horizontal velocity parameter

Test	***E***	E_{opt}
1	75%	73%
2	66%	72%
3	46%	48%
4	71%	73%
5	52%	75%

On the overall, the contact parameter that mainly affected the interaction was found to be the damping coefficient; lower values of damping resulted in a better response of the head interaction, being able also to simulate the rebound effect due to the impact with the windshield.

CONCLUSIONS

In this work a novel approach to the multibody modelling of the human body was presented, introducing an anthropomorphic ATB model. In previous studies of the authors, it was assessed the relevance of properly replicating the external human shape, whenever the interaction with the external environment is significant. Based on this, the anthropomorphic multibody model could represent an effective tool for the investigation and the reconstruction of accidents.

A first validation of the model response under external impact loading conditions was here sought, considering experimental data coming from cadavers' tests. Five different scenarios replicating the pedestrian-car impact were replicated and the results have shown that the proposed ATB model was able to properly capture and replicate the full kinematics of impact. Moreover, not only the global kinematic was considered, but also the local response of the head segment. Corresponding kinematic parameters proved to be in agreement with the experimental one, while the vertical velocity response was found to be affected by the major differences with respect to experimental data. The EEARTH metric was here implemented for the analysis and comparison of the experimental and numerical time histories, and it was also used to improve the multibody model parameters, in particular setting up the head contacts' inputs.

The proposed model has shown its capability to offer accurate information on kinematics impact, making it a promising numerical tool for accident reconstruction and injury assessment.

REFERENCES

[1] Crocetta, Gianmarco, Simone Piantini, Marco Pierini, and Ciaran Simms. 2015. "The Influence of Vehicle Front-End Design on Pedestrian Ground Impact." *Accident Analysis and Prevention* 79:56–69. doi: 10.1016/j.aap.2015.03.009.

[2] Danckaers, Femke, Toon Huysmans, Ann Hallemans, Guido De Bruyne, Steven Truijen, and Jan Sijbers. 2019. "Posture Normalisation of 3D Body Scans." *Ergonomics* 62(6):834–48. doi: 10.1080/00140139.2019.1581262.

[3] Fréchède, Bertrand, and Andrew S. McIntosh. 2009. "Numerical Reconstruction of Real-Life Concussive Football Impacts." *Medicine and Science in Sports and Exercise* 41(2):390–98. doi: 10.1249/MSS.0B013E318186B1C5.

[4] Huysmans, Toon, Lyè Goto, Johan F. M. Molenbroek, and Richard Goossens. 2020. "DINED Mannequin." *Tijdschrift Voor Human Factors* 45(1):4–7.

[5] McNally, D. S., and S. Whitehead. 2013. "A Computational Simulation Study of the Influence of Helmet Wearing on Head Injury Risk in Adult Cyclists." *Accident; Analysis and Prevention* 60:15–23. doi: 10.1016/J.AAP.2013.07.011.

[6] Pascoletti, G., T. Huysmans, J. F. M. Molenbroek, and E. M. Zanetti. 2023. "From an Ellipsoid-Based to an Anthropomorphic Articulated Total Body Model for Multibody Applications." *International Journal on Interactive Design and Manufacturing*. doi: 10.1007/s12008-023-01427-0.

[7] Pascoletti, Giulia, Daniele Catelani, Paolo Conti, Filippo Cianetti, and Elisabetta M. Zanetti. 2019. "A Multibody Simulation of a Human Fall: Model Creation and Validation." *Procedia Structural Integrity* 24:337–48. doi: 10.1016/j.prostr.2020.02.031.

[8] Pascoletti, Giulia, Toon Huysmans, Paolo Conti, and Elisabetta M. Zanetti. 2022. "Evaluation of a Morphable Anthropomorphic Articulated Total Body Model." Pp. 761–72 in *Design Tools and Methods in Industrial Engineering II*, edited by C. Rizzi, F. Campana, M. Bici, F. Gherardini, T. Ingrassia, and P. Cicconi. Cham: Springer International Publishing.

[9] Scataglini, Sofia, Femke Danckaers, Robby Haelterman, Toon Huysmans, Jan Sijbers, and Giuseppe Andreoni. 2019. “Using 3D Statistical Shape Models for Designing Smart Clothing.” *Advances in Intelligent Systems and Computing* 822:18–27. doi: 10.1007/978-3-319-96077-7_3.

[10] Shang, Shi, Catherine Masson, David Teeling, Max Py, Quentin Ferrand, Pierre Jean Arnoux, and Ciaran Simms. 2020. “Kinematics and Dynamics of Pedestrian Head Ground Contact: A Cadaver Study.” *Safety Science* 127(January). doi: 10.1016/j.ssci.2020.104684.

[11] Sun, Wenbo, Jiacheng Liu, Jingwen Hu, Judy Jin, Kevin Siasoco, Rongrong Zhou, and Robert Mccoy. 2023. “Adaptive Restraint Design for a Diverse Population through Machine Learning.” *Frontiers in Public Health* 11. doi: 10.3389/FPUBH.2023.1202970.

[12] de Vette, Vera, Kim Hutchinson, Winfred Mugge, Arjo Loeve, and Jan Peter van Zandwijk. 2024. “Applicability of the Madymo Pedestrian Model for Forensic Fall Analysis.” *Forensic Science International* 361. doi: 10.1016/J.FORSCIINT.2024.112068.

[13] Xhimitiku, Iva, Giulia Pascoletti, Elisabetta M. Zanetti, and Gianluca Rossi. 2022. “3D Shape Measurement Techniques for Human Body Reconstruction.” Pp. 1–8 in *ACTA IMEKO*. Vol. 11.

[14] Yang, King H., Jingwen Hu, Nicholas A. White, Albert I. King, Clifford C. Chou, and Priya Prasad. 2006. “Development of Numerical Models for Injury Biomechanics Research: A Review of 50 Years of Publications in the Stapp Car Crash Conference.” *Stapp Car Crash Journal* 50(November). doi: 10.4271/2006-22-0017.

[15] Zhan, Zhenfei, Yan Fu, and Ren Jye Yang. 2011. “Enhanced Error Assessment of Response Time Histories (EEARTH) Metric and Calibration Process.” *SAE 2011 World Congress and Exhibition*. doi: 10.4271/2011-01-0245.

Ride Comfort Optimization through Multibody Modelling of Human-Vehicle Interaction

Raj Desai

Centre for Future Transport and Cities, Coventry University, UK

ABSTRACT

Assessing ride comfort is important for designing vehicles to provide a comfortable experience for passengers. Current methods often use complex computer Finite Element (FE) human body models. While these models are accurate, they are too slow and complex to be used in real-time situations. This paper presents a simpler model to assess ride comfort within an excitation range of up to 20 Hz, designed to simulate efficiently enough for real-time use without compromising accuracy in measuring comfort. By simplifying the model and using multibody dynamics approach, allow faster calculations while accurately simulating the body's response to vehicle vibrations and movements. The model is validated to predict experimental data through parameter identification using genetic algorithm optimization method. This model accurately captures the direct and cross axis vibrational response making it a practical tool for real-time applications in vehicle design. This work aims to support the development of efficient, user- friendly tools for studying human body responses under various driving conditions, enabling the creation of more comfortable vehicles and advancing resilient comfort solutions in the automotive industry.

Keywords: Human body modelling, ride comfort, vibrations

INTRODUCTION

Optimizing ride comfort is essential in vehicle engineering, as it directly influences the ergonomic efficiency, fatigue reduction, musculoskeletal strain, and long-term physical health of passengers (Mohajer et al., 2020). With the rapid advancement of automotive technologies, there is an increasing focus on optimizing vehicle comfort by understanding and mitigating the impact of vehicle vibrations, comfortable seat design, road irregularities, and other dynamic forces on the human body. Traditionally, assessing ride comfort involves the use of detailed computational models of the human body, built using the Finite Element Method (FEM) (Iwamoto et al., 2002). These models are highly accurate in capturing the complex biomechanics of the human body, seat-to-human contact pressure distribution, and offer insights into how different vehicle motions impact passenger comfort. However, they are primarily developed for assessing occupant injury in short duration crash scenarios, limiting their effectiveness for comfort-focused analysis. While FEM models are accurate and include details like organs, muscles, they are very complex and require a lot of computing power. This makes them impractical for real-time assessments during long journey or iterative design assessments during the vehicle design process. To achieve quick and approximate results, fast models are essential. These models enable rapid design iterations across various levels, including seat-human interaction, suspension parameters fine tuning, and road-tire interaction dynamics, enabling effective optimization throughout the process.

In automated vehicles, human body modelling plays a crucial role in enhancing both ride comfort and safety. As vehicles become increasingly autonomous, passengers may engage in various activities such as reading, working, or relaxing in reclined seating postures, which introduces new comfort and safety considerations (Fahse et al., 2023). Human body models for automated vehicles need to account for different body positions and interactions with the vehicle, as well as diverse responses to acceleration, braking, and cornering. Simplified, real-time capable models tailored for autonomous driving conditions can help designers predict and enhance comfort by simulating how diverse postures and interactions respond to vehicle motions. These models support the comfort systems those will be adjusted in real- time, ensuring a smooth and safer experience for occupants. This simplified approach is particularly suitable for real-time adaptive comfort systems, essential for autonomous vehicles where passengers will adapt different body postures and non-driving related activities.

The need for a more efficient, real-time capable solution has led to growing interest in developing simplified human body models that can provide accurate ride comfort assessments while minimizing computational load (Elbanhawi et al., 2015). A simplified model would enable automotive designers to evaluate ride comfort during early stages of design, allowing for faster, data-driven decision-making without the delays associated with more complex simulations. Additionally, such a model could potentially be integrated into active suspension and dynamic response systems within the vehicle, enabling real-time monitoring and automatic adjustments to enhance comfort as driving conditions change. This would mark a significant step forward in creating adaptive, human-cantered comfort systems in modern vehicles.

This paper introduces a simplified approach to human body modelling for ride comfort assessment, designed specifically to be simplified efficient models for real-time applications. By reducing the complexity of FEM-based models, the proposed model maintains accuracy in capturing seat to head vibration transmissibility while allowing for much faster computation. The simplified model has been validated through experimental data, demonstrating its effectiveness in predicting comfort levels under various driving conditions and its suitability for integration into real-time systems. This research provides a vital tool for automotive designers, engineers, and manufacturers, facilitating the creation of accessible, adaptive, and efficient vehicle comfort solutions. It supports the automotive industry's shift toward more human- centered and responsive vehicle designs, meeting the growing demand for a smoother and more comfortable ride experience.

MATERIALS & METHODS

A 12 degrees of freedom (DoF) multibody biomechanical seated human body model, joint configuration, lumbar cushion support is shown in Fig. 1. The model made up of four rigid masses constituting the anthropometry of thigh, lower-upper torso, pelvis and head, individually. To simplify, the legs and hands are not included. Each joint Ji (3-DoF) comprises of rotational and translational spring-damper that allows relative motion between different body parts. The equations of motion were developed using

free-body diagram analysis and the Newton's method. The time-domain equations are then converted to the frequency domain using Laplace transformation. The perpendicular compression (kv1-kv3 and cv1-cv3) and parallel shear (kh1-kh3 and ch1-ch3) properties of the human body at the contact points (c1, c2, c3) are represented by spring-dampers to the seat surface. The spring-dampers in contact with lumbar contact at c3 inclined at an angle (α) depict the angle of inclination of the backrest. The construction is designed to enable the coupling of fore-aft and vertical motions through the inclination of the backrest. The weight and size of different body parts are taken from literature, while joint properties are adjusted to match the model's response closely with experimental results.

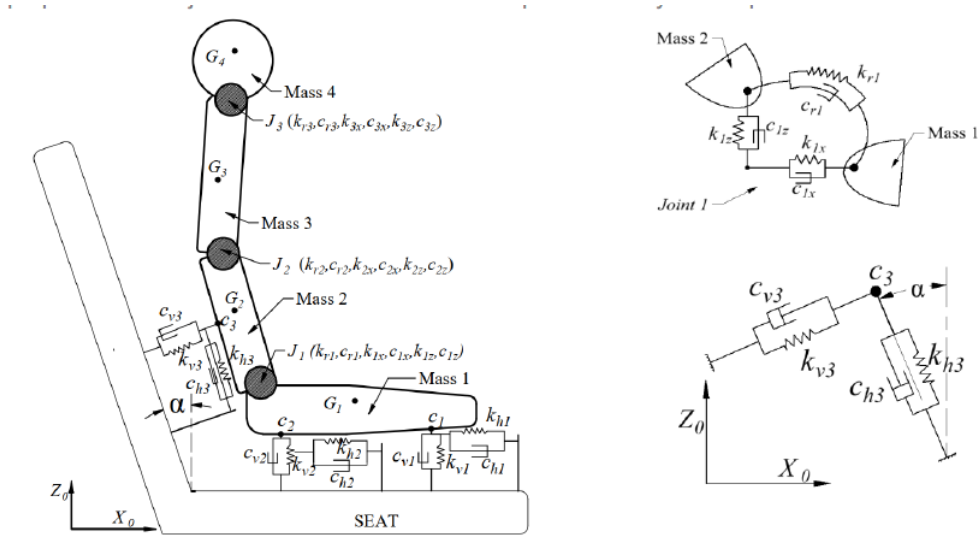

Figure 1: 12 DoF human body model with joint configuration and lumbar support.

The model is integrated with vehicle model to investigate the ride comfort Fig 2 to investigate and optimize ride comfort (Desai et al., 2020).

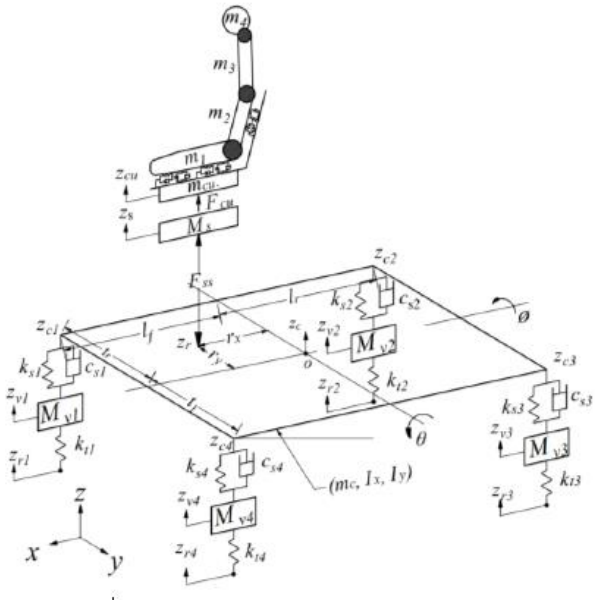

Figure 2: Vehicle cushion human model.

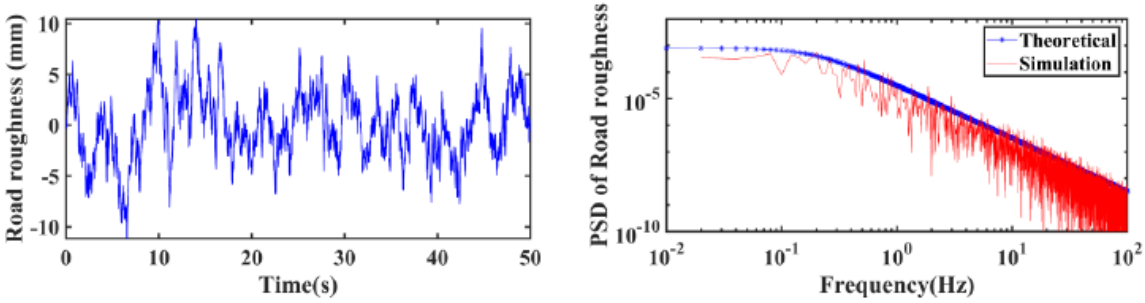

Figure 3 Random Road (grade C, velocity=20 m/s): (a) random constant velocity road profile and (b) PSD of road roughness.

To verify the simulation results, the theoretical power spectral density (PSD) of road roughness is calculated in the frequency domain to serve as a benchmark for comparison. This theoretical PSD provides an expected profile of road irregularities, allowing an assessment of how accurately the simulation reflects real-world conditions. When comparing the PSD values from both the simulation and theoretical calculations, shows a similar trend, indicating that the model accurately captures the frequency characteristics of road roughness. This similarity, as shown in Fig. 3, complement the validity of the simulation approach and its applicability to realistic scenarios.

RESULTS AND DISCUSSION

Genetic algorithm-based optimization techniques were employed to ensure the model's accuracy. This approach provided validation by comparing the model with experimental data (Wang et al., 2006), with emphasis on accurately capturing direct and cross-axis seat-to-head transmissibility. This validation process confirmed that the model's predictions closely match the experimental data, as shown in Fig. 4.

The model effectively captures both direct and cross-axis vibrational responses, allowing for a realistic evaluation of comfort across various driving conditions. Fig 5 shows how different factors changes with road roughness and vehicle speed. The top-left chart represents the force between the seat cushion and the passenger, which indicates the pressure on the body. The top-right chart shows the head's fore- aft (back-and-forth) acceleration, which affects comfort during turns or bumps. The bottom-left chart shows the head's up-and-down acceleration, reflecting how road vibrations impact the head. The bottom-right chart shows the vertical acceleration of the seat, adjusted for human sensitivity to different vibration frequencies. As road roughness and speed increase, these forces and movements generally rise, highlighting conditions that affect passenger comfort. As vehicle speed and road roughness increase the model predicts a rise in seat-to-head transmissibility, indicating a decrease in passenger comfort. This trend shows that the model can reliably simulate discomfort under challenging road conditions, offering valuable insights for improving suspension and seating systems.

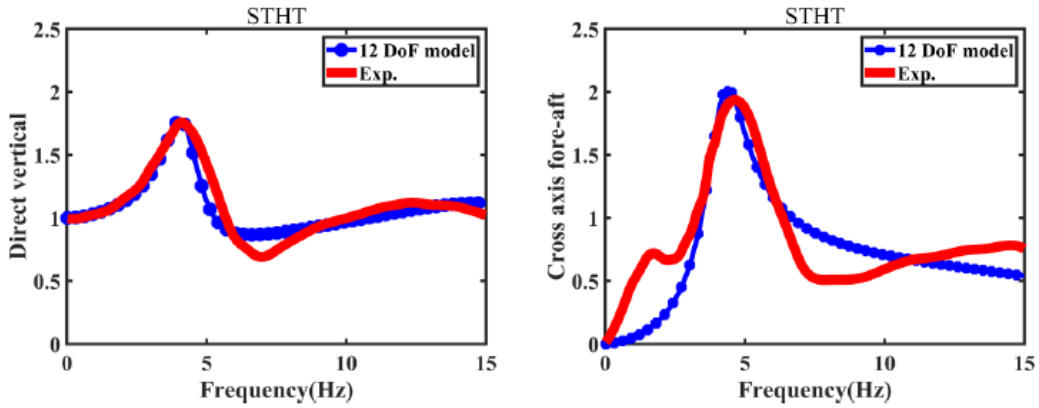

Figure 4: Experimental vs presented analytical body model seated with inclined backrest

Furthermore, by capturing cross-axis vibrations often overlooked in simpler one-dimensional lumped models the model better represents real-world dynamics. Cross-axis vibrations are crucial for assessing passenger comfort, as they greatly impact discomfort during cornering or on uneven surfaces. This capability indicates potential for adapting the model to active suspension systems that can adjust dynamically to changing road conditions in real-time.

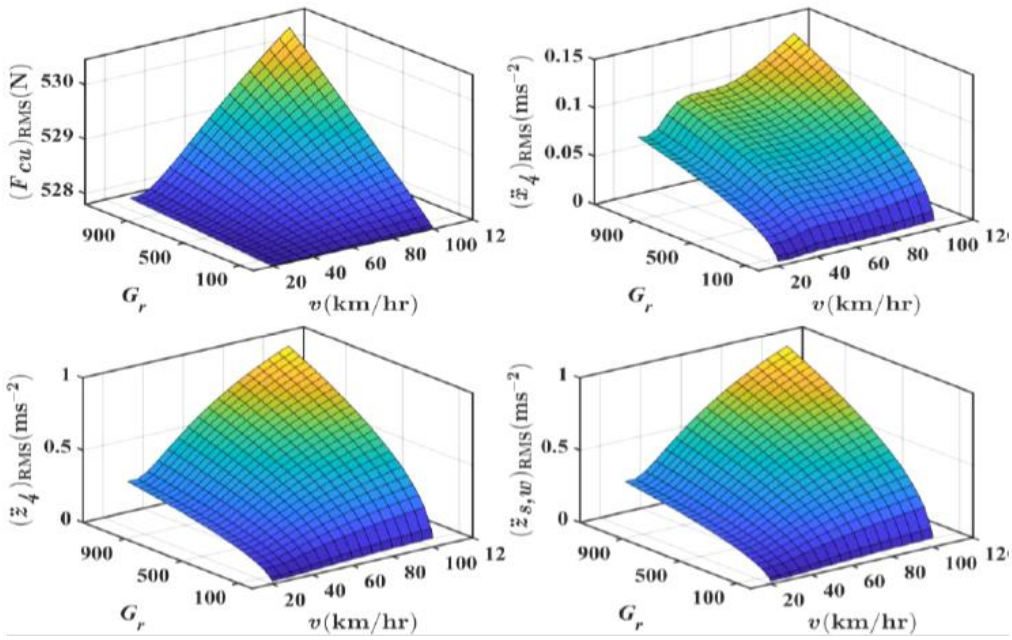

Figure 5: 3D variation due to road roughness and vehicle speed

CONCLUSIONS

This study introduces a simplified human body model for real-time ride comfort assessment, enabling faster computation compared to traditional FEM models that, which are more accurate, are too complex for real-time applications. The proposed model provides a faster, efficient alternative that retains essential accuracy in capturing the vibrational response of the human body, particularly from seat to head, across both direct and cross-axis responses. By reducing computational requirements, this model allows for fast design iterations, making it a valuable tool for automotive designers focused on enhancing passenger comfort.

The model's real-time capabilities make it ideal for both conventional vehicles and emerging automated systems, where adaptive comfort solutions are increasingly important. With future integration of a motion sickness component, this model could predict discomfort levels and further enhance comfort systems. Validated against experimental data, it demonstrates reliability across various vibration frequencies, confirming its suitability for integration into different vehicle systems.

In summary, this work provides an effective and practical tool for the automotive industry, bridging the gap between complex human body modelling and real-time comfort evaluation. By enabling more adaptive, human-cantered vehicle designs, this model supports the industry's commitment to delivering a smoother, more comfortable, and responsive passenger experience.

REFERENCES

[1] Desai, R., Guha, A., & Seshu, P. (2020). Modelling and simulation of an integrated human-vehicle system with non-linear cushion contact force. *Simulation Modelling Practice and Theory*, 102206.

[2] Elbanhawi, M., Simic, M., & Jazar, R. (2015). In the Passenger Seat: Investigating Ride Comfort Measures in Autonomous Cars. *IEEE Intelligent Transportation Systems Magazine*, *7*(3), 4–17.

[3] https://doi.org/10.1109/MITS.2015.2405571

[4] Fahse, N., Millard, M., Kempter, F., Maier, S., Roller, M., & Fehr, J. (2023). Dynamic human body

[5] models in vehicle safety: An overview. *GAMM-Mitteilungen*, *46*(2), e202300007.

[6] Iwamoto, M., Kisanuki, Y., Watanabe, I., Furusu, K., Miki, K., & Hasegawa, J. (2002). Development of a finite element model of the total human model for safety (THUMS) and application to injury

[7] reconstruction. *Proceedings of the International IRCOBI Conference*, 18–20.

[8] Mohajer, N., Nahavandi, S., Abdi, H., & Najdovski, Z. (2020). Enhancing passenger comfort in autonomous vehicles through vehicle handling analysis and optimization. *IEEE Intelligent*

[9] *Transportation Systems Magazine*, *13*(3), 156–173.

[10] Wang, W., Rakheja, S., & Boileau, P.-É. (2006). Effect of back support condition on seat to head transmissibilities of seated occupants under vertical vibration. *Journal of Low Frequency Noise,*

[11] *Vibration and Active Control*, *25*(4), 239–259.

Three-dimensional simulation of fracture healing with two different fracture-fixation devices

George T. Morgan[1], Arul Ramasamy[1,2,3], Spyros D. Masouros[1]

1 Imperial College London, Department of Bioengineering, London, SW7 2AZ; 2 Royal Centre for Defence Medicine, ICT Centre, Academic Department of Military Trauma and Orthopaedics, Birmingham, B15 2SQ; 3 Milton Keynes Hospital NHS Foundation Trust, Trauma and Orthopaedics, Milton Keynes, MK6 5LD

ABSTRACT

Traditional methods of comparing bone-fracture treatments have failed to identify the best option for certain fracture types. This study uses a previously validated computational tool to model the healing process in a femoral shaft fracture. The two most common fixation devices, intramedullary nail and lateral locking plate, were modelled. The computational tool predicted accurately axisymmetric callus development in the intramedullary nail model and asymmetric callus development in the locking plate model. These findings demonstrate the tool's suitability for a large-scale *in silico* trial of femoral fracture fixation.

Keywords: fracture-healing algorithm; fixation device; in silico trial; callus; finite element

INTRODUCTION

Distal femoral fractures represent 3-6% of femoral fractures (Court-Brown and Caesar, 2006; Martinet et al., 2000) with an annual occurrence of 4.5 per 100,000 (Court-Brown and Caesar, 2006). While these fractures are ten times less frequent than proximal femoral fractures (Martinet et al., 2000), they have similar morbidity and mortality rates. Proximal femoral fractures have received much attention with the National Hip Fracture Database and NHS Best Practices Tariff, leading to decreased morbidity and mortality rates (Smith et al., 2015). There is no consensus on the management of distal femoral fractures (Smith et al., 2015; Toro, 2015).

Locking plates offer better angular stability than intramedullary nails due to the use of locking screws, which is particularly beneficial in intra-articular fractures. Locking plates have gained popularity and are often the preferred treatment for distal femoral fractures (Ricci et al., 2014; Rodriguez et al., 2014), but early promising results (Kregor et al., 2004; Schütz et al., 2001) may have led to overuse and increased non-union rates (Ricci et al., 2014; Rodriguez et al., 2014). The lateral placement of locking plates, however, creates bending, leading to an asymmetric callus development during healing (Lujan et al., 2010). A review of trials comparing interventions for distal femoral fractures found limited evidence to support locking plates as a standard treatment (Claireaux et al., 2022; Griffin et al., 2015), with many trials using outdated implants (Griffin et al., 2017). Research on locking plates is further complicated by variations in plate configurations (MacLeod et al., 2018; MacLeod and Pankaj, 2018).

A large-scale randomised controlled trial (RCT) comparing locking plates and intramedullary nails for distal femoral fractures was planned, but patient recruitment issues rendered it unfeasible (Griffin et al., 2019). Even with sufficient recruitment, the many parameters involved, such as comminution or articular involvement, make a generalised approach to treatment unlikely. A large-scale *in silico* trial offers a viable alternative by enabling the simulation of a range of well controlled scenarios, and so could offer specific treatment recommendations for each fracture classification.

Modelling distal femoral fractures presents computational challenges, particularly regarding screw placement near the fracture site. Previous studies have shown that screw modelling has a minor impact on global mechanics, but significantly affects local mechanics (MacLeod et al., 2012). Consequently, this study models a mid-shaft femoral fracture to allow certain modelling simplifications. The primary objective is to validate the ability of a novel fracture-healing algorithm to replicate key mechanical differences between locking plates and intramedullary nails, such as the angular stability of locking plates and the

symmetric motion of intramedullary nails, and their effects on fracture healing. Simulating locking plate fixation requires 3-D modelling, increasing computational requirements.

MATERIALS & METHODS

A validated fracture-healing algorithm was used in this study (Morgan et al., 2024). A finite-element (FE) model of the fracture, fixator, and callus region was used to calculate the local mechanical strains at each finite element in the callus region. This strain information was then used by a 'biological controller' to model the various fracture-healing processes. As the outputs of the biological controller include tissue change in the callus region, the material properties of the FE model must be updated to reflect these changes. Thus, as fracture healing progresses, the fracture-healing algorithm was able to capture the progressive ossification of the callus. This iterative process is shown in a flowchart diagram in Figure 1.

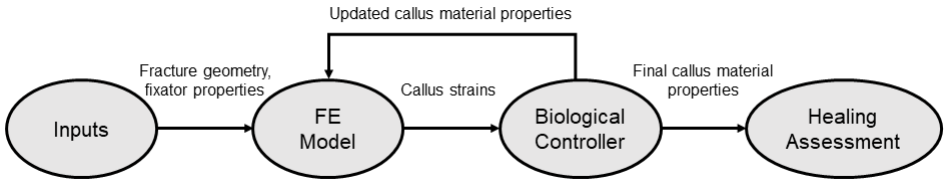

Figure 1: A flowchart diagram of a typical fracture-healing algorithm workflow.

Two 3-D non-linear models were developed in MSC.Marc (v2021, MSC Software) of a femoral shaft fracture; one which was treated with an intramedullary nail, and one which was treated with a lateral locking plate. Femur geometry was taken from the Muscle Standardized Femur Model (Viceconti, 2017), which is based on a bone surrogate for *in vitro* testing. A simple transverse diaphyseal fracture was modelled as an osteotomy (Lewis et al., 2021) which was created at the mid-shaft of the femur by removing a 5 mm section of bone. A callus region was created 56 mm in length and 64 mm in diameter, with no intramedullary portion (Figure 2). The callus volume was created by revolving the 2-D sketch around the long-axis of the bone, then performing a Boolean subtract function on the volume to ensure the callus was flush to the bone sections. Trabecular bone was not included in the model geometry, but its exclusion is unlikely to have affected the mechanical environment at the mid-shaft. The bone segments and callus were meshed with linear tetrahedral elements with average element edge lengths of 3 mm and 1 mm, respectively.

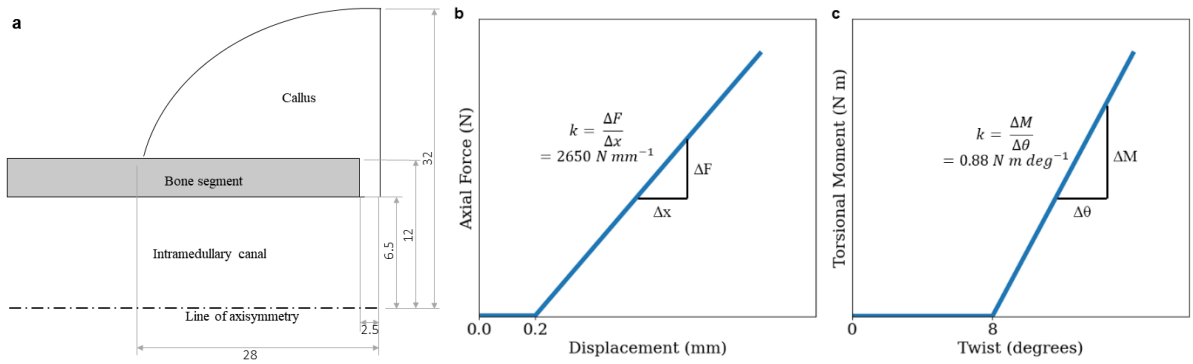

Figure 2: (a) Dimensions of the initial callus domain. Shown is half of an axisymmetric profile of the callus region. The profile is revolved around the long axis of the bone to create the callus volume. An idealised bone segment with approximately the same dimensions of the bone segments is shown shaded. The actual bone segment geometry used is physiological and varies along the length of the bone. (b-c) Non-linear stiffness plots used to represent the intramedullary nail, which include free-movement regions, for (a) axial and (b) torsional stiffness (Dailey et al., 2015; Ren and Dailey, 2020).

The locking plate was modelled with dimensions of 150 mm × 5 mm × 17.5 mm. Eleven holes with an inter-hole spacing of 12.5 mm were created with diameters of 5 mm. Screws were modelled as 4.3 mm diameter

beam elements connecting rigid-body elements (RBE2s) at the plate, near-plate cortex, and far-plate cortex. The plate was located centrally over the mid-point of the callus on the lateral side. The central hole in the plate was located directly over the fracture gap. Screws were placed at the first, third, and fifth screw holes in the plate on both sides of the fracture. 4.3 mm diameter through-holes were created in both cortices of the bone segments at each screw location. Plate and screw volume which overlapped with the callus region was removed from the callus region. The bone-plate offset varied between 2 mm to 5 mm along the length of the plate. The plate was meshed with an element edge length of 1.5 mm, and refined to 0.75 mm in the region of the fracture, where bending stresses are highest. Linear tetrahedral elements were used with a strain-smoothening formulation, which are better suited for capturing bending behaviour than traditional tetrahedral elements (Dohrmann et al., 2000).

The intramedullary nail was modelled as 6 fixed-degree-of-freedom springs connecting the retained nodes of two RBE2s, which were located at a distance of 135 mm on each side of the callus centre, for a total nail length of 270 mm. At each nail end, two through-holes, orthogonal to each other, of diameter 4.3 mm were created in the bone segments, at distances of 130 mm and 135 mm from the callus centre. The interior nodes of each through-hole were tied to their nearest retained node, to attach the intramedullary nail to the bone segments. Axial and torsional stiffnesses were modelled as non-linear, with an initial free-movement range of 0.2 mm and 8°, respectively, followed by a linear stiffness of 2,650 N mm^{-1} and 0.88 N m deg^{-1}, respectively, as shown in Figures 2b and c (Dailey et al., 2015; Ren and Dailey, 2020). Bending stiffness, represented as two rotational degree-of-freedom springs, was 32 N m deg^{-1} (Schandelmaier et al., 2000). The intramedullary nail was modelled with a high shear stiffness of 20,000 N mm^{-1}, represented as two translational degree-of-freedom springs.

All materials were assigned linear elastic material properties. The locking plate and screws were modelled in stainless steel. A summary of material properties is given in Table 1 (Ren and Dailey, 2020).

Table 1: Young's modulus and Poisson's ratio of the materials used in the models. All materials were modelled as linear elastic isotropic.

Material	*Young's modulus (MPa)*	*Poisson's ratio*
Soft tissue	3	0.3
Cartilage	200	0.45
Woven bone	400	0.36
Lamellar bone	10,000	0.36
Stainless steel	200,000	0.3

The hip joint was modelled as an RBE2 with the retained node located at the centre of the femoral head and tied nodes located on the surface of the femoral head. The retained node was fixed in 2 translational degrees-of-freedom, allowing for axial translation. The knee joint was modelled with 2 RBE2s, one for each condyle, with the retained nodes located at the centre of each condyle and tied nodes located on the surface of each respective condyle. The medial condyle was fixed in all 3 translational degrees of freedom, and the lateral condyle was fixed in 2 translational degrees of freedom, allowing for lateral translation (MacLeod, 2015; Nassiri et al., 2013). Loading was applied at the hip as an axial force with a magnitude of 238% of body-weight, or 1,635 N (Bergmann et al., 2001; Heller et al., 2001; MacLeod, 2015). Glued contact was specified between all contacting bodies, whereby no tangential nor direct relative motion was allowed.

Inter-fragmentary movement (IFM) was measured at each iteration at the external surface of both the lateral and medial cortices to capture the bending dynamics of the locking plate model (MacLeod et al., 2012). IFM was also measured at both cortices in the intramedullary nail model to confirm its predominantly axial behaviour.

A biological controller which was previously described for a 2-D model was used (Morgan et al., 2024). The only notable consideration in the 3-D model used here is the number of nodes shared between two callus

elements to define neighbouring elements; the number of nodes to define a neighbour was left unchanged at 1.

At the end of 150 iterations, previously shown to be adequate for the healing process to have completed, the fixator in each of the models was removed and a bending test simulated to assess the bending stiffness of the healed construct. Two new RBE2s were created, one at 100 mm distal and one at 100 mm proximal to the centre of the callus region, with a central retained node and tied nodes along the transverse cross-section of the femur. A bending moment of 5,000 N mm was applied at each of the retained nodes. The distal retained node was fixed in all 3 translational degrees of freedom, and the proximal retained node was fixed in 2 translational degrees of freedom, allowing axial translation. Deflection was measured at the centre of the callus. Bending stiffness was calculated as the applied moment divided by the mid-span deflection. Bending stiffness was measured in both directions across four planes: sagittal, coronal, and the two planes at 45° to the sagittal and coronal planes.

RESULTS AND DISCUSSION

Results

The simulations of the intramedullary nail and plate models both converged at iteration 50. The IFM progressions of each simulation, measured at both the medial and lateral cortices, are shown in Figure 3a The minimal difference between the medial and lateral IFMs in the intramedullary nail model simulation is attributable to the predominantly axial movement in the model, while the large difference between the medial and lateral IFMs in the plate model simulation is attributable to the predominantly bending behaviour of the plate model.

The Young's modulus, bone concentration, cartilage concentration, and intramembranous ossification activation level at each callus finite-element at iterations 7, 14, 21, 35, and 100 are shown for the coronal callus cross-section of the intramedullary nail model in Figure 3b, and for the plate model in Figure 3c. The intramedullary nail simulation shows axisymmetric callus development, with periosteal bulging, external callus bridging, and subsequent bridging at the cortices. In the coronal plane of the plate simulation, there is greater callus development at the medial, or 'far-plate', cortex than at the lateral, or 'near-plate', cortex. Bony bridging occurs at the lateral cortex before the medial cortex.

The bending stiffnesses of the final iteration of the simulations of the two models, with fixators removed, in 8 different bending directions, along with the average and standard deviations of these directions, are shown in Table 2. The average bending stiffness of the intramedullary nail model is higher than that of the plate model. Within each model, bending stiffnesses are approximately equivalent in either direction of a given plane; for example, the bending stiffness of the nail model in the anterior-posterior plane is the same with bending in the anterior direction as in the posterior direction.

Table 2: Bending stiffnesses in 8 bending planes of the healed calluses of the model treated with an intramedullary nail and with a plate. 'IM' = intramedullary. Bending planes are coded by a two-letter plane followed by the direction of callus movement, ie: 'AP-A' = anterior-posterior (or sagittal) plane, with callus moving anteriorly. 'ML-M' = medial-lateral (or coronal) plane, with callus moving medially.

Bending plane	*Bending stiffness (N m mm^{-1})*	
	Intramedullary nail	*Plate*
AP-A	23.5	22.8
AP-A + ML-M	25.3	23.9
ML-M	23.7	21.6
AP-P + ML-M	22.0	20.7
AP-P	23.5	22.8

AP-P + ML-L	25.3	23.9
ML-L	23.7	21.6
AP-A + ML-L	22.0	20.7
Average ± Standard deviation	23.6 ± 1.2	22.2 ± 1.2

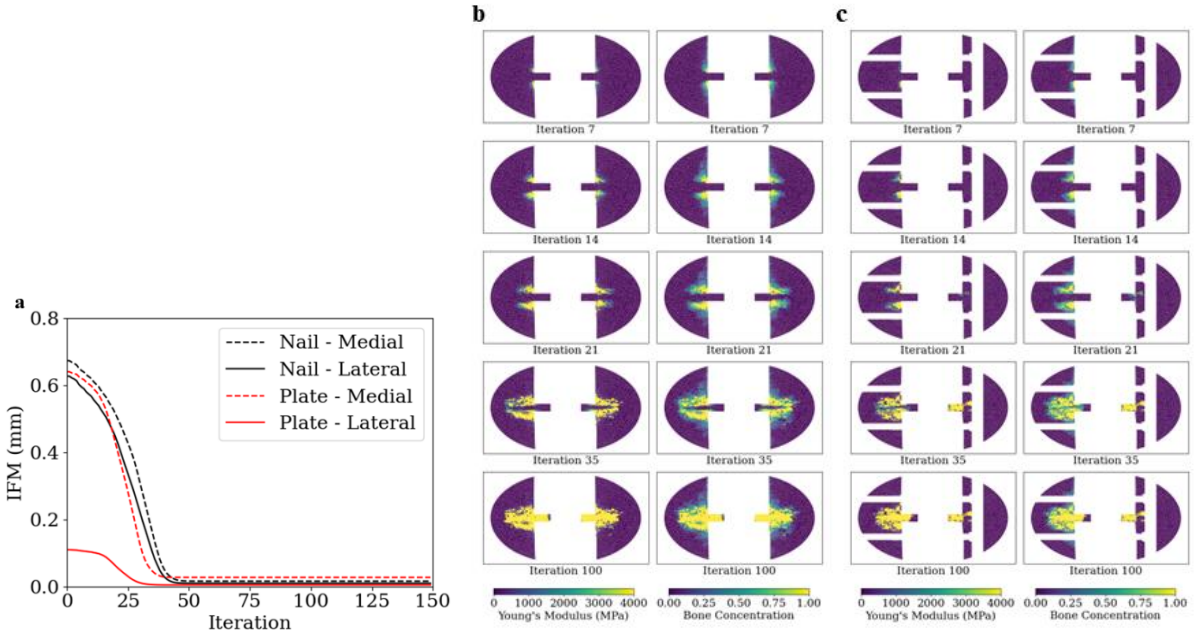

Figure 3: (a) Temporal evolution of IFM in the intramedullary nail and plate model simulations, with IFM measured at both the lateral and medial cortices, representing the near and far-plate cortices in the plate model. (b-c) Coronal view of the callus cross-section of the (b) intramedullary nail model and (c) plate model simulations at iterations 7, 14, 21, 35, and 100. Note the plate and two screws are visible in the outline of the callus. The plotted variables for each callus finite element are Young's modulus and bone concentration. Bone is depicted as tissue proportion within the finite element, with a bone concentration of 1.0 indicating full ossification.

DISCUSSION

The simulation of the intramedullary nail model showed symmetric IFM throughout healing, with medial and lateral IFMs closely matching (Figure 3a), leading to mostly axisymmetric callus development (Figure 3b). In contrast, the locking plate model had an asymmetric IFM, with the medial IFM greater than the lateral IFM (Figure 3a). The lateral IFM converged before the medial IFM, highlighting the need to measure IFMs at multiple cortex locations in 3-D models, and the inadequacy of IFM as a sole indicator of fracture healing. The locking plate model had asymmetric callus formation in the coronal plane, with more callus at the medial cortex, consistent with physiological observations in plate-treated fractures (Lujan et al., 2010).

The fracture-healing algorithm previously demonstrated a physiological healing sequence in 2-D models, and has also predicted here physiological healing in 3-D models for both fixation methods. The simulations began with periosteal bulging via intramembranous ossification, followed by cartilaginous and bony bridging at the external callus (Vetter et al., 2010). In the locking plate model, the near-plate cortex bridged first due to lower strains, though whether this is physiological remains unclear due to limited time-series radiographs and optical obstruction by the plate (Lujan et al., 2010). This phenomenon warrants experimental investigation, as it could impact healing dynamics and inform late-stage rehabilitation.

The bending stiffness assessments of both models were approximately equal, and with similar patterns across bending planes, despite the asymmetric mechanics of the plate model; for example, both models

had the highest bending stiffness in the 'AP-A + ML-M' and 'AP-P + ML-L' directions. The intramedullary nail model had slightly higher average callus bending stiffness, aligning with clinical best practices (Gwathmey et al., 2010). The plate model showed relatively faster healing based on medial IFM traces, but should be considered along with the fact that IFM is a poor measure of healing. An analysis of the bending stiffness at each iteration could yield insights into the relative healing speeds of the treatments, but would significantly increase computational expense.

Previous *in silico* studies of femoral fractures have used a gap width of 6 mm (MacLeod, 2015), but a 5 mm gap width was used in this study to reduce computational expense. This likely had little effect on the results of the study, as successful healing was achieved in both cases and a reduction in gap width generally improves healing outcomes. The use of a larger gap width may amplify the differences in callus development; a larger gap may increase the effect of plate bending, creating greater differences in strain magnitudes at the far-plate cortex. This may lead to the fracture-healing algorithm predicting a non-union in the plate model and a successful union in the intramedullary nail model.

A previous study which expanded a fracture-healing algorithm to a 3-D model noted an over-sensitivity to distortional strain, predicting non-unions where experimental data showed only a delayed union (Ren and Dailey, 2020). In this study, no significant difference in overall outcome was observed between the predictions for axisymmetric models and 3-D models, however, torsional loading was not applied. While physiological hip-joint loading is predominantly axial (Bergmann et al., 2001; Heller et al., 2001), some torsional loading occurs. Applying joint loads derived from musculoskeletal modelling of rehabilitation could provide better insights into algorithm performance under real loading (Orth et al., 2023).

A mid-shaft femoral fracture was modelled in this study to manage computational expense. Modelling a distal femoral fracture would likely require physical modelling of screws and contact interactions with bone fragments and the plate, given their proximity to the fracture gap (MacLeod et al., 2012). The mid-shaft model allowed for simplifications, including abstraction of the intramedullary nail as fixed-degree-of-freedom springs. A further simplification was the use of joint reaction force without muscle forces; muscle forces and the use of free boundary conditions have been shown to affect bone strains in FE models of the femur (Phillips, 2009; Viceconti, 2017), but whether increasing modelling complexity would alter callus region strains in a femoral fracture model is unclear. A limitation of the models used in the present study is the lack of *in vitro* validation testing, however, the use of physiological boundary conditions, including joint restraints, is challenging to model *in vitro*.

CONCLUSIONS

A validated fracture-healing algorithm was applied to two 3-D models of femoral mid-diaphyseal fractures; one treated with an intramedullary nail, and one treated with a locking plate. While the fracture-healing algorithm had previously only been applied to axisymmetric models, the algorithm predicted successfully a physiological healing sequence in the 3-D models. The effects of different fixator types on callus development were captured accurately; specifically, the algorithm predicted the asymmetric callus development caused by the bending motion in the locking plate model, and the symmetric callus development in the intramedullary nail model.

REFERENCES

[1] Bergmann, G., Deuretzbacher, G., Heller, M., Graichen, F., Rohlmann, A., Strauss, J., and Duda, G.N. 2001. "Hip Contact Forces and Gait Patterns from Routine Activities." Journal of Biomechanics 34:859–871.

[2] Claireaux, H.A., Searle, H.K., Parsons, N.R., and Griffin, X.L. 2022. "Interventions for Treating Fractures of the Distal Femur in Adults." Cochrane Database of Systematic Reviews.

[3] Court-Brown, C.M., and Caesar, B. 2006. "Epidemiology of Adult Fractures: A Review." Injury 37:691–697.

[4] Dailey, H.L., Daly, C.J., and Glass-Hardenbergh, A. 2015. "Mechanical Origins of Fracture Nonunion: Implant Tests and Finite Element Models of Callus Strains." Presented at the Biomedical Engineering Society Annual Meeting.

[5] Dohrmann, C.R., Heinstein, M.W., Jung, J., Key, S.W., and Witkowski, W.R. 2000. “Node-Based Uniform Strain Elements for Three-Node Triangular and Four-Node Elements.” International Journal for Numerical Methods in Engineering 47:1549–1568.

[6] Griffin, X.L., Costa, M.L., Achten, J., Dritsaki, M., Baird, J., and Parsons, N. 2017. “Trial of Acute Femoral Fracture Fixation (TrAFFix): Study Protocol for a Randomised Controlled Feasibility Trial.” Trials 18:538.

[7] Griffin, X.L., Costa, M.L., Phelps, E., Parsons, N., Dritsaki, M., Png, M.E., Achten, J., Tutton, E., Lerner, R., McGibbon, A., and Baird, J. 2019. “Retrograde Intramedullary Nail Fixation Compared with Fixed-Angle Plate Fixation for Fracture of the Distal Femur: The TrAFFix Feasibility RCT.” Health Technology Assessment 23:1–132.

[8] Griffin, X.L., Parsons, N., Zbaeda, M.M., and McArthur, J. 2015. “Interventions for Treating Fractures of the Distal Femur in Adults.” Cochrane Database of Systematic Reviews.

[9] Gwathmey, W.F., Jones-Quaidoo, S.M., Kahler, D., Hurwitz, S., and Cui, Q. 2010. “Distal Femoral Fractures: Current Concepts.” American Academy of Orthopaedic Surgeons 18:597–607.

[10] Heller, M.O., Bergmann, G., Deuretzbacher, G., Dürselen, L., Pohl, M., Claes, L., Haas, N.P., and Duda, G.N. 2001. “Musculoskeletal Loading Conditions at the Hip during Walking and Stair Climbing.” Journal of Biomechanics 34:883–893.

[11] Kregor, P.J., Stannard, J.A., Zlowodzki, M., and Cole, P.A. 2004. “Treatment of Distal Femur Fractures Using the Less Invasive Stabilization System: Surgical Experience and Early Clinical Results in 103 Fractures.” Journal of Orthopaedic Trauma 18:509–520.

[12] Lewis, G.S., Mischler, D., Wee, H., Reid, J.S., and Varga, P. 2021. “Finite Element Analysis of Fracture Fixation.” Current Osteoporosis Reports 19:403–416.

[13] Lujan, T.J., Henderson, C.E., Madey, S.M., Fitzpatrick, D.C., Marsh, J.L., and Bottlang, M. 2010. “Locked Plating of Distal Femur Fractures Leads to Inconsistent and Asymmetric Callus Formation.” Journal of Orthopaedic Trauma 24.

[14] MacLeod, A., Simpson, A.H.R.W., and Pankaj, P. 2018. “Experimental and Numerical Investigation into the Influence of Loading Conditions in Biomechanical Testing of Locking Plate Fracture Fixation Devices.” Bone and Joint Research 7:111–120.

[15] MacLeod, A.R. 2015. “Modelling and Optimising the Mechanical Behaviour of Fractures Treated with Locking Plates.” University of Edinburgh.

[16] MacLeod, A.R., Pankaj, P., and Simpson, A.H.R.W. 2012. “Does Screw-Bone Interface Modelling Matter in Finite Element Analyses?” Journal of Biomechanics 45:1712–1716.

[17] Martinet, O., Cordey, J., Harder, Y., Maier, A., Bühler, M., and Barraud, G.E. 2000. “The Epidemiology of Fractures of the Distal Femur.” Injury 31:62–94.

[18] Morgan, G.T., Low, L., Ramasamy, A., and Masouros, S.D. 2024. “A Novel Strain-Based Bone-Fracture Healing Algorithm Able to Predict a Range of Healing Outcomes.” Frontiers in Bioengineering and Biotechnology 12:1477405.

[19] Nassiri, M., Macdonald, B., and O’Byrne, J.M. 2013. “Computational Modelling of Long Bone Fractures Fixed with Locking Plates - How Can the Risk of Implant Failure Be Reduced?” Journal of Orthopaedics 10:29–37.

[20] Orth, M., Ganse, B., Andres, A., Wickert, K., Warmerdam, E., Müller, M., Diebels, S., Roland, M., and Pohlemann, T. 2023. “Simulation-Based Prediction of Bone Healing and Treatment Recommendations for Lower Leg Fractures: Effects of Motion, Weight-Bearing and Fibular Mechanics.” Frontiers in Bioengineering and Biotechnology 11:1067845.

[21] Phillips, A.T.M. 2009. “The Femur as a Musculoskeletal Construct: A Free Boundary Condition Modelling Approach.” Medical Engineering and Physics 31:673–680.

[22] Ren, T., and Dailey, H.L. 2020. “Mechanoregulation Modeling of Bone Healing in Realistic Fracture Geometries.” Biomechanics and Modeling in Mechanobiology 19:2307–2322.

[23] Ricci, W.M., Streubel, P.N., Morshed, S., Collinge, C.A., Nork, S.E., and Gardner, M.J. 2014. “Risk Factors for Failure of Locked Plate Fixation of Distal Femur Fractures: An Analysis of 335 Cases.” Journal of Orthopaedic Trauma 28:83–89.

[24] Rodriguez, E.K., Boulton, C., Weaver, M.J., Herder, L.M., Morgan, J.H., Chacko, A.T., Appleton, P.T., Zurakowski, D., and Vrahas, M.S. 2014. “Predictive Factors of Distal Femoral Fracture Nonunion after Lateral Locked Plating: A Retrospective Multicenter Case-Control Study of 283 Fractures.” Injury 45:554–559.

[25] Schandelmaier, P., Farouk, O., Krettek, C., Reimers, N., Mannß, J., and Tscherne, H. 2000. “Biomechanics of Femoral Interlocking Nails.” Injury 31:437–443.

[26] Schütz, M., Müller, M., Krettek, C., Höntzsch, D., Regazzoni, P., Ganz, R., and Haas, N. 2001. “Minimally Invasive Fracture Stabilization of Distal Femoral Fractures with the LISS: A Prospective Multicenter Study Results of a Clinical Study with Special Emphasis on Difficult Cases.” Injury 32:48–54.

[27] Smith, J.R.A., Halliday, R., Aquilina, A.L., Morrison, R.J.M., Yip, G.C.K., McArthur, J., Hull, P., Gray, A., and Kelly, M.B. 2015. “Distal Femoral Fractures.” Injury 46:1084–1088.

[28] Toro, G. 2015. “Locking Plate Fixation of Distal Femoral Fractures is a Challenging Technique: A Retrospective Review.” Clinical Cases in Mineral and Bone Metabolism.

[29] Vetter, A., Epari, D.R., Seidel, R., Schell, H., Fratzl, P., Duda, G.N., and Weinkamer, R. 2010. “Temporal Tissue Patterns in Bone Healing of Sheep.” Journal of Orthopaedic Research 28:1440–1447.

[30] Viceconti, M. 2017. “The ‘Muscle Standardised Femur’ Model.”

Vibration Reductions in the use of Brush Cutter

Massimo Cavacece[1]

[1] *University of Cassino and Southern Latium,*

Department of Civil and Mechanical Engineering,

Via G. Di Biasio 43, 03043 Cassino (FR), Italy

cavacece@unicas.it

ABSTRACT

This research explores the reduction of vibrations originating from an instrument held and operated by a worker. The components that generate vibrations include the drive shaft, cutting attachment, and motor. Increasing the thickness of the shaft tube in the area where the crankshaft bearing is mounted, along with ergonomic handle designs, can reduce mechanical vibrations by 20%-30%. Additionally, steering wheel handles made from specialized materials can provide anti-vibration properties through elastomers. The effects of vibration attenuation are noticeable from the fingers to the elbow, as well as throughout the elbow and back of the worker. The brush cutter features a primary and a secondary system. The primary system comprises the shaft and the rotating head, which is responsible for cutting grass. The secondary system includes the endothermic motor and the handle brush cutter. The vibration control of mechanical equipment allows for an increase in speed and in-action forces during work phases. The dynamic vibration absorber (DVA) is the tuned mass damper (TMD) vibration control device. The device uses an additional system with different shapes or parameters to suppress or reduce the vibration of the primary system. The primary system is considered a mass-spring-damping system for the classical DVA. Similarly, the secondary system consists of a mass-spring-damping system. The vibration control of these structures, primary and secondary systems, examines the dynamic behavior of the entire system. Low-frequency vibrations can be effectively isolated by reducing the system's natural frequency. However, the mechanical system dimensioning optimization identifies optimal values for additional masses, springs, and dampers to reduce mechanical vibrations in the selected frequency range. The proposed anti-vibration system, by spring and damping elements, presents a multifunction handle that is adjustable two-handed. The optimal design of the anti-vibration system focuses on minimizing the frequency response of the secondary system within the range of 0 to 160 Hz.

Keywords: Vibration reductions, human hand-arm system, musculoskeletal disorders

INTRODUCTION

Back pain may depend on the mechanical vibrations the tools produce during the worker's manual processing. Prolonged and excessive mechanical vibrations represent loads applied to the whole body (WBV) and hand-arm system (HAV). Long workloads can lead to health problems.

The damage caused to the man is pain in the hands, lower arm, back pain, and difficulties with lumbar disc herniation. Mechanical shocks on the whole body and hand-arm system characterize the activities of manual workers. Low back pain risk factors are posture and stress induced by electro-mechanical tools. In their daily work, a worker with manual skills can use one or more devices that can produce mechanical vibrations, such as the following portable power tools: brush cutter, chainsaw, and electric saw.

A brush cutter's mechanical vibration emissions can generate a professional risk of mechanical vibration injury, which stresses the human body. Frequent exposure to whole-body vibration and hand-arm systems can deteriorate human body capabilities even with permanent effects. The spine is the central structural element that supports the upper part of the body and protects against spinal disorders that could generate neurological consequences.

Spinal disorders may be the result of vibration exposure combined with other factors. Working posture, anthropometric characteristics, physical workload, noise, and individual susceptibility (age, pre-existing disorders) can produce disorders in the human spine.

The intervertebral discs support high compressive loads and shear deformations, allowing flexibility and rotation. The intervertebral disc may be subject to ruptures and degenerative processes. Mechanical stresses applied to the disc can accelerate the development of degenerative changes.

The balance of rotating components and the reduction of mechanical vibrations are critical factors in minimizing vibration levels. Effective technical solutions include:

1. Coating tool handles with rubber insulators.
2. Isolating the movement between different parts of the tools.
3. Limiting maximum daily exposure time to vibrations.

This research aims to study the transmissibility of vibrations of an instrument held and guided by hand by a worker. The research analyzes the vibration risks associated with using brush cutters to evaluate the effects of mechanical vibrations on the hand-arm system and the whole body. The study estimates the reduction of vibrations in the hand-arm system. Vibration absorbers are devices that, added to a system, can reduce the amplitude of vibrations by introducing equal and opposite dynamic forces and a damping system to dissipate mechanical energy. Effective vibration control of mechanical equipment allows for increased speed and enhanced operational forces during work phases. The primary devices utilized for this purpose are dynamic vibration absorbers (DVAs) and tuned mass dampers (TMDs). These devices employ an auxiliary system with varying shapes or parameters to suppress or mitigate the vibrations of the primary system. The primary system is typically modeled as a mass-spring-damping system, while the secondary system also consists of a mass-spring-damping configuration. Analyzing vibration control in these structures involves examining the dynamic behavior of the combined primary and secondary systems. The lowering of the system's natural frequency can reduce low-frequency vibrations. Additionally, optimizing the dimensions of the mechanical system helps identify the ideal values for additional masses, springs, and dampers, thereby reducing mechanical vibrations within the targeted frequency range.

MATERIALS & METHODS

The brush cutter (Figure 1) presents primary and secondary systems (Figure 2). The primary system consists of the shaft and the rotating head, which makes the cutting of the grass. The secondary system includes the endothermic motor and the handle brush cutter. The decoupling of the primary and secondary systems achieves vibration reduction. A rigid shaft drives the cutting head to transmit engine power to the cutting attachment indirectly through the angle gear. A brush cutter can be used by a worker several times a year. A brush cutter is a portable work machine with a cutting attachment mounted on a shaft over 1 m long. The brush cutter can cut wood and grass. Attachment types can be circular blades or nylon thread. Vibration changes depending on the state of operation of the motor, the type of cutting head, and the posture.

The anti-vibration system's structure effectively isolates the device handles from the drive unit to minimize mechanical vibrations and isolates the motor from the decoupling frame (Figure 3). The vibration-damping systems, comprising elastic and damping elements, adhere to safety and health standards to mitigate the impact of mechanical vibrations on individuals in the workplace. These systems effectively absorb and dissipate the mechanical energy associated with mechanical vibrations. Constructed from steel, rubber, or a combination of both, the anti-vibration systems are meticulously balanced and harmonize with the drive components and tool handles.

The anti-vibration system has a multifunction handle, is two-handed (adjustable without using tools), has an engine with a petrol mixture, and has a universal shoulder strap for cutting thick grass.

Fig.1: Brush cutter with vibration absorber system

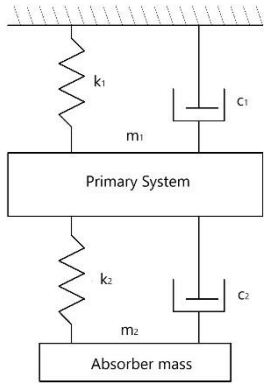

Fig.2: The primary and secondary system of brush-cutter

Fig.3: The anti-vibration system

- *Design Considerations*. In the design of springs subjected to rapid reciprocating motion, it is crucial to minimize the possibility of resonance between the frequency of the spring's alternating motion and one of its natural frequencies of vibration. Typically, the lowest natural frequency is of the most tremendous significance. For a spring compressed between parallel plates, the first mode of vibration corresponding to the lowest natural frequency exhibits a vibratory motion in the middle section of the spring while the ends remain stationary. In contrast, the second vibration mode, which corresponds to a higher frequency, features a node (a point of zero motion among the coils) at the midpoint of the spring. Maximum motion occurs at points one-quarter and three-quarters of the way along the spring from a given end. The natural frequencies associated with these modes of vibration can be calculated.
- *Damping Forces*. Damping forces are present due to various causes, including internal hysteresis in the spring material, air damping, damping due to friction in the end turns, and damping due to energy loss in the supports.
- *Vibration Absorber*. A mathematical model for the vibration absorber is a two-degree-of-freedom system. The primary system represents the degree of freedom of the system and the initial and actual mechanical setup. An absorber consisting of mass, spring, and damping elements is added to the primary system. The excitation of the system acts on the primary mass. Randall et al. propose the following frequency response for the system:

$$\boldsymbol{\alpha} = \frac{\sqrt{\left(1-\frac{\beta^2}{T^2}\right)^2+4\left(\frac{\zeta_2\beta}{T}\right)^2}}{Z} \quad , \tag{1}$$

with

$$Z^2 = \left[\frac{\beta^4}{T^2}-\frac{\beta^2}{T^2}-\beta(1+\mu)-4\frac{\zeta_1\zeta_2\beta^2}{T}+1\right]^2+4\left[\frac{\zeta_1\beta^3}{T^2}+\frac{\zeta_2\beta^3}{T^2}(1+\mu)-\frac{\zeta_2\beta}{T^2}-\zeta_1\beta\right]^2, \tag{2}$$

$$\omega_1=\sqrt{\frac{k_1}{m_1}},\omega_2=\sqrt{\frac{k_2}{m_2}},T=\frac{\omega_2}{\omega_1},\beta=\frac{\Omega}{\omega_1},\mu=\frac{m_2}{m_1},\zeta_1=\frac{c_1}{2\sqrt{k_1m_1}},\zeta_2=\frac{c_2}{2\sqrt{k_2m_2}} \quad . \tag{3}$$

A search for the optimum ζ_2 and T values can be based strictly on the min-max definition of the optimum system. There is a strong correlation between the major system's two peak values. Compared to the second peak, the first peak is lower. The following variables optimum μ, ζ_1, ζ_2, T determine the ideal ratio α.

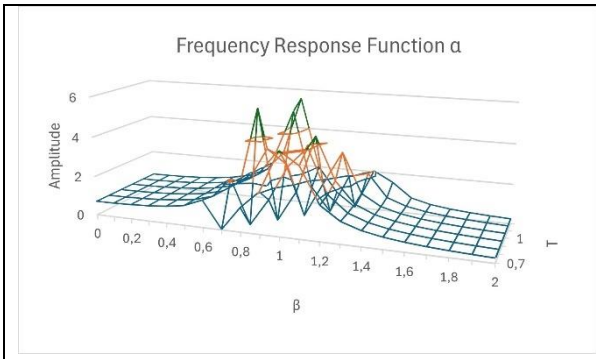

Fig.4: Frequency Response Function α vs. β, T with $\zeta_1 = 0.1, \zeta_2 = 0.01, \mu = 0.1$

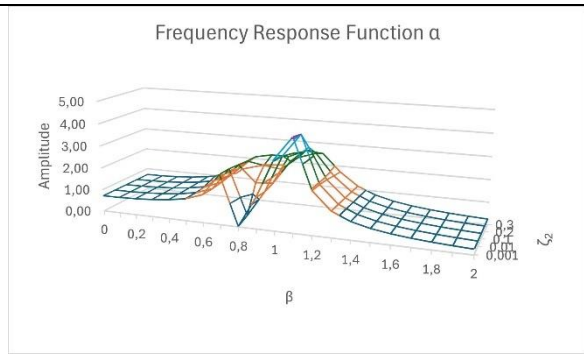

Fig.5; Frequency Response Function α vs. β, ζ_2 with $\zeta_1 = 0.1, \mathrm{T} = 0.8, \mu = 0.1$

RESULTS

Experimental investigations verify the effectiveness of the anti-vibration system. A data logger AX6 activity and a data logger Svantek 106A record the accelerations. The measurement points are the brush cutter shaft and the worker's right and left hands. The brush cutter has the following mechanical characteristics: 41.6 cc / 2.0 kW-2.7 hp/ 8.5 kg.

The optimal design of the mechanical system aims to minimize the frequency response of the secondary system within the range of 0 to 160 Hz. The relationships 1), 2) and 3) provide optimal values: $\mu = 0.1, \zeta_1 = 0.1, \ \zeta_2 = 0.001$, and $T = 0.8$. The mass ratio $\mu = 0.1$ indicates that the mass of the secondary system should be less than that of the primary system (Figure 4). Additionally, a comparison of the damping factors ζ_1 and ζ_2 reveals that the damping factor ζ_2 of the secondary system must be lower than that of the primary system, ζ_1 (Figure 5).

The comparison between primary and secondary systems on RMS and VDV illustrates that the secondary system presents lower RMS (=0.00007 m/s^2) and VDV (=0.016 m/s$^{1.75}$) values than ones of the primary system (Figures 6 and 7).

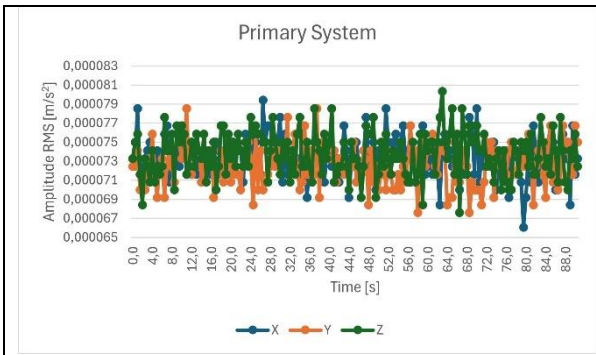

Fig.6: Time response of primary system

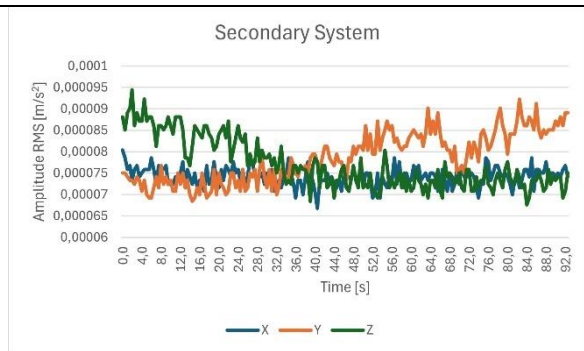

Fig.7: Time response of secondary system

The frequency domain illustrates the effectiveness of the anti-vibration system (Figures 8 and 9). Figure 10 compares the response of the primary and secondary systems in the frequency domain. The figure shows the peak leveling in the 0-1000 Hz frequency range.

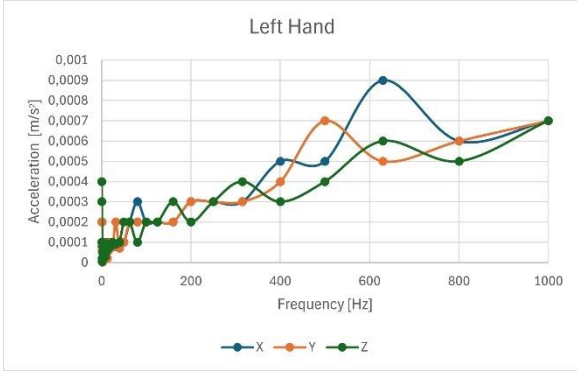

Fig.8: Frequency response function evaluated on left hand

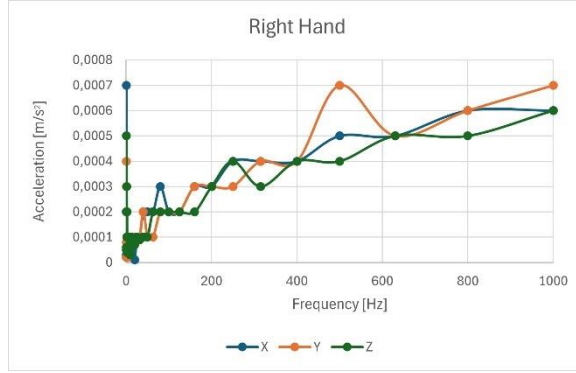

Fig.9: Frequency response function evaluated on right hand

If the worker uses the brush cutter twice a year and has to cut the grass for an area of 5000 m^2, assume a cutting time of 8 hours until you reach the 16 hours of exposure time.

DISCUSSION

Previous research shows that critical resonant frequencies along the z_h-axis for the extended arm posture are 10.9 – 15, 27.7 – 39.9, 87.9 – 99.2, and 97.8 – 110.0 Hz (Table 1). The resonance frequency ranges for the bent-arm posture are 13.0 – 17.3, 27.2 – 36.8, 53.4 – 62.0, 78.1 – 89.9, 152.3 – 154.0, and 164.0 – 169.9 Hz (Table 1).

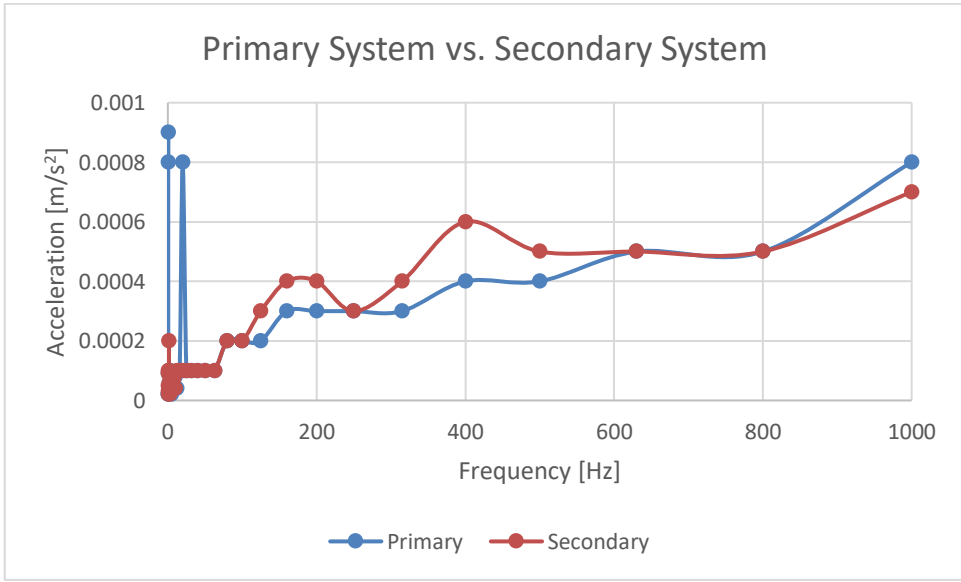

Figure 10: Steady-state amplitude of acceleration vs. frequency of primary and secondary system

Table *1: Resonant frequencies along z_h-axis according to posture of hand arm system*

Posture/Frequencies [Hz]	*1st*	*2nd*	*3rd*	*4th*	*5th*	*6th*
Extended Arm Posture	10.9 – 15.0	*27.7 – 39.9*	*87.9 – 99.2*	*97.8 – 110.0*	---	---
Bent-Arm Posture	13.0 – 17.3	27.2 – 36.8	53.4 – 62.0	78.1 – 89.9	152.3-154.0	164.0 – 169.9

International standards regarding hand-arm vibration include criteria such as finger whitening, which relies on measurements of various independent variables, including vibration magnitude, frequency, and exposure duration. This research presents a method for mitigating the hand-arm vibration produced by brush cutters. Subjective assessments of discomfort indicate that the severity of vibrations may vary across the three cartesian axes. The dynamics of the brush cutter's primary and secondary systems are analyzed to evaluate the accelerations experienced in the left and right hands due to mechanical vibrations. Experimental studies conducted in working conditions alone cannot predict the potential damage linked to specific characteristics of workers' vibration exposures. Research aimed at optimizing professional equipment can significantly alleviate the effects of occupational exposure. While developing mechanical models based on optimization study results is crucial to understanding occupational exposures, a holistic perspective encompasses subjective, biodynamic, physiological, pathological, epidemiological, and mechanical studies.

The primary symptoms associated with exposure to segmental vibrations stem from neurological and vascular disorders and the involvement of tendons, muscles, joints, and bones. Workers exposed to these vibrations often report experiencing paresthesia in the hands, blanching, and numbness in the fingers, muscular weakness, fatigue, and joint pain in the upper limbs. The episodes of finger blanching represent Raynaud's phenomenon of occupational origin, or Vibration-Induced White Finger (VWF). This complex condition, along with other related disabilities, is classified under the broader term Vibration Syndrome.

Critical factors in the onset of vibration-related diseases include the physical characteristics of vibrations, such as amplitude and frequency, along with the duration of exposure. Vibrations characterized by high amplitude and low frequency (below 40 Hz) are associated with osteoarticular lesions. In contrast, those with higher frequencies (ranging from 40 to 1000 Hz) may lead to neurovascular disorders. Additionally, it is essential to consider other contributing factors when assessing the cause of these injuries, including environmental conditions (such as cold), ergonomic factors (such as grip strength, tool handling methods, and working posture), and technical aspects.

When operating the brush cutter, the worker must support the hand tool with both their right and left feet while wearing the shearer’s harness on their shoulders. Vibrations are in three directions: from the hands, feet, and shoulders, affecting multiple points simultaneously. This combined vibration stress impacts the lumbar spine, and prolonged exposure to these vibration levels can significantly impact the worker, potentially leading to a herniated intervertebral disc. Different instruments and working conditions result in varying acceleration levels, and international standards provide additional insights into these issues:

- *Hand arm vibration*. The exposure limit value (ELV) is the maximum vibration value for an operator in a single day. The ELV parameter represents a daily exposure of 5 m/s^2 A(8) for vibration on the hand-arm system. The action exposure value of 2,5 m/s^2 A(8) means a high risk for workers. Workers should use vibration-damping gloves to protect themselves from HAV-prolonged exposure to white finger syndrome (WFS) or Raynaud syndrome.
- *The vibration of the whole body*. Mechanical vibrations, acting on the feet or other parts of the body, produce mechanical vibrations to the whole body. Prolonged exposure to WBV can be associated with severe lumbar pain. For whole-body vibration, the ELV parameter allows a daily exposure of 1.15 m/s^2 A(8), and the EAV allows 0.5 m/s^2 A(8).
- *Biomechanics of the spine*. Brush cutter is supported by a human operator on his shoulders and, simultaneously, on his back. The arms and hands control the brush cutter. The posture of human operators for the operation of mowing the grass is standing and slightly bent forward. The human spine is exposed to mechanical vibration in the following directions: according to shoulder direction and foot direction. The weight of the brush cutter is about 9 Kg, which provides mechanical stress to the human spine.

CONCLUSIONS

This research examines the reduction of vibrations generated by a tool operated by a worker. The components that emit vibrations include the drive shaft, cutting attachment, and motor. Increasing the thickness of the shaft tube in the area designed for the crankshaft bearing, along with ergonomic handle

designs, can lead to a 20% to 30% reduction in mechanical vibration. Also, using elastomer-based materials for the steering wheel handles can provide effective anti-vibration properties. This vibration attenuation is perceptible from the fingers to the elbow and from the elbow to the worker's back.

REFERENCES

[1] M. Futatsuka. 1979."A study on the vibration hazards due to using bush cutters." Japanese Journal of Industrial Health, 21(3):269-273.

[2] Bovenzi M, Petronio L, Di Marino F. 1980. "Epidemiological survey of shipyard workers exposed to hand-arm vibration." Int Arch Occup Environ Health. 1980;46(3):251-66. doi: 10.1007/BF00380015. PMID: 7450890.

[3] Randall, S. E., Halsted, D. M., III, and Taylor, D. L. 1981. "Optimum Vibration Absorbers for Linear Damped Systems." ASME. *J. Mech. Des*. 103(4): 908-913, https://doi.org/10.1115/1.3255005.

[4] Daikoku, Masamichi and Fumitake Ishikawa. 1990. "Hand-transmitted vibration reduction of agricultural machinery (Part 1). Simulation method for vibration reduction." Journal of the Japanese Society of Agricultural Machinery*,* 52: 13-19.

[5] M. Cavacece, E. Pennestrì, P.P. Valentini, and L. Vita. 2004. "Mechanical efficiency analysis of a cardan joint." volume 2 A, 799-808. American Society of Mechanical Engineers.

[6] M. Cavacece and L. Vita. 2004. "Optimal cantilever dynamic vibration absorbers by Timoshenko beam theory." Shock and Vibration, 11(3-4):199–207.

[7] J. Kashima and T. Uemura. 2005, "Analysis of accidents related to brush-cutter use." Journal of the Japan Forest Engineering Society, 25(2):77–84, 2010.741. doi: 10.1115/detc2005-84109.

[8] M. Cavacece, E. Pennestri, and R. Sinatra. 2005. "Experiences in teaching multibody dynamics." Multibody System Dynamics, 13(3):363–-369.

[9] Adewusi, S.A., Thomas, M., & Vu, H.V. 2014. "Natural Frequencies of the Human Hand-Arm System using Finite Element Method and Experimental Modal Analysis." Transaction on Control and Mechanical Systems*, 3*.

[10] M. Cavacece. 2021."Incidence of predisposing factors on the human hand-arm response with flexed and extended elbow positions of workers subject to different sources of vibrations." Universal Journal of Public Health, 9(6):507-519, 2021. doi: 10.13189/UJPH.2021.090620.

[11] M. Cavacece, 2023, "Therapy for the treatment of tinnitus." Otorhinolaryngology(Italy), 73(3):156-159.

[12] M. Cavacece, 2024."Strategies to evaluate musculoskeletal disorders to the human arm hand system using similarity metrics." Journal of Physics: Conference Series 2802 (2024) 012007, doi:10.1088/1742-6596/2802/1/012007.

[13] M. Cavacece. 2024."Distribution of the residual tolerable imbalance between correction plans." Mechanics Based Design of Structures and Machines.

Modification of Psychophysical Laws in Auditory Intensity Perception

Massimo Cavacece[1]

[1] *University of Cassino and Southern Latium, Department of Civil and Mechanical Engineering, Via G. Di Biasio 43, 03043 Cassino (FR), Italy*
cavacece@unicas.it

ABSTRACT

Noise disturbances within the home can lead to a sustained negative evaluation of living conditions. Such disruptions often result in feelings of upset, aggravation, dissatisfaction, worry, irritation, exasperation, discomfort, and distress. Furthermore, these disturbances interfere with essential activities such as communication, recreation, and sleep. The impact of this disorder may also induce changes in blood pressure and provoke defensive responses. This paper presents an Active Noise Control (ANC) system designed to address these disturbances from a psychoacoustic perspective. The proposed process begins by loading the acoustic signal and configuring various parameters, including tone, sample rate, SPL measurement, and frequency weighting employed by the SPL meter. It performs a frequency analysis of the acoustic signal to identify the frequency bands influencing loudness perception. The process subsequently generates visual representations for both time-varying and specific loudness to investigate the acoustic signal further. This methodology evaluates the perceived sharpness of the acoustic signal to assess its overall annoyance level. Additionally, it examines modulation frequencies, highlighting that low-frequency modulations significantly impact perceived annoyance.

Keywords: Psychophysical Laws, Auditory Intensity, Perception, Active Noise Control

INTRODUCTION

In most psychophysical experiments, Stevens' power law equation accurately describes the relationship between sensory magnitude judgments and stimulus magnitude. This equation must be more accurate for weak stimuli near the absolute threshold. The logarithm of apparent magnitude, plotted against the logarithm of stimulus magnitude, appears linear (a power function) only at higher stimulus values. At stimulus values near the absolute threshold, the relationship becomes concave downward. Stevens' power law explains nonlinearity, correlating the perceived intensity of a stimulus (e.g., discomfort caused by noise) to the actual intensity of the stimulus (e.g., noise level) through observation. The exponent α signifies the rate at which discomfort related to noise increases with the rise in the actual intensity of the noise. Studies on the increase in noise discomfort did not conclusively demonstrate that discomfort depends on frequency. The discomfort growth rate, α, varies across noise frequencies and wave directions. Consequently, a noise with a specific frequency, direction, and position may cause less discomfort than another noise with different characteristics.

Psychoacoustic parameters enable us to quantify subjective discomfort or pleasantness that specific sounds evoke in individuals using objective metrics. The Zwicker model introduces a general discomfort parameter (PA) based on several psychoacoustic factors: Volume (L), Sharpness (S), Force of fluctuation (F), and Roughness (R). This model accounts for the anatomy of the human ear, comprising filters in the cochlea. Subjective experiences of discomfort or pleasure reflect sound quality, and sound's aesthetic, cognitive, and acoustic effects can significantly influence these perceptions. Psychoacoustic discomfort depends on the sound's volume, tone, and temporal structure. Technical sounds—such as those produced by cars, air conditioners, or tools like circular saws and drills—can lead to psychoacoustic annoyance. As a result, annoyance cannot be solely predicted by the sound pressure level (SPL). While sonority may be directly related to SPL, noise pertains to the extent to which individuals are disturbed by a sound. Furthermore, noise refers explicitly to the quality of the sound itself, distinguishing between clarity and the feelings of irritation or unacceptability it may provoke.

The research on the perception of noise shows that noise exposure is likely to affect mental health, as the brain is the primary target organ for noise-mediated effects. Exposure to environmental noise is a

considerable factor influencing public health. It causes cardiovascular disorders and adverse effects on the brain. Noise cans, such as traffic, have the potential to impact the central nervous system, increasing susceptibility to mental health conditions like depression and anxiety.

Earplugs, ear protection devices, soundproof walls, silencers, and sound-absorbing materials are all examples of passive noise control techniques aimed at reducing sound levels. These passive strategies are effective across a broad range of frequencies. However, they often necessitate costly and less efficient materials for low-frequency noise. In contrast, active noise control (ANC) provides a solution for effectively reducing low-frequency sounds. Active Noise Control (ANC) is an electro-acoustical technique grounded in the principle of superposition. The ANC system generates anti-noise with the same amplitude but in the opposite phase to cancel out unwanted primary noise acoustically, reducing residual noise. ANC systems are particularly effective at attenuating low-frequency noise in situations where passive noise control methods are costly, cumbersome, and less effective.

The noise level is not the sole factor contributing to irritation. After reducing low-frequency components, the prominence of high-frequency components can heighten irritation as the clarity of the noise becomes more apparent. A more effective noise control strategy is implementing a filter that considers psychoacoustic considerations. An active noise cancellation (ANC) system designed with psychoacoustic properties enhances performance from a psychoacoustic perspective. This paper proposes a psychoacoustic ANC system that can control the disturbance from a psychoacoustic point of view. Loudness, the perceived force of fluctuation, and roughness of the acoustic signal are the psychoacoustic criteria for evaluating the system's noise reduction performance. Simulation results show the effectiveness of the proposed psychoacoustic ANC system.

Table 1: Pseudocode

#	***Description***
1	Load acoustic signal, Specify the tone, the sample rate, the SPL reading, and the frequency weighting of the SPL meter
2	L'analisi in frequenza del segnale acustico individua le bande di frequenza che contribuiscono alla sensazione percettiva del volume
3	Plot time-varying loudness and specific loudness to analyze the acoustic signal
4	Estimate the perceived sharpness level of an acoustic signal to estimate the contribution to its overall annoyance level.
5	Evaluate the modulation frequencies present in the signal. Low-frequency modulations contribute to the perceived annoyance level.
6	Calculate the perceived force of fluctuation of the acoustic signal
7	Compute the perceived roughness of the acoustic signal
8	Plot the tone-to-noise ratio of the acoustic signal
9	Combine the previous metrics to produce the psychoacoustic annoyance metric
10	Measure the impact of improved soundproofing on the measured SPL and the perceived noise.
11	Design an equivalent Filter Bank to simulate the attenuation of the proposed soundproofing
12	Compare the perceived loudness measurements before and after soundproofing
13	Calculate the reduction in the psychoacoustic annoyance factor

METHODS

The qualitative relationship between sound and impression and the quantitative relationships between acoustic stimuli and auditory sensations significantly affect the human auditory system's capacity to receive information. In a steady state, sounds can be associated with sensations of intensity or pitch, referred to as sound timbre. Timbre is a characteristic of sound that enables differentiation between two sounds that share the same frequency or pitch. It is an attribute of auditory sensation, allowing the listener to identify the sound source, making it distinct from others. Sound height, duration, and intensity can be accurately quantified and ordered on a scale, as these physical properties are objective and measurable.

In contrast, timbre is a multidimensional quality encompassing sensations such as sonority, sharpness, roughness, and floating force. Sonority pertains to the subjective perception of a sound's magnitude on a semantic scale, which ranges from silence to loud sounds. Sharpness reflects the sensation of sensory pleasure, while the rapid variations in modulation frequencies between 15-300 Hz contribute to the perception of sound roughness. Lastly, the force of acoustic fluctuation represents a perceptual measure of slow modulation in amplitude or frequency at low frequencies (below 20 Hz) within a signal. The psychoacoustic nuisance metric articulates the relationship as follows:

$$PA = N_5\left(1 + \sqrt{w_S^2 + w_{FR}^2}\right) \quad , \tag{1}$$

with

- N_5 is the percentile loudness in sone (level that is exceeded only 5% of the time);
- $w_s = (S - 1.75)[0.25\ \log(N_5 + 10)]$, for $S > 1.75$, where S is the sharpness in acum;
- $w_{FR} = \frac{2.18}{(N_5)^{0.4}}(0.4\ F + 0.6\ R)$, where F is the fluctuation strength in vacil;
- R is the roughness in asper.

Table 1 describes the steps of the proposed algorithm. The algorithm begins by loading the acoustic signal and setting parameters such as tone, sample rate, SPL measurement, and frequency weighting used by the SPL meter. It performs a frequency analysis of the acoustic signal to identify the frequency bands contributing to the loudness perception. The algorithm subsequently generates plots for both time-varying and specific loudness to examine the acoustic signal further. This methodology assesses the perceived sharpness of the acoustic signal to evaluate its overall annoyance level. It analyses the modulation frequencies, noting that low-frequency modulations significantly impact perceived annoyance. The perceived fluctuations within the acoustic signal are then evaluated, leading to the computation of the perceived roughness associated with the signal, which visualizes the tone-to-noise ratio. By integrating these metrics, the psychoacoustic annoyance index assesses the impact of improved soundproofing on measured SPL and perceived noise levels. The technique also designs a corresponding filter bank to model the attenuation effects of the proposed soundproofing solution, allowing for a comparison of perceived loudness measurements taken before and after installation. Ultimately, this process determines the reduction in the psychoacoustic annoyance factor.

RESULTS

The acoustic signal presents SPL (LCF) and peak SPL (LCF_{peak}) patch as shown in Figure 1. In the hypothesis of a free-field recording, the stationary loudness assumes a peak value in the field 15-18 Bark scale or 2900-3500 Hz (Figure 2) according to ISO 532-1.

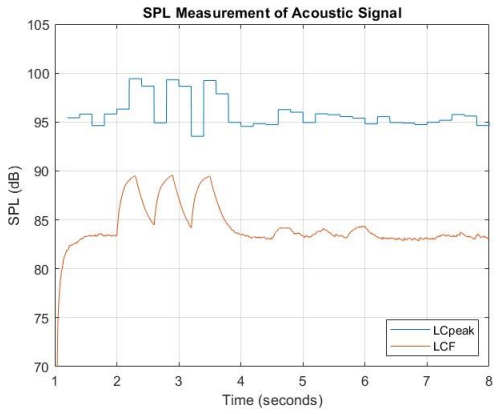

Fig. 1 - SPL (LCF) and peak SPL (LCFpeak) of the acoustic signal

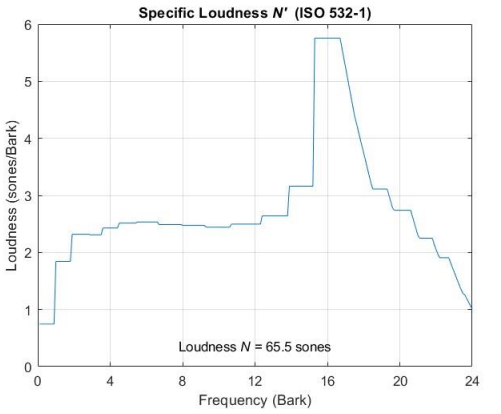

Fig. 2 - Stationary loudness in Bark scale assuming a free-field recording

The patch time-varying loudness illustrates three high peaks of the acoustic signal from 2 to 4 s and the lowest peaks from 4.5 to 6 s. Specific loudness in the frequency domain shows that the high and lowest peaks of the acoustic signal are in the field 16-20 Bark scale (Figure 3). Perceived fluctuation intensity increases from 0 to 3 seconds, takes a maximum value of 3 to 6 seconds, and decreases from 6 to 8

seconds (Figure 4). Similarly, the specific fluctuation strength (vacils/Bark) changes from 0 to 3 seconds and from 0.5 to 23.5 Bark scale (Figure 4).
The perceived sharpness of the acoustic signal shows a constant contribution to its overall annoyance level (Figure 5). Low-frequency modulation contributes significantly to perceived discomfort (Figure 6).
Helmholtz attempted to bring together the boundaries of two disciplines, despite their many natural similarities, which had remained separate: the boundaries of physical and physiological acoustics on one side and music science and aesthetics on the other. Roughness is a fundamental hearing sensation for fast amplitude modulations (Figure 7). The evaluation of the perceived roughness of the acoustic signal in Hz scale shows maximum values in the field 250-1000 Hz (Figure 8).

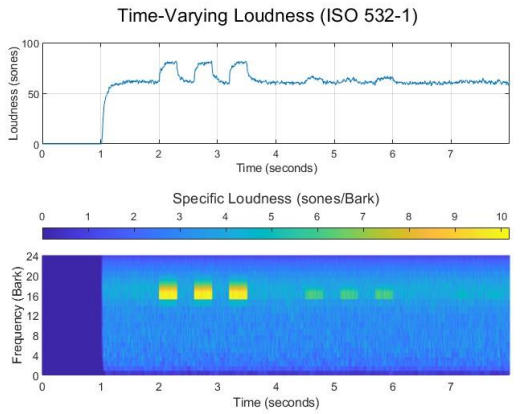

Fig. 3 - Plot time-varying loudness and specific loudness to analyze the acoustic signal

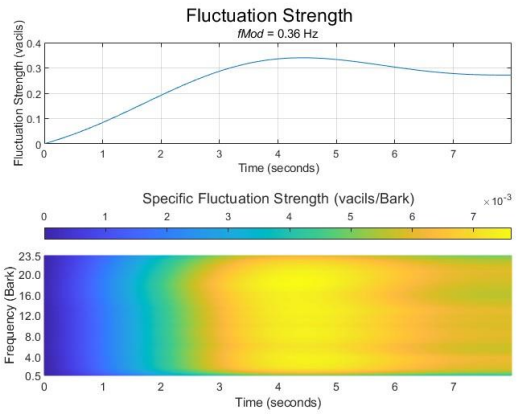

Fig.4 – Evaluation of the perceived fluctuation strength with frequency in Bark scale

The tone is a significant characteristic of the beep. The interplay between tone and other sounds underscores the importance of tone over noise. The signal-tone-noise ratio provides insights, including a prominence indicator. Notably, hue metrics do not require a calibration factor. The tone-to-noise ratio derived from the power spectrum of the acoustic signal reveals a peak around 3000 Hz (Figure 9).
Additionally, the spectrogram displays a series of peaks occurring between 3 and 6 seconds and around 3000 Hz (Figure 10). The digital filter (Figure 11) simulates the attenuation of the proposed soundproofing (Figure 12). Low frequencies are more complex to attenuate.
The original acoustic signal presents the following values: sharpness 2.1 [acum], 82.83 PA, and loudness 85.7 [phons]. The acoustic signal with soundproofing obtains the following optimal values: sharpness 2.1 [acum], 58.52 PA, and loudness 5.5 [phons].

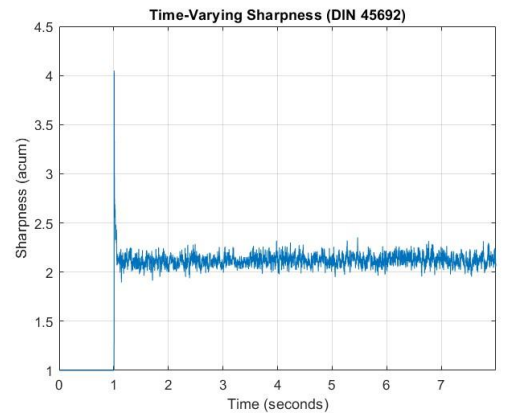

Fig.5 – The contribution of the perceived sharpness of the acoustic signal on its overall annoyance level

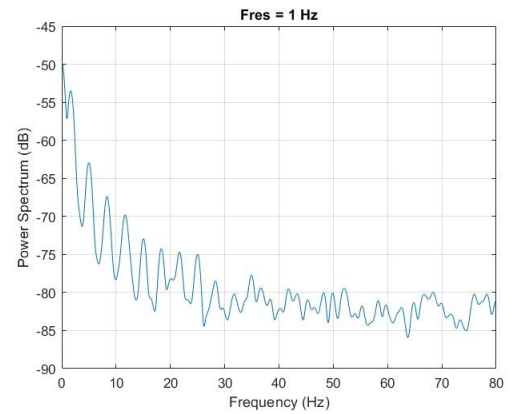

Fig.6 – The contribution of low-frequency modulations on the perceived annoyance level

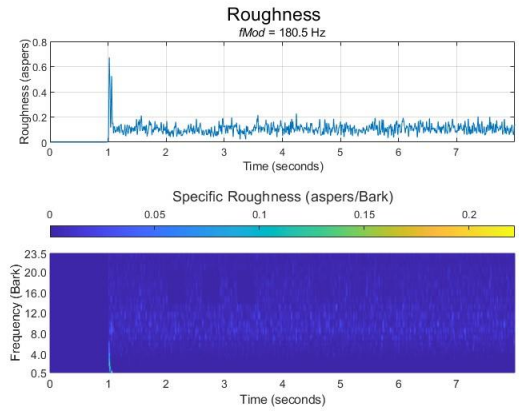

Fig.7 – Evaluation of perceived roughness of the acoustical signal in Bark scale

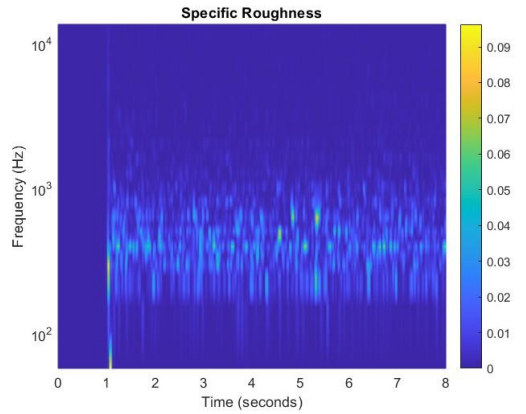

Fig.8 – Evaluation of perceived roughness of the acoustical signal in Hz scale

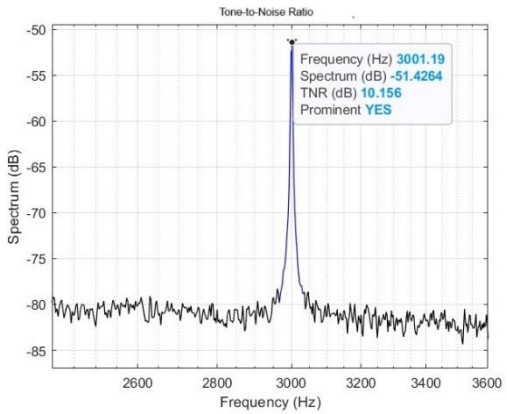

Fig.9 – The tone-to-noise ratio by the power spectrum of the acoustic signal

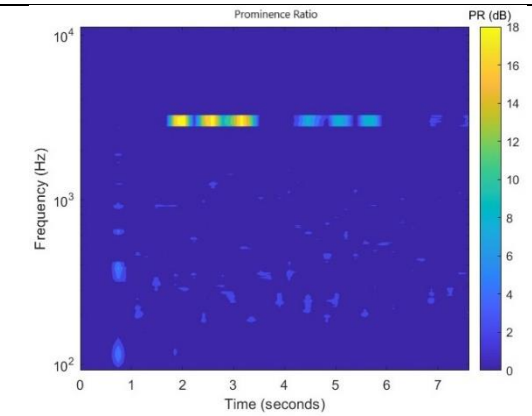

Fig.10 – The prominence ratio of the acoustic signal
at 2-4 s and 3000 Hz

DISCUSSION

Low-frequency noise, characterized by a frequency range of approximately 10 Hz to 200 Hz, poses a significant environmental noise issue, particularly for sensitive individuals in their homes. Traditional methods for assessing noise nuisance, typically relying on the A-weighted equivalent sound level, are insufficient for effectively addressing low-frequency noise. Many laboratory measurements examining the nuisance associated with various spectra and levels of low-frequency noise complicate direct comparisons. Notably, the perception of nuisance escalates rapidly with increasing sound levels, and A-weighted measurements tend to underestimate the impact of low-frequency noise. This type of noise can lead to discomfort and stress for those affected.

Elevated noise levels can impair hearing and contribute to increased blood pressure, disrupt sleep, and hinder productivity and learning. While noise pollution may not always receive the same attention as more visible pollutants, public awareness of its detrimental effects has grown significantly. Acknowledging the public's concerns, companies have started developing active noise control solutions to mitigate low-frequency sounds, typically those below 600 Hz, which often evade conventional noise reduction techniques.

Active control systems in development or production stages aim to reduce noise from electric motors, transformers, jet engines, automobile, truck, and bus exhaust systems. Active noise-control systems operate on the principle that a sound can be effectively canceled out by producing a second sound wave that is nearly identical but 180 degrees out of phase with the original. In these systems, microphones capture the unwanted sounds to send to a digital processor. Utilizing advanced signal-processing software and algorithms that generate repetitive or random noise, the processor creates anti-noise signals transmitted through loudspeakers to eliminate offending sounds.

The psychoacoustic analysis presents the following reflections:

1. The initial realization is acknowledging that absolute silence does not exist. The psychoacoustic framework indicates that scenarios devoid of sound are essentially unattainable; identifiable and measurable sounds are always present. While silence is perceptible, this paradox necessitates reevaluating its definition, highlighting the limitations of merely defining silence as the absence of sound.
2. Silence is a sonorous form. Indeed, defining silence as the result of the perception of a class of sound forms is the result of assuming the paradox that silence exists and, simultaneously, that the total absence of sound is impossible.

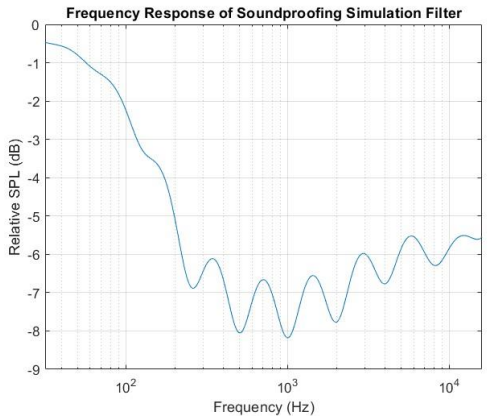

Fig. 11 – Frequency Response of Soundproofing Simulation Filter

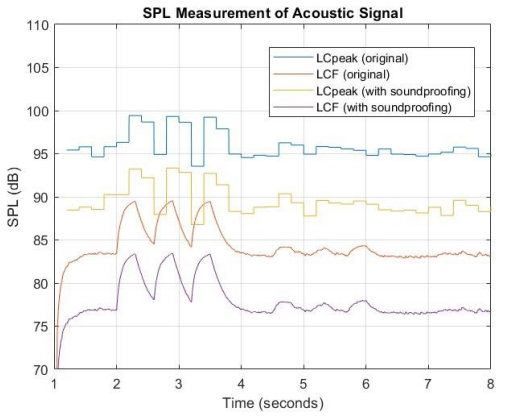

Fig. 12 – Comparison between the SPL with and without soundproofing

CONCLUSIONS

The general description of discomfort encompasses a constant hum, palpitations, ear, head, or body pain, vibrations or aches, loss of concentration, nausea, and sleep disturbances. However, the perception of low-frequency disturbance varies from person to person. The research proposes a specific method for evaluating low-frequency noise by considering noise quality, fluctuations, sharpness, and roughness. It also suggests an approach for developing a digital filter to reduce low-frequency nuisance.

REFERENCES

[1] Zwislocki, J. J. An analysis of some auditory characteristics. In R. D. Luce, R. R. Bush, & E. Galanter (Eds.). 1965. Handbook of mathematical psychology (Vol. Ill). New York: Wiley.

[2] Stevens, S. S. 1975. Psychophysics: Introduction to its perceptual, neural and social prospects. New York: Wiley.

[3] S. Kuwano, S. Namba, H. Fastl, 1988. “On the judgment of loudness, noisiness and annoyance with actual and artificial noises.”Journal of Sound and Vibration, Volume 127, Issue 3, 457-465, ISSN 0022-460X, https://doi.org/10.1016/0022-460X(88)90370.

[4] Leventhall HG. 2004. “Low frequency noise and annoyance.” Noise Health. 2004 Apr-Jun;6(23):59-72. PMID: 15273024.

[5] Bao, H., Panahi, I., 2010. “A novel feed forward active noise control structure with spectrum-tuning for residual noise”. IEEE Trans. Consum. Electron., 56 (4), 2093-2097.

[6] Bao, H., Panahi, I. 2010. “Psychoacoustic active noise control based on delayless subband adaptive filtering.” Proc. of ICASSP 2010, 341-344.

[7] Wang, T.W., Gan, W.S, Chong, Y.K. 2012. “Psychoacoustic hybrid active noise control system.” Proc. of ICASSP 2012.

[8] Zwicker, Eberhard, and Hugo Fastl. 2013. *Psychoacoustics: Facts and Models*. Vol. 22. Springer Science & Business Media.

[9] Soeta, Y., & Ando, Y. 2015. “Neurally Based Measurement and Evaluation of Environmental Noise.” Mathematics for Industry, Springer, Vol.20, DOI:10.1007/978-4-431-55432-5, Corpus ID: 64096521.

[10] Guo-Qing Di, Xing-Wang Chen, Kai Song, Bing Zhou, Chun-Ming Pei. 2016. “Improvement of Zwicker’s psychoacoustic annoyance model aiming at tonal noises.” 2016. Applied Acoustics, Volume 105, 2016, 164-170, ISSN 0003-682X, https://doi.org/10.1016/j.apacoust.2015.12.006.

[11] Xieqi Chen, Jianhui Lin, Hang Jin, Yan Huang, Zechao Liu. 2021. “The psychoacoustics annoyance research based on EEG rhythms for passengers in high-speed railway.” Applied Acoustics, Volume 171, 107575, ISSN 0003-682X, https://doi.org/10.1016/j.apacoust.2020.107575.

[12] Guoqing D, Cong C, Yao Y, Li D, Jian W. 2022. “A study on the conversion relationship of noise perceived annoyance and psychoacoustic annoyance-a case of substation noise.” Journal of Low Frequency Noise, Vibration and Active Control. 2022;41(2):810-818. doi:10.1177/14613484211068308.

[13] Cavacece, M. 2023. “The noise of rail transport.” volume 2590. Institute of Physics.

[14] Cavacece, M. 2023. “Therapy for the treatment of tinnitus.” Otorhinolaryngology (Italy), 73(3):156-159.

An investigation into the use of magnetic materials in the repair of damaged peripheral nerves

Maz Aljunaydi[1], Gillian Pearce[2], Philip Langley[1]

1. *School of Biomedical Engineering, Hull University, HU6 7RX ;*
2. *School of Engineering and Physical Sciences, Aston University, B4 7ET;*

ABSTRACT

This study investigates the use of magnetic materials to improve axon alignment in severed peripheral nerve. The research objective is to enhance nerve alignments by utilising magnets in comparison to the traditional epineural nerve repair method. The experimental design involved creating a simulated nerve model, using Polycraft T15 silicone rubber to represent the nerve, copper wires to represent axons, and neodymium magnets, testing different configurations of magnets for aligning nerve fascicles. A model was constructed, based on human sciatic nerve measurements. Analytical techniques included measuring electrical resistance across the model to assess the alignment's effect on nerve axons. The results showed that the use of magnets resulted in better axon alignment than the epineural suturing technique, with significantly reduce resistance where the mean for the magnets was 0.83 ohm vs 1.03 ohm for the epineural nerve repair, indicating enhanced conductivity in magnet-aligned models. Statistical analysis revealed non-significant difference in variability of resistance measurements suggesting the techniques are equally repeatable as the mean of the standard deviation was 0.154 ohm for the magnet's method vs 0.145 ohm for epineural nerve repair. In comparison with previous studies on nerve repair, which primarily focus on chemical and physical cues, the study highlights magnets as a promising potentially offering a significant improvement for nerve repair outcomes. The main conclusion is that magnetic materials provide a novel and effective method for enhancing nerve alignment, potentially offering a significant improvement for nerve repair. This approach may pave the way for further advancements in biomedical engineering, with implications for peripheral nerve injury treatments.

INTRODUCTION

Peripheral nerve injuries are a significant clinical challenge, affecting 2.8% of multiple trauma patients and up to 5% when including root and plexus injuries(Benga et al, 2017). These injuries disrupt the nerve's ability to regenerate naturally, necessitating medical interventions. According to Burnett and Zager (Burnett & Zager, 2004) more than 1 million people worldwide experience peripheral nerve injuries every year. Existing approaches, including microsurgical techniques such as autografting and epineural nerve repair using the Kessler method, serve as the gold standard for nerve repair but face limitations in promoting optimal nerve alignment. Figure 1 shows a two-strand Kessler repair of the two sections of two severed ends of the nerve stitched together through the epineurium in two figures of 8 sutures.

According to Benga (Benga et al, 2017), prior research has investigated various approaches to enhance nerve regeneration, with chemical and physical cues being a focal point. The development of biomimetic scaffolds and research into growth factors like cytokines has demonstrated promising results for nerve regeneration. However, these methods have their drawbacks, such as inconsistent outcomes and complexities in practical applications. Recent studies have investigated the combined use of magnetic field stimulation, iron oxide nanoparticles, and aligned electro spun fibres to promote neurite outgrowth from dorsal root ganglia in vitro.

The use of magnetic nanoparticles for a magnetic orientation approach is one of the most common methods for remotely controlling the alignment of fibres during scaffold formation. This approach leverages magnetic fields to provide physical cues for guiding nerve regeneration and alignment. Despite preliminary successes, the efficacy of magnetic materials as a technique for nerve alignment remains under-explored, leaving a gap in the field (Soetaert et al, 2020).

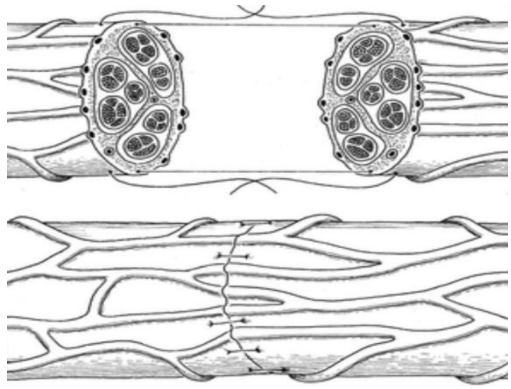

Figure 1: Two ends of the nerve stitched together (Wolfe, 2000)

The specific objective of this study is to investigate the potential of magnetic materials in improving axonal alignment within simulated nerve fibre models. The hypothesis posits that using magnets to align severed nerve sections will yield superior outcomes compared to the current epineural repair techniques. This research is crucial as it addresses the need for improved methods of nerve repair, with the potential for enhancing recovery from peripheral nerve injuries.

This study will focus on developing and testing simulated nerve models embedded with magnetic materials to evaluate their effect on axon alignment. Key limitations include the inability to fully replicate the complex biological environment of live tissues within the experimental setup. The subsequent sections will cover a detailed literature review, the experimental design and methodology, results from the magnetic and non-magnetic models, and a final discussion on the findings and their broader implications.

MATERIALS & METHODS

This study aimed to explore the potential of magnetic materials in aligning nerve fibres in severed peripheral nerves, hypothesising that magnets could enhance axon alignment and improve regeneration outcomes compared to traditional suturing techniques, such as epineural nerve repair. Two distinct nerve models were constructed to test this hypothesis: one representing traditional epineural repair and the other utilising magnets to facilitate nerve alignment. The nerve models were designed to simulate human peripheral nerves, specifically the sciatic nerve, which typically measures approximately 20 mm in diameter (Davis et al,2021). Therefore the outer diameter of the models was 20 mm. Studies found that the fascicle diameters ranged from 0.2 to 3 mm, with a mean diameter of 1.7 ± 0.8 mm (Tsur et al,2018). Therefore 1.5mm wire diameter is used to represent the fascicle diameter.

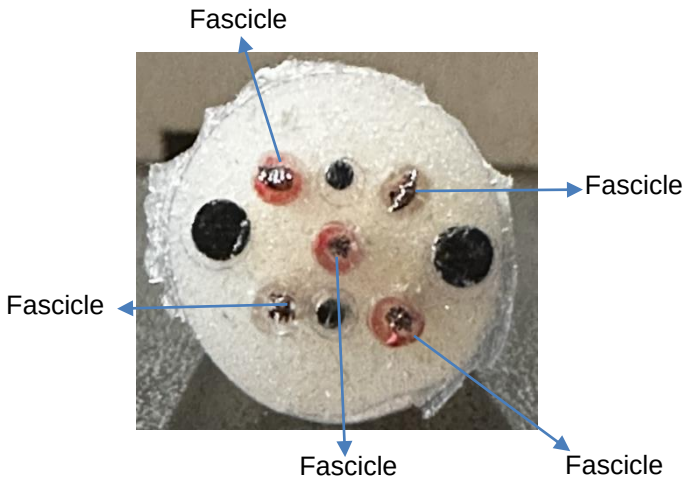

Figure 2. Cross section of synthetic nerve material showing positions of fascicles.

According to Snell (Snell,2010), The distance between fascicles can be up to 2mm distance, however, it's important to note that the exact distance between fascicles in human peripheral nerve varies from person to person as it's difficult to have an average estimate. Other sources and studies may provide slightly different measurements or ranges. Additionally, the fascicle-to-fascicle distance may also be influenced by factors such as age, sex, body size, and medical conditions that affect nerve function or morphology. Therefore, the fascicle-to-fascicle distance in this experiment was 2 mm from one fascicle to another. The average number of nerve fascicles is between 4-5 fascicles (Antunes et al, 2012). Figure 2 shows the cross-section of synthetic nerve material showing the positions of fascicles. Ethical approval was not required, as the study involved no human or animal subjects, relying solely on simulated nerve models.

The materials and equipment used in the construction of the nerve models included an Ultimaker 3D printer with Polylactic Acid (PLA) as the printing material for the creation of the shape of the nerve as shown in figure 3 and 4, Neodymium magnets of various diameters (2 mm and 4 mm) and 1.5 mm stranded copper wires to represent nerve fascicles.

Figure 3 shows the 3D printed half-cylinder made from PLA

Silicone rubber, specifically Polycraft T15 Translucent RTV Addition Cure Silicone Rubber, was used to mould the nerve models, while nylon micro monofilament nonabsorbable sutures, in sizes 8-0 and 10-0, were employed in the epineural repair model. The nerve model designs were created using SolidWorks, and electrical resistance readings were taken using a digital multimeter to test nerve fibre alignment.

For the construction of the models, two different approaches were used. In the magnetic alignment model, magnets were inserted into cylindrical cup compartments at the ends of the nerve model as shown in figure 4, designed to hold the fascicles in place and promote correct position.

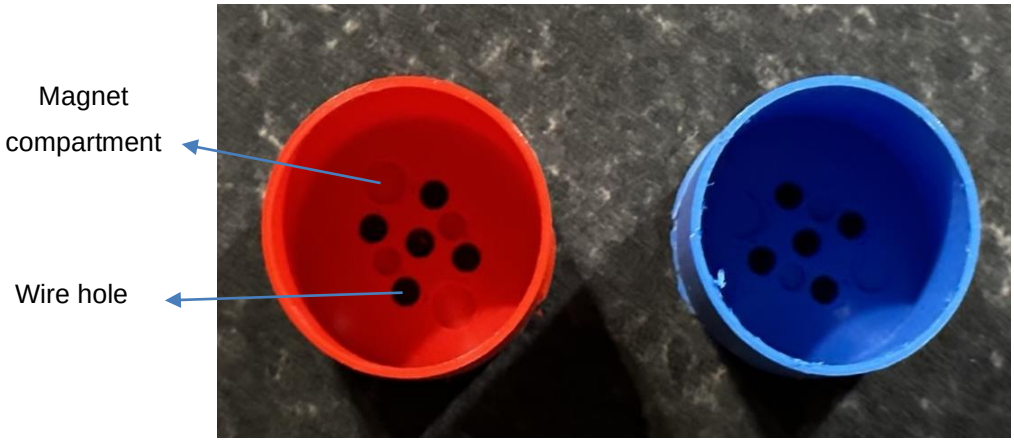

Figure 4 shows the 3D printed two cylindrical cups made from PLA

The cylinder and the cups were put together to create the nerve shown in figure 5.

Figure 5 shows the assembled parts for the nerve model

In the epineural repair model, the nerve ends were joined using nylon sutures, placed 90 degrees apart to ensure even distribution of tension and proper alignment of the nerve fibres as shown in figure 6.

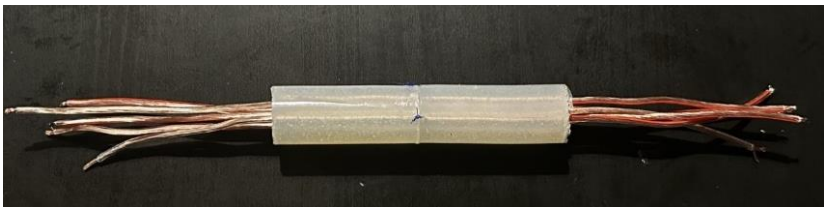

Figure 6 shows the full epineural repair model being modelled

Figure 7 displays the fully constructed and aligned model with the use of neodymium magnets, which are ready for testing to obtain resistance measurements.

Figure 7 shows the full magnet model being modelled

PLA was chosen as the 3D printing material due to its biodegradability and ease of use, while silicone rubber was selected for its biocompatibility and mechanical properties, ensuring the nerve models accurately represented the physical characteristics of human peripheral nerves.

The experimental procedures involved two primary tests. The first was the magnet alignment experiment, where Neodymium magnets of varying sizes were inserted into the nerve model ends, and electrical resistance measurements were taken using a digital multimeter as shown in figure 8.

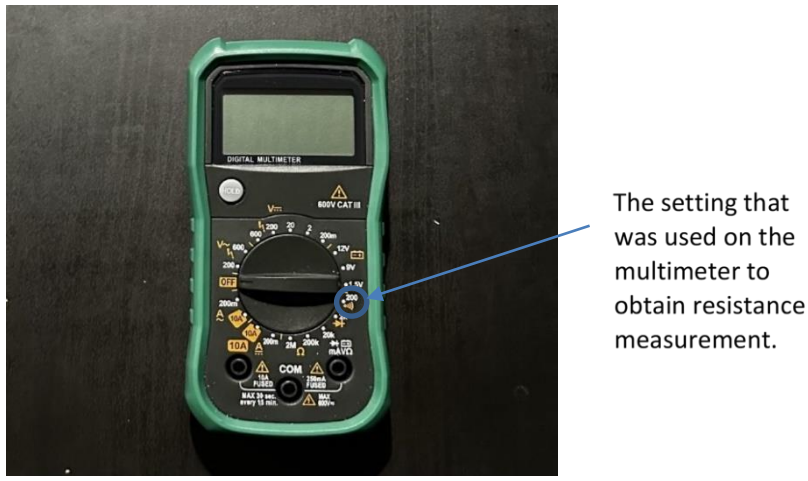

Figure 8 displays the multimeter used to obtain resistance measurements

These measurements were used to evaluate the alignment of nerve fascicles and assess the effectiveness of the magnets in promoting proper nerve alignment. The second experiment involved traditional epineural repair, where sutures were used to reconnect the nerve ends, and similar resistance measurements were taken for comparison with the magnetic alignment model. Both models were constructed with five fascicles, represented by copper wires, and the same experimental protocol was followed for consistency.

Data analysis was conducted by comparing the resistance readings obtained from the two models, the original measurements and data can be provided by the first author upon request. Mean resistance values were calculated for both the magnetic and sutured models, and standard deviations were used to assess the variability of the measurements. The data were recorded in Microsoft Excel and analysed to determine whether the use of magnets significantly improved nerve fibre alignment compared to the traditional suturing method. Multiple readings were taken for each model to ensure the reliability of the results, and any anomalies were addressed by recalibrating the multimeter and rechecking the experimental setup.

Quality control measures were implemented throughout the experimental process. The 3D printing and moulding materials were carefully inspected to ensure consistency, and the silicone rubber was poured into the moulds with precision to avoid any imperfections that could affect the results. The digital multimeter was calibrated before each session, and all readings were taken under identical conditions to minimise variability. Additionally, each model was constructed and tested multiple times to ensure the repeatability and validity of the findings.

Since no human or animal subjects were involved, ethical considerations were limited to ensuring the integrity and accuracy of the data reported. The study adhered to best practices in material engineering and model validation, and no formal ethical approval was required. Established microsurgical techniques for epineural nerve repair were referenced throughout the study, while the magnetic alignment method was exploratory, drawing from recent developments in magnet-based nerve regeneration research.

RESULTS AND DISCUSSION

The experiments compare the effectiveness of the Epineural nerve repair method, which involves stitching the epineurium, to the use of magnets method to aid in alignment for nerve regeneration in both models.

For the model experiment, copper wires with a diameter of 1.5 mm and a length of 165mm for each half of the model were used, along with neodymium magnets with diameters of 2 mm and 4 mm.

The resistance was measured to an accuracy of +/- 0.1 ohm. These are displayed graphically in figures 9 and 10. Based on the data, which can be provided by the first author upon request, we constructed a graph displaying the means and standard deviations for both the magnets and the epineural nerve repair experiment. Figures 9 and 10 show resistance in ohms on the x-axis and the mean of the epineural nerve repair method (sew)and magnets y- axis.

Figure 9 result shows significantly reduce resistance where the mean for the magnets was 0.83 ohm vs 1.03 ohm for the epineural nerve repair, indicating better nerve alignment, for the repair with the magnets compared with epineural nerve repair, where an unpaired t test was performed with p value of 0.0017, where $p<0.05$.

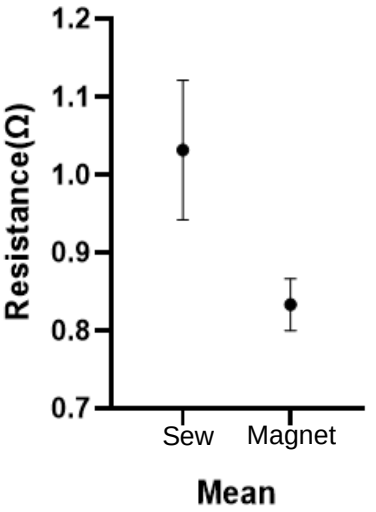

Figure 9 shows the resistance mean results for model one experiment with and without magnets

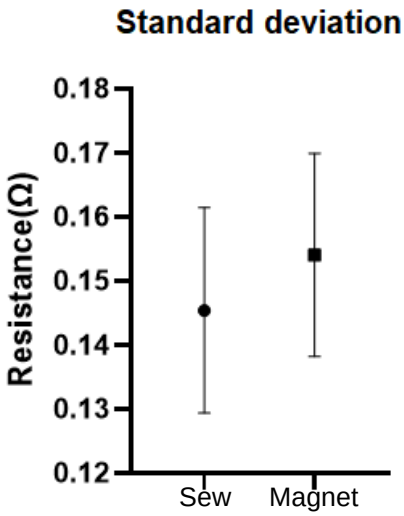

Figure 10 shows the resistance standard deviation results for model one experiments with and without the magnets.

Figure 10 shows non-significant difference in variability of resistance measurements suggesting the techniques are equally repeatable as the mean of the standard deviation was 0.154 ohm for the magnet's method vs 0.145 ohm for epineural nerve repair. Where unpaired t test was performed with p value of 0.4167, where $p < 0.4167$.

The magnets demonstrated better nerve alignments compared to epineural nerve repair. This suggests the potential use and further investigation of magnetic materials to aid in nerve repair. Further research in this area is needed to explore the possibility of magnets and their application to actual nerves, notwithstanding the need for biocompatible magnetic materials or biocompatible coatings on such magnets. Nevertheless, using magnetic materials in nerve repair holds potential for application in nerve repair. The magnetic materials could possibly be incorporated into a nerve scaffold or conduit placed at the nerve injury site to guide the regenerating nerve fibres along a specific path. One potential approach would be to create a magnetic scaffold composed of magnetic nanoparticles of opposite polarity embedded in a biodegradable polymer matrix. This scaffold could be implanted at the site of the nerve injury and used to guide the regenerating nerve fibres along a specific path through the application of a magnetic field.

An external magnetic field gradient might also be applied to such a scaffold to encourage nerve repair. The toxicity of nanoparticle materials would be an important factor in such an approach, Stern (2008). Yet another approach might potentially involve creating a nerve conduit coated with magnetic materials. The nerve conduit would be placed at the site of the nerve injury, and the magnetic field would be applied externally, guiding the regenerating nerve fibres along the magnetic gradient created by the magnetic coating on the nerve conduit. While these approaches are potentially promising, more research is needed to determine the safety and efficacy of using magnetic materials in human nerve regeneration. Studies need to be conducted to investigate the biocompatibility of the magnetic materials. Additionally, the optimal magnetic properties, field strength, and duration of exposure need to be determined for optimal nerve repair outcomes.

CONCLUSIONS

Our research suggests that magnets resulted in better nerve alignment compared to traditional repair methods. Magnetic materials show promise in aiding nerve repair, especially when combined with scaffolds, magnetic gradients, or external magnetic fields. Neodymium magnets proved effective, but further research is needed to optimise their field strength and composition. Although our study used a synthetic nerve model, the results present a novel approach to nerve repair with magnetic materials, warranting further investigation.

While these approaches are promising, more research is needed to determine the safety and efficacy of using magnetic materials in human nerve regeneration. Studies need to be conducted to investigate the biocompatibility of the magnetic materials and the potential for adverse effects on nerve regeneration. Additionally, the optimal magnetic properties, field strength, and duration of exposure need to be determined for optimal nerve regeneration outcomes.

REFERENCES

Antunes, L., Demir, A G., & El Fakouri, R. (2012). The use of digital models for planning and executing peripheral nerve surgery. Acta Neurochirurgica, 154(6), 1023-1028. Azevedo, Frederico A.C., et al. "Equal Numbers of Neuronal and Nonneuronal Cells Make the Human Brain an Isometrically Scaled-up Primate Brain." The Journal of Comparative Neurology, vol. 513, no. 5, 10 Apr. 2009, pp. 532-541, 10.1002/cne.21974.

Burnett, M.G., & Zager, E.L. (2004). Pathophysiology of peripheral nerve injury: A brief review. Neurosurgical Focus, 16(5), 1-7. https://doi.org/10.3171/foc.2004.16.5.2.

Davis, David, et al. "Sciatica." PubMed, StatPearls Publishing, 2021, pubmed.ncbi.nlm.nih.gov/29939685/. Accessed 2 Oct 2024.

Snell, R. S. (2010). Clinical anatomy by regions (9th ed.). Lippincott Williams & Wilkins.

Soetaert, Frederik, et al. "Cancer Therapy with Iron Oxide Nanoparticles: Agents of Thermal and Immune Therapies." Advanced Drug Delivery Reviews, vol. 38, no. 5, June 2020, 10.1016/j.addr.2020.06.025. Accessed 1 Oct. 2024.

Stern, Stephan T., and Scott E. McNeil. "Nanotechnology Safety Concerns Revisited." Toxicological Sciences, vol. 101, no. 1, 1 Jan. 2008, pp. 4-21, academic.oup.com/toxsci/article/101/1/4/1655301, 10.1093/toxsci/kfm169. Accessed 7 Oct. 2024.

Segal, O., Novak, V., Azizi, Y., Kaplan, L., & Ben-Dov, I. Z. (2018). Quantitative assessment of peripheral nerves using magnetic resonance neurography: A study of the ulnar nerve in diabetic neuropathy. Journal of Neurophysiology, 120(1), 201-207.

Wolfe, Scott W. "Peripheral Nerve Injury and Repair." ResearchGate, Aug. 2000, www.researchgate.net/publication/12369987_Peripheral_Nerve_Injury_and_Repair. Accessed 5 Oct. 2024.

Design and Development of a Cellular Laminoplasty Plate

Saheed Ademuyiwa[1], Gillian Pearce[2] and Peter Zioupos[1]

1 Department of Engineering, University of Hull, Kingston upon Hull HU6 7RX, UK

2 Dr Gillian Pearce, College of Engineering and Physical Sciences, Aston University, Aston Triangle, Birmingham, B4 7ET, United Kingdom

ABSTRACT

Our research investigates the development and evaluation of cancellous-like laminoplasty plate designs, focusing on honeycomb structures with thicknesses of 0.4mm, 0.8mm, 1.0mm, and 1.2mm, as well as a solid design. Laminoplasty plates are essential in spinal surgery for stabilizing vertebrae and promoting bone healing. The study's objective was to evaluate the stiffness, strength, and flexibility of these designs under stress, which are crucial for both stability and adaptability within the spine's dynamic environment. Mechanical testing was conducted to determine the ultimate tensile strength (UTS) and flexibility of each design. The 0.4mm honeycomb design exhibited a UTS of 14.0±4.55 MPa and a strain of 0.131±0.0397 highlighting its strength but limited mechanical support in highly dynamic spinal environments. Although, the 0.8mm and 1.0mm honeycomb designs showed balanced stiffness and strength with UTS values of 12.57±3.58 MPa and 13.17±4.12 MPa, respectively, the 1.0mm design could withstand higher strains up to 0.156±0.0456 before failure, making it ideal for dynamic spinal regions where adaptability is crucial. The 1.2mm honeycomb design, despite its increased thickness, did not significantly outperform the 1.0mm design, indicating a potential limit to the benefits of increased thickness. The solid design, though less stiff than the honeycomb structure raised concerns about osteointegration and long-term bone healing. The results suggest that the 1.0mm honeycomb design offers the best balance between strength and flexibility, making it a promising candidate for laminoplasty applications.

Keywords: Laminoplasty Plate, Honeycomb Structure, Mechanical Properties, Spinal Surgery, 3D Printing, Design Optimization

INTRODUCTION

Laminectomy and laminoplasty are critical spinal surgeries aimed at relieving compression on the spinal cord or nerves due to conditions such as spinal stenosis, herniated discs or spinal tumours [2]. These procedures often involve removing or altering portions of the vertebral lamina to reduce pressure on the spinal cord thereby reducing neurological claudication, halting clinical deficits and promoting functional ambulation [3]. However, in some instances problems can arise involving destabilization of the spinal column, potentially leading to post-surgery complications [2,7]. Open laminectomies are the standard traditional treatment for relieving spinal cord or nerve root compression [5], while such procedures are effective, there may be limitations in terms of structural integrity because of the alterations in the biomechanics of the spinal column associated with the procedure [1]. Traditional metal implants are typically used to provide structural support, yet issues like stress shielding and poor osseointegration remain significant challenges potentially leading to poor long term surgical outcomes [6]. To ensure the stability and proper healing of the spine after these procedures, biomedical implants, such as plates, are often used to provide structural support and facilitate fusion. However, the challenge remains to develop spinal plates that offer both mechanical stability and flexibility to accommodate the dynamic nature of the spine while promoting osteointegration.

This paper focuses on the design and mechanical testing of cellular laminoplasty plates with a honeycomb structure that mimics the flexibility and load distribution of bone tissue. Through 3D printing, prototypes were fabricated and tested for their mechanical properties, including ultimate tensile strength (UTS), to evaluate their suitability for clinical applications. The primary aim is to enhance patient outcomes by providing a plate that balances strength, flexibility, and biocompatibility

MATERIALS & METHODS

Plate Design

The study's core focus is the design of cellular hexagonal honeycomb structures using SolidWorks. The aim was to mimic the natural cancellous bone structure to optimize flexibility and mechanical support while promoting biological integration. Five designs were tested: honeycomb structures with thicknesses of 0.4mm, 0.8mm, 1.0mm, 1.2mm, and a solid design. The geometric considerations were driven by ensuring anatomical fit and biomechanical performance. The figure 1 shows the laminectomy plate design using SolidWorks.

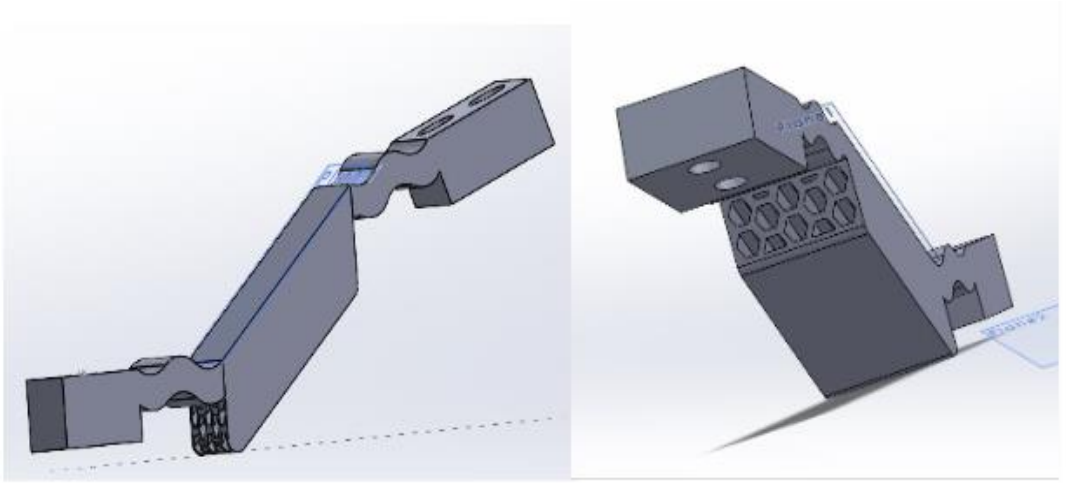

Figure1: The Laminectomy plate design using SolidWorks

3D Printing of Prototypes

The CAD-AM process allowed for the creation of complex geometries that would be difficult to achieve using traditional manufacturing methods. Multiple prototypes were printed for testing and comparison. Mechanical testing was conducted to evaluate the structural integrity of the plates in tension and compression and FEA was performed (SolidWorks) to make predictions. The aim was to determine the plate's capacity to withstand physiological loads while maintaining structural stability.

The prototypes were printed using PLA polymer with a density of 1.24g/cm^3 on an Ultimaker 2+ Extended printer. The 3D printing process was optimized to achieve a balance between mechanical integrity and lightweight design, utilizing a grid infill pattern at 20% density. The process settings, including a nozzle diameter of 0.4 mm and a printing temperature of 200^{0}C, were carefully selected to maintain precision during the fabrication of the intricate honeycomb designs.

Mechanical Testing

Mechanical testing was conducted using a Universal Testing Machine (EZ50) to determine the stiffness, UTS, and Young's modulus of each plate. Tensile tests were conducted to assess how the plates performed under simulated physiological loads. The aim was to compare experimental data with finite element simulations to ensure the designs met clinical standards for spinal implants.

Table1: The strain and the Ultimate tensile strength, UTS (MPa)

Honeycomb size (mm)	Ultimate Tensile Strength (MPa)	Strain
0.4	14.00 ± 4.55	0.131 ± 0.0397
0.8	12.57 ± 3.58	0.128 ± 0.0375
1.0	13.17 ± 4.12	0.156 ± 0.0456
1.2	12.30 ± 3.68	0.116 ± 0.0336
Solid	12.70 ± 3.58	0.163 ± 0.0474

RESULTS AND DISCUSSION

Experimental Findings

The tensile strength testing of various laminoplasty plate designs, including honeycomb structures (0.4mm, 0.8mm, 1.0mm, and 1.2mm) and a solid design, revealed distinct mechanical properties in terms of strength, and flexibility. The 0.4mm honeycomb design demonstrated the highest stiffness and load bearing capacity, with a UTS of 14.0±4.55 MPa and a strain of 0.131±0.0397, making it ideal for high-load applications with minimal deformation but limited flexibility as shown in figures 2 and 3. Although, the 0.8mm and 1.0mm honeycomb designs showed balanced stiffness and strength with UTS values of 12.57±3.58 MPa and 13.17±4.12 MPa, respectively, the 1.0mm plate, had a higher load bearing capacity, and demonstrated increased strain tolerance (up to 0.156±0.0456) making it adaptable for dynamic spinal regions. The solid plate had the highest strain at failure (0.163±0.0474), and it was more flexible than the rest, but may be prone to stress shielding.

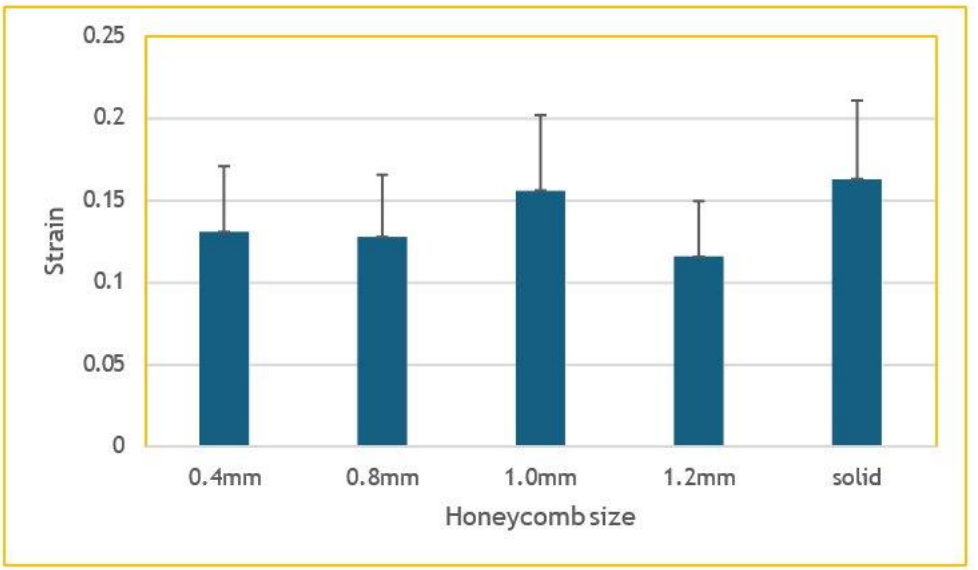

Figure 2: Bar Chat representative of the strain for the Honeycomb Designs

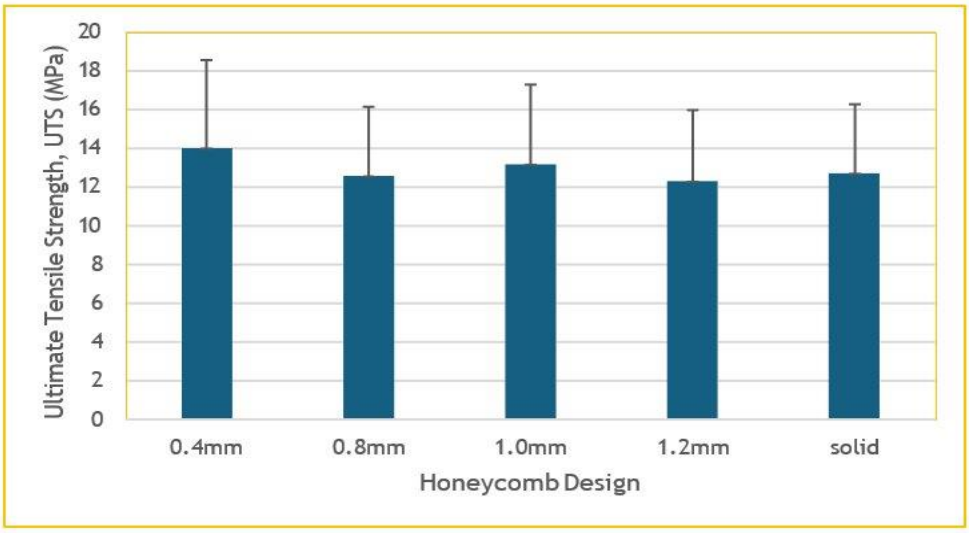

Figure 3: Bar Chat representative of the UTS for the Honeycomb Designs

Finite Element Analysis

Finite element analysis was performed to simulate the mechanical behaviour of the plates under realistic loading conditions. In figure 4, the simulations showed that stress distribution was optimized in the honeycomb designs, particularly in the case of 1.0mm plate, which closely matched the experimental results. The stress concentration was well within acceptable limits for clinical applications, reinforcing the suitability of the 1.0mm design

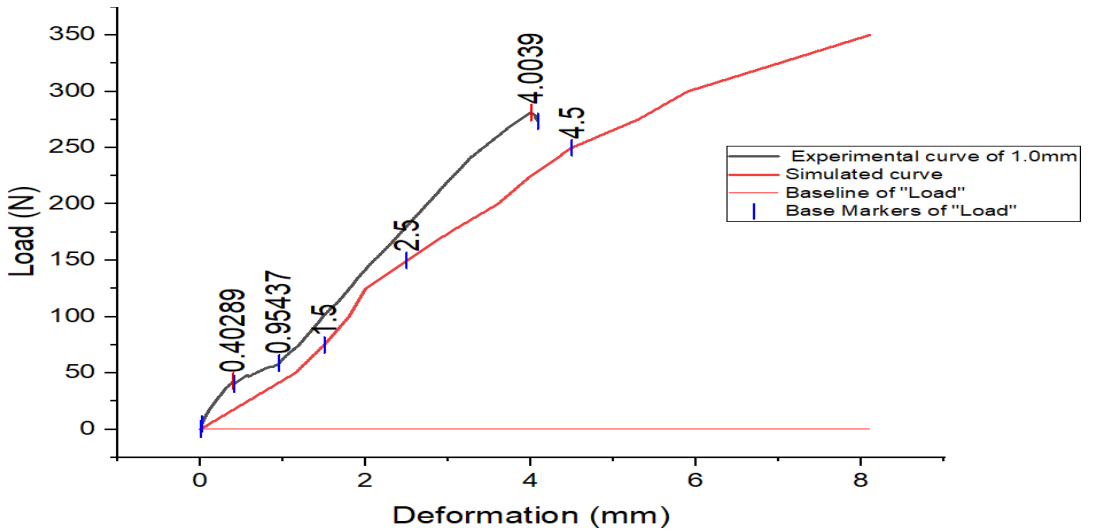

Figure 4: Simulated Load-Deformity curve for 1.0mm plate and Experimental curve

The study demonstrated that honeycomb structures offer distinct mechanical advantages over traditional solid plates. The 1.0mm honeycomb design struck the optimal balance between mechanical strength and flexibility, essential for use in spinal surgery where the implant must support biomechanical loads while adapting to movement. The design also showed potential for promoting osteointegration due to its porous nature. Figure 5 shows the commercial plate in-situ and the design of a custom-made cellular body 3D printed plate with a honeycomb cellular structure.

Figure 5: Commercial plate [4] in-situ and our design of a custom-made cellular body 3D printed plate with a honeycomb cellular structure.

While the study showed promising results for the 1.0mm design, further research is needed to explore its long-term biological performance, particularly in terms of bone growth and integration. Additionally, testing on a broader range of materials, including biocompatible metals and composites, could yield further improvements in the design's clinical viability.

CONCLUSIONS

Our research presents an approach to laminoplasty plate design by incorporating cellular honeycomb structures, which mimic the mechanical properties of natural bone. The results suggest that the 1.0mm honeycomb design offers the best combination of strength and flexibility, making it a strong candidate for future clinical application in spinal surgery. Further research will focus on long-term in-vivo testing and material enhancements to optimize osteointegration and mechanical performance.

REFERENCES

[1] Banczerowski, P., Czigléczki, G., Papp, Z., Veres, R., Rappaport, H.Z. and Vajda, J., 2014. Minimally invasive spine surgery: systematic review. Neurosurgical Review, 38(1), pp.11–26. doi: https://doi.org/10.1007/s10143-014-0565-3.

[2] Eisenstein, S.M., Balain, B. and Roberts, S., 2020. Current Treatment Options for Intervertebral Disc Pathologies. CARTILAGE, 11(2), pp.143–151. doi: https://doi.org/10.1177/1947603520907665.

[3] Estefan, M. and Camino Willhuber, G.O. (2021). Laminectomy. [online] PubMed. Available at: https://www.ncbi.nlm.nih.gov/books/NBK542274/.

[4] Globus Medical. (2024). *CANOPY® Laminoplasty System | Globus Medical*. [online] Available at: https://www.globusmedical.com/products/canopy/ [Accessed 21 Jul. 2024].

[5] Haddadi, K. and Ganjeh Qazvini, H.R., 2016. Outcome after Surgery of Lumbar Spinal Stenosis: A Randomized Comparison of Bilateral Laminotomy, Trumpet Laminectomy, and Conventional Laminectomy. Frontiers in Surgery, 3. doi: https://doi.org/10.3389/fsurg.2016.00019.

[6] Henky, J., Yasuda, M., Arifin, M.Z., Takayasu, M. and Faried, A., 2014. Trumpet laminectomy microdecompression for lumbal canal stenosis. Asian Spine Journal, 8(5), pp.667-74. doi: 10.4184/asj.2014.8.5.667. PMID: 25346821; PMCID: PMC4206818.

[7] Tarazi, J.M., Koutsogiannis, P., Humphrey, E.K., Khan, N.Z., Katsigiorgis, M., Katsigiorgis, G., & Cohn, R.M. (2024). Risk Factors for Unexpected Admission Following Lumbar Spine Laminectomy:

A National Database Study. *Cureus*, 16(3), e55507. doi: 10.7759/cureus.55507. PMID: 38571866; PMCID: PMC10990575.

Keynotes

Prof Jörg Fehr (University of Stuttgart)

"Active Human Models for the Assessment of Injury Patterns in Whiplash Trauma: Simulation and Experiment".

Prof Gianluca Tozzi (University of Greenwich)

"*Advances in imaging-based measurements and artificial intelligence for the characterisation of musculoskeletal tissues and biomaterials"*

Active Human Models for the Assessment of Injury Patterns in Whiplash Trauma – Simulation and Experiment

Jörg Fehr[1], Matthew Millard[1,2], Norman Stutzig[2], Alessandro Scattina[3] und Tobias Siebert[2]

[1] *Institute of Sport Science, University of Stuttgart, Allmandring 28, 70569 Stuttgart, Germany*
[2] *Institute of Sport Science, University of Stuttgart, Allmandring 28, 70569 Stuttgart, Germany*
[3] *Department of Mechanical and Aerospace Engineering (DIMEAS) Politecnico di Torino,*

Keywords*:* human body model, neck injury, rear impacts, driving simulator

1. Introduction

Autonomous driving alters occupant positions, like rotated seating, which changes musculoskeletal stresses during accidents and maneuvers. These positions and in-car multimedia and conference calls increase distractions and load variations during impacts, affecting injury risk. Specifically, a rotated head during a rear-end collision significantly raises whiplash risk, with chronic patients often found in such positions at impact time, altering muscle activation and neuromuscular response in accidents.

2. Methods

We use Finite Element Simulations of the head-neck region and experiments conducted in the FKFS driving simulator.

As a finite element (FE) model, we use the VIVA 50th percentile OpenHBM reduced head-neck model. The input boundary condition for the FE model is the T1 trajectory (X, Z and Yrot motion) extracted from [1].

To achieve a good fit with the experimental data [1], the boundary condition, the controller structure, and different muscle material models are examined. Two user-defined user materials, i.e., the EHTMM and the VEXAT, are compared with the standard LS-Dyna MAT 156 muscle material [2],

Furthermore, we look at how the pattern of injury on the macro and micro levels changes with increasing acceleration and how the pattern of injury changes with impact direction.

For the validation of the HBM, the neck movements and muscle activity of 21 participants (11 women) were recorded on the mechanical driving simulator of FKFS* in Stuttgart. The simulator performed maneuvers producing lateral accelerations of up to 5m/s². The recordings, EMG and kinematics data took place under two conditions: in one, participants looked forward (0°, 6 trials), and in the other, to the right (45°, 4 trials).

3. Results and Discussion

When considering active muscle reactions, it has been shown that classical Hill-type muscle models underestimate muscle forces during active lengthening – as occurs in rear-end collisions. A new VEXAT muscle model [2] is used to estimate muscle forces during active lengthening significantly more accurately.

As intuition would suggest, increased acceleration magnitude leads to increased head movement and IVD stress. Interestingly, the impact direction does not bring a specific pattern in increment or decrement in the IVD stress, suggesting that the risk of injury in the rotated configuration remains almost constant for the IVD.

Similar to a smaller earlier experimental study [3], we found that neck muscle activity responds to both direction and posture.

4. Conclusions

Low-speed rear-end impacts are frequently the cause of neck injuries, mainly connected to WAD that can lead to chronic pain. Since the mechanism of injury is not entirely known, HBMs are a powerful tool for injury assessment.

Acknowledgments

Thanks to the FKFS and the research group of Syn Schmitt for Modelling and Simulation of Biomechanical Systems (IMSB) for the successful collaboration. (DFG, German Research Foundation) under Germany's Excellence Strategy 3 (EXC 2075 – 390740016) through the Stuttgart Center for Simulation Science (SimTech).

References

[1] Ono K, Ejima S, Suzuki Y, Kaneoka K, Fukushima M, Ujihashi S. Prediction of Neck Injury Risk based on the Analysis of Localized Cervical Vertebral Motion of Human Volunteers During Low-speed Rear Impacts. In: Proceedings of the IRCOBI Conference. Madrid, Spain; 2006. .

[2] Millard M, Stutzig N, Fehr J, Siebert T. A benchmark of muscle models to length changes great and small. bioRxiv. 2024. Available from: https://-www.biorxiv.org/content/early/2024/07/26/-2024.07.26.605117.

[3] Kempter F, Lantella L, Stutzig N, Fehr J, Sieber T. Role of Rotated Head Postures on Volunteer Kinematics and Muscle Activity in Braking Scenarios Performed on a Driving Simulator. Annals of Biomedical Engineering. 2023;51(4):771-82. Available from: https://doi.org/10.1007/s10439-022-03087-9.

***Corresponding author: Joerg.Fehr@itm.uni-stuttgart.de**

Advances in imaging-based measurements and artificial intelligence for the characterisation of musculoskeletal tissues and biomaterials

Gianluca Tozzi[1*]

[1] *School of Engineering, University of Greenwich, United Kingdom*

Keywords*:* Musculoskeletal tissue, imaging, mechanics, artificial intelligence

1. Introduction

Musculoskeletal tissues are complex hierarchical structures, requiring constant technological advancement to capture and replicate their structure-function relationship at different dimensional scales. Experimental techniques such as digital volume correlation, mainly based on X-ray computed tomography (CT), greatly contributed to deepen understanding of local material deformation with investigations ranging from clinical CT to nanoCT [1]. Hyperspectral imaging (HSI) is an emerging multidimensional optical imaging method, which allows objective identification of tissues and conveys information from spectral bands beyond the capabilities of the human visual system or conventional cameras [2]. In addition, the advent of artificial intelligence (AI) proposed novel methodologies encompassing image classification and imaging-based mechanical predictions, which have the potential to revolutionise the characterisation of musculoskeletal tissues and biomaterials [3].

2. Recent advances

At the University of Greenwich, we are at the forefront of AI research for biomedical engineering. We recently developed unique models such as:

- Data-driven image mechanics (D^2IM) as shown in Figure 1, based on feed forward convolutional neural network, to predict deformation and risk of fracture in bone directly from grayscale content of microCT images [4].
- DiffSpectralNet which combines diffusion and transformer techniques to extract diverse and meaningful spectral–spatial features, leading to improvement in HSI classification [5].
- MedDiffHSI, which significantly improves classification of tumours, outperforming other advanced HSI classification methods [2].

3. Future directions

As more advancements in language models come to pass, more accessible and natural design interfaces can be made, including the ability to generate new data, run code, and develop multi-agent solutions [6]. Mechanics-focused large language models (LLMs) such as BioinspiredLLM were recently developed and trained based on a corpus of thousands of peer-reviewed articles in structural biological and bio-inspired materials, showcasing ability to generate new research hypotheses and connect disparate areas of knowledge domains [7]. These and other insights can yield powerful new opportunities for research at the intersection of experimental efforts and modelling, opening intriguing scenarios where a language model could map words to structures and generative models automatically investigate the mechanics of the desired materials.

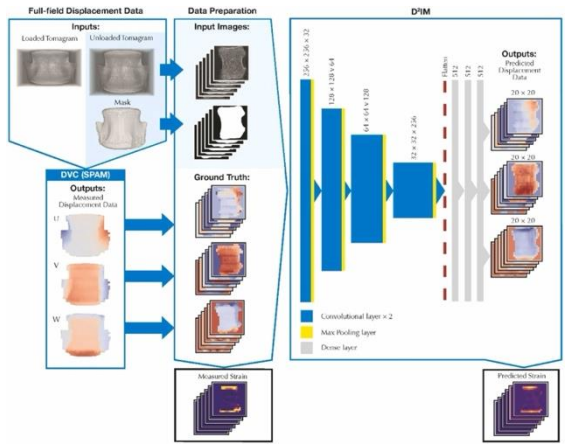

Figure 1: Workflow for generating 2D sliced dataset and making displacement field predictions using Machine Learning Model D^2IM. Strain fields are calculated from the displacements [4].

Acknowledgments

The author greatly acknowledges institutional support, funding agencies, colleagues and researchers that contributed to this work.

References

[1] Dall'Ara and Tozzi, 2022. Front. Bioeng. Biotechnol. https://doi.org/10.3389/fbioe.2022.1010056
[2] Sigger et al., 2024. J. Mic. https://doi.org/10.1111/jmi.13372
[3] Tozzi and Buehler, 2024. Comp. Mech. Mat. https://doi.org/10.1016/B978-0-323-90646-3.00046-0
[4] Soar et al., 2024. Ext. Mech. Lett. https://doi.org/10.1016/j.eml.2024.102202
[5] Sigger et al., 2024. Sci. Rep. https://doi.org/10.1038/s41598-024-58125-4
[6] Ni and Buehler, 2024. Ext. Mech. Lett. https://doi.org/10.1016/j.eml.2024.102131
[7] Luu and Buehler, 2024. Adv. Sci. https://doi.org/10.1002/advs.202306724

***Corresponding author: g.tozzi@greenwich.ac.uk**

Physics-based reinforcement for AI in Safety Critical Systems

V Shrinivas[1], C Bastien[1], H Davies[1], A Daneshkhah[2,5], J Hardwicke[3]
[1]*Institute for Future Transport and Cities, Coventry University, UK*
[2]*School of Computing, Electronics & Mathematics, Coventry University, Coventry, UK*
[3]*Institute of Applied and Translational Technologies in Surgery (IATTS), University Hospitals Coventry and Warwickshire NHS Trust (UHCW), UK*
[4]*School of Mechanical Engineering, University of Birmingham, UK*
[5]*Faculty of Mathematics and Data Science, Emirates Aviation University, Dubai, UAE*

Keywords*:* Physics-Based Reinforcement, Safety-Critical Systems, AI Prediction Verification, Biomechanical Injury Criteria, Safety Verification Framework

1. Introduction

AI predictions must be highly accurate and reliable in safety-critical systems like autonomous vehicles, medical devices, and aerospace technologies. Traditional machine learning models often struggle in scenarios with limited or noisy data. Physics-based reinforcement addresses this by integrating physical laws into AI models, enhancing accuracy and ensuring predictions align with real-world system behaviours, even when data is scarce or uncertain [1].

2. Methods

Physics-based reinforcement in AI prediction embeds physical laws into learning algorithms to ensure predictions align with real-world behaviours. However, this approach is complex and costly, especially for non-linear systems. An alternative is physics-based safety verification, which checks AI predictions against physical laws after training. By integrating biomechanical injury criteria as benchmarks, this method ensures accurate, risk-aligned predictions consistent with real-world injury thresholds [2].

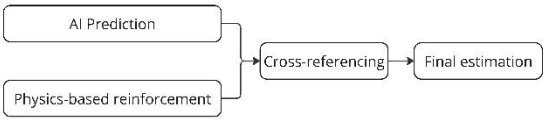

Figure 1: Physics-based reinforcement overview

3. Results and Discussion

The research on a physics-based safety verification framework for injury prediction systems showed significant improvements in prediction accuracy. By integrating this framework, the system effectively cross-referenced predictions with established injury criteria like Peak Virtual Power (PVP) limits, ensuring biomechanically feasible outputs that adhered to safety standards. Although the addition of physical verification increased complexity, the computational overhead remained manageable, enabling efficient real-time verification suitable for safety-critical environments [3].

4. Conclusions

This research highlights the effectiveness of a physics-based safety verification framework in enhancing the reliability and safety of injury prediction systems. By integrating biomechanical injury criteria into the verification process, the framework successfully improved prediction accuracy and ensured compliance with established safety standards. The results demonstrate that this approach reduces the occurrence of unsafe predictions and maintains robustness across diverse scenarios with minimal computational impact. These findings suggest that such a framework is a valuable tool for reinforcing the safety of AI-driven systems in safety-critical applications, such as autonomous vehicles and advanced driver assistance systems.

Acknowledgments

The authors thank University Hospitals Coventry and Warwickshire and Coventry University for sponsoring this research.

References

1. Thuerey, N., Holl, P., Mueller, M., Schnell, P., Trost, F., & Um, K. (2021). Physics-based Deep Learning. Retrieved from https://physicsbaseddeeplearning.org
2. Bastien, C., Sturgess, C. N., Davies, H., Wellings, R., Bonsor, J. & Cheng, X., 17 Aug 2024, In: Computer Methods in Biomechanics and Biomedical Engineering. 27, 11, p. 1563-1585 23 p., 240542684.
3. Arias Chao, M., Kulkarni, C., Goebel, K., & Fink, O. (2022). Fusing physics-based and deep learning models for prognostics. Reliability Engineering & System Safety, 217(107961), 107961. doi:10.1016/j.ress.2021.107961

*** Vadhiraj Shrinivas. Email: shrinivasv@coventry.ac.uk**

Assessing the Tribological Performance of Disposable and Reusable Sanitary Pads

A. Fadele Oluwaseyi[1] and S. Crossland [1(*)]

[1] *Medical Engineering, School of Engineering, University of Hull*

Keywords*:* tribology; friction; sanitary pads; reusable; disposable

1. Introduction

The comfort and user satisfaction of disposable and reusable sanitary pads is significantly impacted by their tribological performance. Limited research has been conducted into the effects of increasing saturation to varied sanitary pad materials in both the disposable and reusable markets on frictional response. In the push for sustainability the reusable market is also growing, requiring the evaluation of the impact of washing cycles on the friction measured. This study looks to utilise benchtop tribological assessment to evaluate the changes in friction coefficient of disposable and reusable sanitary pads under increasing saturation and the impact of washing cycle on the latter.

2. Methods

A HFRR tribometer (PCS Instruments Ltd) was used to perform benchtop frictional analysis. Loading characteristics were derived from seated pressure assessments (Yu et al., 2014) and shearing profiles explored in the representative field of incontinence product assessment (Morecroft et al., 2024), to replicate typical daily maximum loading profiles. A simplified contacting pin was created, due to complex anatomical geometry. 3D printed PLA was used as a standardised pin, with a mechanically equivalent skin representative 2mm coated Ecoflex 00-30 silicone pin as alternative. A range of differing sanitary products, Table 1, were evaluated. Saline was implemented as a commonly used menstrual blood substitute (DeLoughery et al., 2024) and all samples tested at 2ml increasing saturations between 0 – 10 ml. Five repeats were taken for the disposable products and three for the reusable due to limited supply of unwashed test product.

Product Type	Brand Name	Top Layer Composition
Disposable	FLO Organic Bamboo	Oeko-Tex Bamboo
Disposable	Rael	100% Cotton
Disposable	Natra-Care Ultra	Organic Cotton
Disposable	Lil-Lets Normal	Polyester-polyethylene blend
	Ultra Soft	
Disposable	Super Eco by Naty	100 % Organic cotton
Reusable	Femplete	Bamboo
Reusable	Eco Lily	Bamboo with charcoal
Reusable	MQUPIN	100% Organic cotton

Table 1 Profile of sanitary products evaluated.

Femplete reusable product was selected to feasibility test the effects of washing cycle on friction. The same saturation testing was performed on three repeats of three wash detergent cycles.

3. Results and Discussion

For both disposable and reusable products bamboo-based products maintain lower frictions during increasing salination than the cotton-based products. Increased friction was consistently seen in dry and wet contact of the silicon vs the PLA pin, due to potential adhesion from varied static and dynamic friction though these were not measured independently.

Friction decreased across wash cycles in the reusable washing feasibility test. Detergents and mechanical processes may alter the fibre properties.

4. Conclusions

Frictional response and comfort are interlinked. Ensuring that products maintain comfort during their usage lifetime is paramount due to the large population impact this has on quality of life.
Further work is needed to assess performance under temperature and humidity and increased number of wash cycles.

References

Yu, C.-H., et al. 2014. Development of a Modularized Seating System to Actively Manage Interface Pressure. Sensors, 14:14235-14252.

Morecroft, R., et al. 2024. Friction between human skin and incontinence pads in the presence of barrier protection products. IMechE Part H, 238(6): 644-654.

DeLoughery, E, et al. 2024. Red blood cell capacity of modern menstrual products: considerations for assessing heavy menstrual bleeding. BMJ Sex Reprod Health, 50:21-26.

***Corresponding author. Email: s.crossland@hull.ac.uk**

Viscoelastically active sutures to promote wound healing

Laughton, M.H.[1 (*)], Fancey, K.S.[1], France, L.A.[1]
[1] School of Engineering, University of Hull, United Kingdom

Keywords*:* sutures, viscoelasticity, wound healing, biomaterials

1. Introduction

Surgical sutures expedite wound closure and provide support during the healing process by reducing bleeding, averting infections, minimising scarring, and mechanically supporting and approximating tissues together. [1].

Synthetic polymeric materials dominate the suture market, with recent research focusing on additive improvements such as chemicals, coatings, drug-eluting, and stem cell-seeding sutures [2,3].

An alternative approach developed by France & Fancey [4] aimed to aid healing by influencing cellular behaviour by exploiting the viscoelastic properties of the polymeric sutures. This is believed to occur through the release of stored viscoelastic energy over time (weeks) by viscoelastically induced mechano-transduction and the release of electric charges, both of which are expected to stimulate wound healing.

2. Methods

Polypropylene (PP) and polyamide (nylon-PA) monofilament samples underwent material-specific thermo-mechanical treatments to induce creep [4].

Characterisation of suture samples before and after treatment was conducted using uniaxial tensile testing (UTT), differential scanning calorimetry (DSC), Fourier-transform infrared spectroscopy (FTIR), and scanning electron microscopy (SEM). Bespoke testing rigs measured viscoelastic recovery strain (VRS) and viscoelastic recovery force (VRF). Change in surface energies & hydrophobicity was examined by employing drop shape analysis and contact angle measurements (CA-DSA).

To examine the cellular response to treated sutures, a Phasefocus Livecyte system was utilised to perform quantitative phase imaging, capturing motility metrics every 20 minutes for 24 hours on samples of 2 cm length.

3. Results and Discussion

UTT found PP-treated sutures had an increased elastic modulus and decreased break strain, with tensile strength being maintained. PA sutures also indicated an initial decrease in break strain; however, no other significant changes were observed ($p>0.05$). DSC confirmed consistency in melting temperatures for both sutures ($p>0.05$). A ~10-20% increase in crystallinity was also detected for both, which was to be expected due to annealing.

FTIR showed no significant peak shifts, implying minimal impact on bond interactions. SEM revealed minor differences in surface features, which, with further optimisation, are likely to be resolved. VRS indicated both sutures had prolonged recovery, indicating the release of viscoelastic energy over the healing period. For treated sutures, a steadily increasing force was detected from VRF, stabilising after 100 hours to remain at ~2.3N and ~1.1N for PP and PA, respectively, in Figure 1.

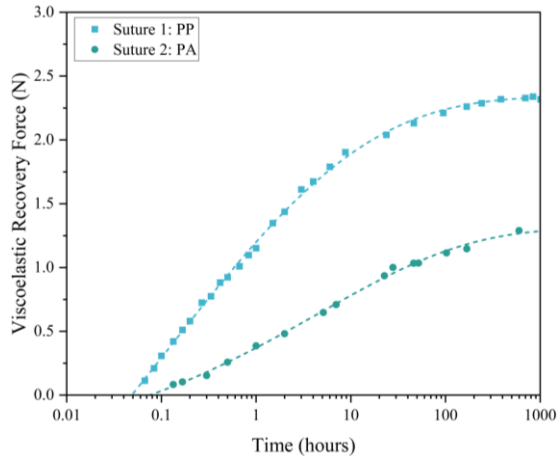

Fig.1. Viscoelastic recovery force generated over the wound healing period for PP and PA.

CA-DSA findings for both sutures implied a reduction in the hydrophobicity because of the treatment, which is speculated to be a result of the release of electric charges. Cell motility results indicated increased cellular response to the presence of treated samples for both materials.

4. Conclusions

Overall, viscoelastic sutures indicate consistent characteristics with untreated sutures while increasing cellular response, providing the pathway towards viscoelastically induced wound healing.

References

[1] Xu (et al.), Polymers (Basel) 14: 1637, 2022.
[2] Joseph (et al.), International Journal of Pharmaceutics 524: 454-466, 2017
[3] De la Harpe (et al.), Carbohydrate Polymers 266: 117860, 2021
[4] France, Fancey, Materials Science and Engineering: C 121: 111695, 2021

***Corresponding author: Michael Laughton, Email: m.h.laughton-2016@hull.ac.uk**

Development of a Test Platform Mechanically Representative of Human skin for Performance testing of Wound Healing Devices

C. Hill[1*], A. Dostan[1], C. Casey[2] and L. France[1]

[1] *School of Engineering, University of Hull*

[2] *Smith+Nephew PLC, UK*

Keywords*:* Multi-axis Sensor, Test Platform, Advanced Wound Care, Negative Pressure Wound Therapy

1. Introduction

FDA-approved testing platforms for Advanced Wound Care devices offer a basic understanding of device performance. These platforms, predominantly focus on user safety and device functionality, often neglecting the impact of biomechanical stimulation on enhancing wound healing. For instance, current approaches typically involve taking pressure measurements from a single point and testing on static, flat surfaces. Whilst animal and clinical testing can offer more comprehensive evaluations, these methods are constrained by ethical concerns and high costs, which limit their practical application. Also, they only produce qualitative data. This research introduces a test platform mechanically representative of a human lower limb for testing Negative Pressure Wound Therapy (NPWT) devices (Smith+Nephew PLC, UK). To enable analysis of lower limb dressing performance under physiologically relevant conditions, with quantitative performance data output.

2. Methods

The research began with standardised multi-axis mechanical testing of human skin and five different elastomers, to identify an elastomer that closely mimics skin properties. Based on these findings, a multi-axis elastomeric sensor was developed using the principles of high- and low-resistance mixtures as described by Matsuda [2]. The sensor consists of a silicone sheet embedded with a 6x6 array of porous silicone nodes, coated with a high-resistance composite material composed of polyvinylidene fluoride, dimethylformamide, and carbon black. Along the X and Y axes, a low-resistance conductive paste made from silicone, chloroform, and carbon black was applied. This was then attached to a representative knee model, capable of replicating the full range of movement of a human knee joint.

3. Results and Discussion

Changes in sensor resistance were measured to determine regions experiencing greater strain and pressure. This was measured with and without a NPWT dressing applied delivering approximately -80 mmHg of pressure along the Z-axis, as well as static and dynamic conditions.

During flat testing, resistance changes were confined to the Z-axis. In contrast, conformed and dynamic testing revealed resistance changes across all three axes. The findings suggest that the pressure applied by NPWT devices increases under conditions of increased static strain and dynamic movement, as illustrated in Figure 1, highlighting the need for advanced testing methodologies.

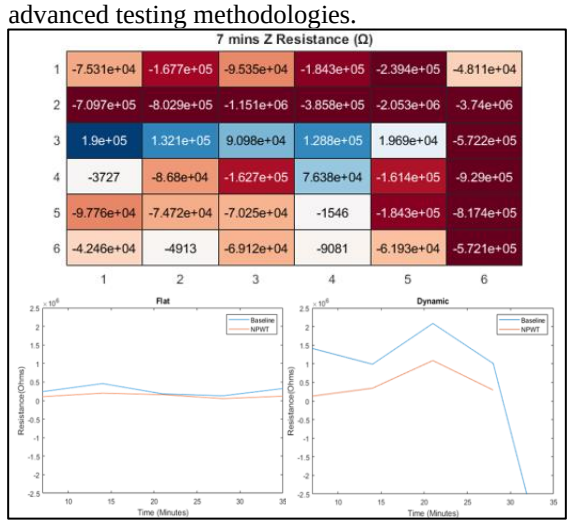

Figure 1 Array of Z-axis resistance measurements; graphs comparing Z-axis resistance baseline against NPWT and flat against dynamic conditions.

4. Conclusions

The standardised elastomer testing method produced Young's modulus values that aligned with those previously reported in the literature [3], confirming the accuracy of the approach. The elastomeric sensing array demonstrated independent detection of pressure and strain. This makes the sensor particularly effective at distinguishing between negative pressure generated by the NPWT dressing and higher pressures resulting from movement across the wound site.

Acknowledgments

We would like to thank Dr. Anthony Wilkinson for his help. This work was funded by Smith+Nephew.

References

1. FDA, Class II Special Controls Guidance Document: Non-powered Suction Apparatus Device Intended for NPWT, 2018.
2. Matsuda et al. Sci Rep 10, 12666, 2020.
3. Kalra & Lowe, J. Aging Sci 4: 156, 2016.

***Corresponding author. Email: c.a.hill-2015@hull.ac.uk**

AI and Mathematical Approaches for Predicting Tumour Progression

Dr. Amit K. Chattopadhyay, Dr. Gillian Pearce
Aimee Pascaline N. Unkundiye
Aston University, Aston Triangle, Birmingham B4 7ET, United Kingdom∗

Keywords: Tumour, predictive models ,magnetic nanoparticle; Fe_3O_4 , Treatment;

1. Introduction

In healthcare, AI models have shown transformative potential for addressing significant biological challenges such as cancer [1]. With over 18 million new cancer cases diagnosed in 2022 [2]and persistently high mortality rates, there is an urgent need for innovative approaches unlike traditional treatments like chemotherapy, radiotherapy, and immunotherapy which are often accompanied by severe side effects. To address these limitations, novel approaches are being explored, including the use of iron oxide magnetic nanoparticles (mNPs). mNPs present a promising alternative to conventional treatments due to their potential for targeted drug delivery [3], minimizing damage to healthy cells and reducing systemic toxicity [2].This study compares the efficacy of saline solution and mNPs in cancer treatment, using AI-driven models to predict tumour progression and shrinkage timelines. We employ machine learning algorithms and mathematical models to explore the potential of a treatment that is both effective and minimally invasive [2,4]. Through these AI models, we hope to provide insights into the dynamics and timeline of tumour shrinkage.

2. Methods

Data were acquired from multiple studies, involving MAC-16 tumour-bearing mice over durations of 5 and 30 days. Standardisation techniques ensured data uniformity. Machine learning algorithms such as Decision Trees (DT), Random Forests(RF), Multilinear Regression(MLR), and Adaptive Neural Networks(ANN) were applied for predictions. Mathematical models were employed to model tumour dynamics, providing insights into growth behaviours over time.

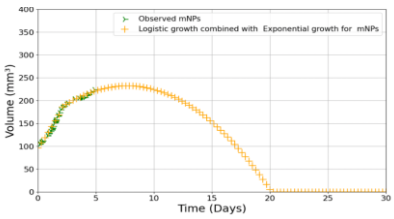

Figure 1 Tumour volume progression with mNP treatment

3. Results and Discussion

mNP treatments demonstrated substantial efficacy in tumour shrinkage compared to saline-treated and untreated groups, with significant destruction observed by day 20. The comparison between mNP and saline treatments (illustrated in Figure 1 and Figure 2) highlights the potency of mNPs in reducing tumour volumes.

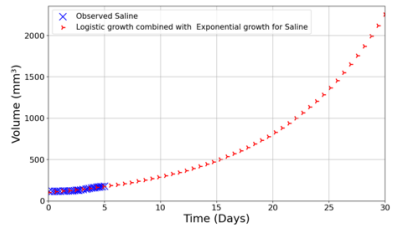

Figure 2 Tumour volume progression with Saline treatment

4. Conclusions

This study demonstrates the superior tumour-targeting efficacy of magnetic nanoparticles (mNPs AI models, particularly ANN, provide enhanced predictions for tumour dynamics). The results suggest that AI-driven models have broad applicability, with the flexibility to integrate different treatment forms when data is available. Moreover, this research highlights the potential of AI tools to reduce reliance on animal experimentation, thus lowering research costs and thus potentially accelerating the development of novel treatments. While these models may not fully replicate human biological responses, they have shown that nanoparticle-based therapies, especially when optimally coated, hold significant promise in reducing tumour volumes. This represents an important advancement in the search for more effective or personalized tumour treatments.

5. References

1. Clarke, M.A. and Fisher, J. (2020). Executable cancer models: successes and challenges. *Nature Reviews Cancer*, 20(6), pp.343–354. doi:https://doi.org/10.1038/s41568-020-0258-x.

2. Chattopadhyay, A.K., Pearce, G., N. Unkundiye, A.P. and Russell, S.T. (2024). Predicting the Progression of Cancerous Tumours in Mice: A Machine and Deep Learning Intuition. *Annals of Biostatistics & Biometric Applications*, [online] 6(2).

3. Akin, O., Aras, O., Watkins, A.J., Pearce, G., Medine, I., Kozgus Guldu, O., Tekin, V., Ting, R., Wong, J., Ma, X., Unak, P., (2018). An in-vivo pilot study into the effects of FDG-mNP in cancer in mice. *PLOS ONE*, 13(8), pp.e0202482–e0202482. doi:https://doi.org/10.1371/journal.pone.0202482.

4. Saranya A and Subhashini R (2023). A systematic review of Explainable Artificial Intelligence models and applications: Recent developments and future trends. *Decision Analytics Journal*, 7, pp.100230–100230. doi:https://doi.org/10.1016/j.dajour.2023.100230.

***Corresponding author. Email: aimeepascaline4@gmail.com**

Optimal merging of kinematic and kinetic information to determine the position of the whole body Center of Mass

Charlotte Le Mouel[1]

[1] *CNRS, Sorbonne Université, Paris, France*

Keywords*:* center of mass

1. Introduction

Stability analyses of standing and walking rely on accurate measurements of the position of the center of mass (CoM). Unfortunately, this cannot be directly measured. It is often estimated using markers on the body and kinematic models ranging from very simple (a single marker on the sacrum, as in Rankin et al., 2014) to very detailed (38 markers, as in Dumas et al., 2007). The accuracy of these models is however unknown. The aim of this study is: first, to evaluate the accuracy of state-of-the-art kinematic models of the CoM; and second, to improve this accuracy by combining kinematic and forceplate measurements.

2. Methods

Two subjects ran on a treadmill for one minute at 3 m/s and 4 m/s. The CoM position was caluclated for three kinematic models: the state-of-the-art model (38 markers), a simplified version (13 markers) and the hip mid-point. The CoM position was differentiated twice to obtain kinematic acceleration. The acceleration obtained from the forceplates was averaged across steps, corrected to remove drift, and integrated twice to obtain a reference CoM position.
A Kalman filter was adapted to optimally combine the kinematic CoM and the CoM acceleration obtained from forceplates..

3. Results and Discussion

During the flight phase of running, the acceleration of the CoM is equal to gravity. However, the acceleration of all three kinematic models was biased, with the largest error for the hip markers (38 % of gravity), then the simplified model (24 %) and the full model (14 %). The error in position was also largest for the hip markers (12.0 mm), then the simplified model (7.0 mm) and the full model (5.9 mm).
When using the proposed Kalman filter, the error in acceleration and position was drastically reduced to around 3 % for all kinematic models.

4. Conclusions

State-of-the-art kinematic models of the CoM were found to have very low accuracy. The proposed Kalman filter optimally combines kinematic and forceplate information to improve the accuracy of CoM measurements.
The code for calculating this optimal combination is available in both Python and Matlab at: https://github.com/charlotte-lemouel/center_of_mass
The documentation is available at: https://center-of-mass.readthedocs.io

References

Dumas R, Chèze L, Verriest J-P (2007) Adjustments to McConville et al. and Young et al. body segment inertial parameters. Journal of Biomechanics, 40, 543–553. https://doi.org/10.1016/j.jbiomech.2006.02.013

Rankin BL, Buffo SK, Dean JC (2014) A neuromechanical strategy for mediolateral foot placement in walking humans. Journal of Neurophysiology, 112, 374–383. https://doi.org/10.1152/jn.00138.2014

***Corresponding author. charlotte.lemouel@normale.fr**

Repositioning of computational Human full-body model of 95th Indian male

[1]Vaibhav Kulkarni, [1,2]Shailesh Ganpule.

[1]Department of Mechanical and Industrial Engineering, Indian Institute of Technology Roorkee, 247667, India,[2]Department of Design, Indian Institute of Technology Roorkee, 247667, India

Keywords*:* –Repositioning, Joint articulation, Mesh morphing, Human Body model (HBM).

1. Introduction:

Computational human body FE models have been usually developed in standardized postures like standing and seating postures. The computational full-body FE model often needs to be configured to numerous subject-specific postures such as reclined seating posture. Conventional simulation-based positioning method commonly used to reposition HBM possess a few limitations such as achieving simulation stability, occurrence of structural artefacts and degradation of mesh quality. In addition to this, these simulation-based methods are time-consuming. To obtain a variety of postures apart from conventional postures, it is imperative to develop robust human body positioning algorithms that allow joint articulation and repostioning of HBMs in alternative postures and expand the flexibility of human body models.

2. Methods

In present work, computer graphic-based repositioning methodology for joint articulation and repositioning of human body FE models elucidated . The computational full body FE model of 95th percentile male based on Indian anthropometric data has been developed by using medical imaging datasets i.e. CT and MRI scan data. In this method, ANSA HBM positioning tool package are utilized which facilitates real time efficient positioning of HBM to obtain anatomically accurate postures. The appropriate antomical planes and coordinate system defined and suitable kinematic markers or landmarks were specified to locate the positioning of joint and human organs. The kinematic joints were defined using suitable constraints on different locations of human organs.The revolute joint employed for knee,ankle,wrist joints whreas spherical joint were utilized for hip and shoulder joints.The repositioning procedure involves use of morphing techniques and appropriate constraints to control joint mobility to achieve several postures.

3. Results and Discussion

The joints provided desired mobility characteristics in terms of angular rotation and resulting flexion-extension, abduction-adduction posture and rotational movement posture obtained for nearly up to 40 degrees of motion..The repositioning methodology employs biofidelic movements of joints i.e. joint articulations for several joints such as the glenohumeral joint, humeroulnar joint, talocrural joint, tibiofemoral joint etc. were illustrated using the human body FE model and corresponding variation in postures was demonstrated. Additionally, kinematic joint modelling features enable realistic articulation and positioning of the human body, enhancing the efficient computational assessment of joint kinematics across different postures. This methodology fosters a compliant mesh morphing algorithm that maintains the mesh's overall quality before and after knee joint articulation. The different postures exported to different solvers and tools for further processing.

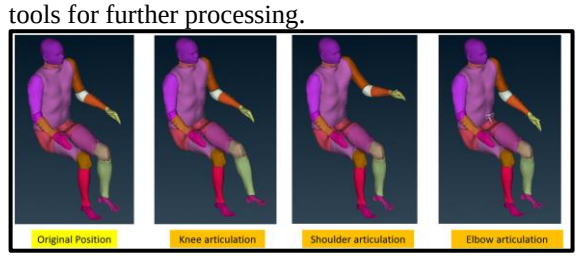

Figure 1 Joint articulation and repositioing of various human joints.

4. Conclusions

The cohesive integration of joint articulation and computer-graphics-based repositioning methods delineates a sturdy, effective, and user-friendly strategy simulating diverse anatomically accurate postures crucial to obtaining a variety of posture-specific models. This underscores its practical utility with minimal human intervention and time-saving features. This also eliminates the need to perform pre-simulation to position the model and smoothening techniques to refine mesh quality and structural artefacts. The model imparts advanced kinematic joint modelling features that effectively estimate joint kinematics and foster joint articulations.

Acknowledgments

The authors acknowledge BETA CAE Systems, India, for the provision of license and technical support for ANSA software distributed to IIT Roorkee.

References

1.BETA CAE Systems , ANSA User Manual 2023.

***corresponding author. Kulkarni.me@sric.iitr.ac.in;**

Ground reaction forces and kinematics of sprinting using wearable systems

Batbayar Khuyagbaatar[1], Munkhbat Tumurbaatar[1], Boldbaatar Chuluunbaatar[2] and Battsengel Banzragch[2]

[1] *Biomechanical Research Laboratory, Mongolian University of Science and Technology, Ulaanbaatar, Mongolia*

[2] *Sports Medicine and Research Center, Ulaanbaatar, Mongolia*

Keywords*:* kinetics; kinematics; sprint; wearable sensors

1. Introduction

Sprinting kinematics have been broadly investigated. The joint kinematics were shown to be associated with maximal sprint running, which is typically divied into accelaration, maximal velocity, and deacceleration phases [1], [2]. Many studies have investigated biomechanical factors in the sprinting phases using conventional motion capture systems, but few have utilized wearable systems. This study aimed to investigate kinematic and kinetic variables during sprint acceleration using wearable motion capture systems.

2. Methods

10 youth male sprinters performed three sets of 30 m sprints on an indoor track. Whole-body kinematics and ground reaction forces (GRF) were recorded using Xsens MVN and F-Scan research wearable systems at a sampling rate of 60 Hz. Kinematics and GRF data were visually synchronized from first heel contact to fifth heel contact, where a 50 N threshold value in GRF was used to define contact with the track [2].Joint kinematics, velocity of the center of mass (COM), and GRF in the front leg for the first four steps after clearing blocks were analyzed.

3. Results and Discussion

The vertical GRF, leg joint flexion angles, and COM velocity are shown in Fig 1. The mean of peak GRFs was 309.4±41.2% of body weight (BW). Estimated ground reaction forces (GRFs) were similar to those reported in studies, where it was shown that GRFs were around 3 times the BW [3]. The COM velocity was increased from 4.1±0.3 m/s to 6.4±0.4 m/s during the first four steps (Fig 1). While flexion angles of the hip, knee, and ankles at peak GRF were slightly decreased as a move forward due to the body becoming more upright posture.

4. Conclusions

This study investigated the kinematics and GRF during sprint acceleration using wearable systems, such as inertial measurement and insole pressure sensors. The mean of the GRF and velocity were increased as moved forward, while leg kinematics were slightly decreased at the peak GRF. Future studies will investigate the relationship between GRF and whole-body kinematics during both foot support and swing phases.

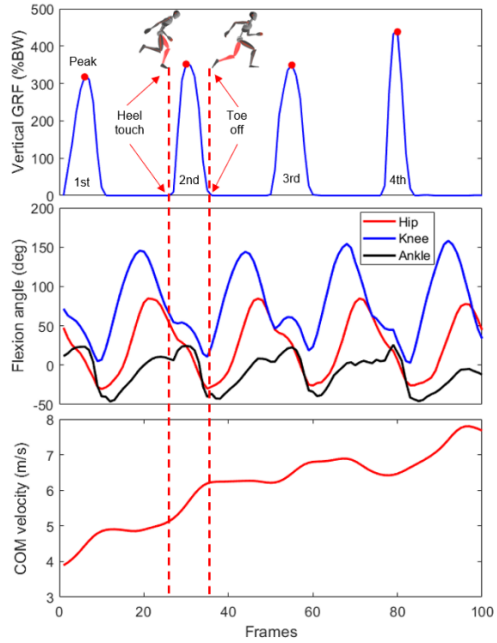

Figure 1. GRF and kinematics during the first four steps (Case of one sprinter).

Acknowledgments

This work was supported by the Sports Medicine and Research Center of Mongolia (G/23-08) and the "Mongolia-Japan Engineering Education Development" project (J24C16), Mongolia.

References

[1] K. Miyashiro et al. Kinematics of maximal speed sprinting with different running speed, leg length, and step characteristics, *Front. Sports Act. Living*, 1, 37, 2019.

[2] D. King, L et al. Relationships between kinematic characteristics and ratio of forces during initial sprint acceleration, *J. Sports Sci.* 40, 22, 2524–2532, 2022.

[3] R. Nagahara et al. Sensor insole for measuring temporal variables and vertical force during sprinting, *Proc. Inst. Mech. Eng. Pt. P J. Sports Eng. Tech.* 232, 4, 369–374, 2018.

***Corresponding author: batbayarkh@must.edu.mn**

Analysis of the influence of the velocity on the injury mechanisms, typology and severity in car accidents

M. Dorsemaine[1,2(*)], D. Brizard[2], M. Massenzio[2], T. Serre[3], C. Vernet[4] and C. Bruna-Rosso[1]

[1] *Aix Marseille Univ, Univ Gustave Eiffel, LBA, Marseille, France*
[2] *Univ Lyon, Univ Gustave Eiffel, Univ Claude Bernard Lyon 1, LBMC, UMR_T 9406, F-69622 Lyon, France*
[3] *Laboratoire Mécanismes d'Accident, Gustave Eiffel Univ., Salon de Provence, France*
[4] *Unité Mixte de Rercherche Epidémiologique et de Surveillance Transports, Travail, Environnement, University Gustave Eiffel, University Claude Bernard Lyon 1, Bron, France*

Keywords*:* speed; accident; injury; car; FE simulations

1. Introduction

The speed limit on road is often an issue regarding road safety, with recently in France the reduction of the speed limit from 90 km/h to 80 km/h on non-urban roads. Several studies used speed characteristics (impact velocity, delta-V) to predict injury risks using Event Data Recorder included in accidented cars (Doecke et al., 2020; Weaver et al., 2015). Despite these epidemiological studies, the effect of the velocity on the injury mechanisms remains insufficiently quantified. Thus, the VISTA project aimed at (i) investigating the impact velocity in specific reconstructed accidents and (ii) quantifying the influence of the impact velocity on the injury mechanisms and injury severity using numerical simulations.

2. Methods

The French national police database related to traffic accidents (BAAC) was analysed between 2012 and 2022 to identify the car accident scenarios leading to the most severe injuries. Three specific accidents matching these scenarios were then isolated from a database of detailed accident reports to investigate the effect of breaking assistance devices (FWC, AEB) on the impact speed for different reaction times of the driver and detection ranges.

In the second part of this project, finite element simulations of a frontal car crash with a rigid obstacle were conducted with a Dodge Neon model. A full factorial design of experiments of 40 accident configurations was performed for 4 impact velocities (30, 50, 70 and 90 km/h) and 10 obstacle types, positions and orientations. The influence of the impact velocity on the loading measured under the car seats of the vehicle was analysed along with the compressions of the different parts of the vehicle.

3. Results and Discussion

The analysis of the BAAC database highlighted that severe accidents more frequently occurred in non-urban and non-intersection areas, on all types of roads but were mostly frontal or lateral accidents.

The analysis on the breaking assistance devices showed a potential strong reduction of the impact velocity (from 48.5 km/h to 0 km/h) but was strongly influenced by the detection range and the reaction time of the driver.

The preliminary results of the numerical analysis showed, as expected, a strong influence of the impact velocity on the compression of the vehicle and on the velocities measured under the car seats. In the future, an in-depth analysis of the results will be conducted before using the loading of the car seats as input on a cabin model with a human model to investigate the injury risks for such accident conditions.

4. Conclusions

This study constitutes the first parts of the VISTA project that will help better quantify the influence of the velocity on the injury mechanisms during car crashes. Future steps will focus on the evaluation and evolution of thoracic injury criteria to improve the injury risk evaluation. All these results will then be used to improve the patient care after a car accident.

Acknowledgments

We would like to thank Clément Soubeyrand, Komi Djossou, Maxime Llari, Michel Behr and Pierre-Jean Arnoux for their contribution to this project.

References

Doecke S.D., Baldock M.R.J., Kloden C.N., Dutschke J.K., 2020, Impact speed and the risk of serious injury in vehicle crashes. Accident Analysis and Prevention, 144: 105629

Weaver A.A., Talton J.W., Barnard R.T. et al., 2015, Estimated Injury Risk for Specific Injuries and Body Regions in Frontal Motor Vehicle Crashes. Traffic Injury Prevention, 16(1): S108-S116

***Corresponding author. Email: marine.dorsemaine@univ-eiffel.fr**

Assessing Occupant Safety in Automated Driving Scenarios

Alexander Diederich[1], Christophe Bastien[1*] and Michael Blundell[1]

[1] *Centre for Future Transport and Cities, Coventry University, CV1 5FB.*

Keywords*:* Connected Autonomous Vehicle, CAV safety, Machine Learning, Kinematics, Madymo, AHBM

1. Introduction

The purpose of this study is to investigate a method to extract which rotated seating configurations are dangerous in Connected Autonomous Vehicles (CAV) when subjected in extreme braking followed by a frontal impact.

2. Methods

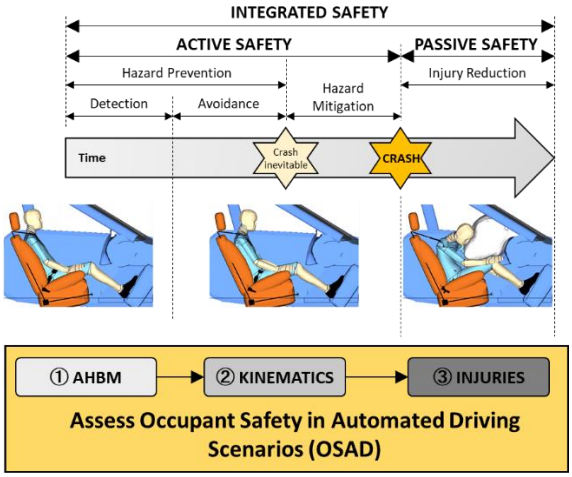

Fig.1. Presentation of the framework to extract occupant injuries.

A framework is designed with combination three distinct phases (**Fig 1.**). The first one is the validation of an active human computer model against human tests to ensure that the occupant's kinematics are realistic. Following this, a process to extract the occupant's head kinematics in designed using machine learning (ML). In case of extreme braking, in any rotated seating scenario, this process will capture any contact with the vehicle hard trims, occupants-to-occupants and closeness to potential deploying airbags. The final stage is to combine the occupant's kinematics from the pre-braking phase with frontal crash. This phase will use machine learning techniques to compute a probability of injury severity based on head, neck and chest injuries and provide the dangerous seating positions

3. Results and Discussion

Using ML it is possible to design a vehicle interior ensuring that head contacts are mitigated. The head save zone is plotted and represent the head motion as a function of seat back angle (**Fig 2.**).

Scenarios with injury severities (**Fig 3.**) during extreme braking follower by a frontal crash which are higher than when the vehicle is designed (Blue dot) can be extracted and dangerous seating positions be known to the driver. Eventually, these seating positions can be disabled by the vehicle.

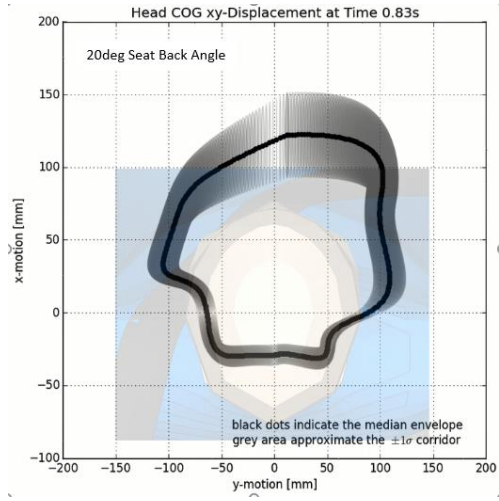

Fig. 2. Plot of safe head zone when vehicle is subjected to extreme braking

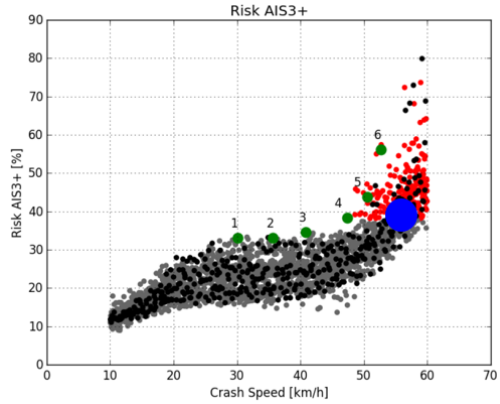

Fig. 3. Rotated seating scenarios exceeding standard crash test

4. Conclusions

The proposed method is providing new opportunities to design safer CAV.

References

[1] Diederich, A., Bastien, C., & Blundell, M. (2023). The Prediction of Autonomous Vehicle Occupants' Pre-Crash Motion during Emergency Braking Scenarios. Proceedings of the Institution of Mechanical Engineers, Part D: Journal of Automobile Engineering, 237(14), 3304-3312. https://doi.org/10.1177/09544070231153262

[2] FDiederich, A., Bastien, C., Ekambaram, K., & Wilson, A. (2021). Occupant Pre-Crash Kinematics in Rotated Seat Arrangements. Proceedings of the Institution of Mechanical Engineers, Part D: Journal of Automobile Engineering, 235(10-11), 2818-2842. https://doi.org/10.1177/09544070211004504

***Corresponding author. aa3425@coventry.ac.uk**

Modelling of a seated human body model for occupant ride comfort

Raj Desai

[1] *Centre for Future Transport and Cities, Coventry University, UK*

Keywords*:* Human body, modelling, vibration, comfort.

1. Introduction

Occupant comfort is a crucial factor in vehicle preference and consumer satisfaction, influencing overall driving experience and brand loyalty. To enhance this comfort, it is essential to accurately model the vibrations transmitted through the human body. These models not only help predict the likelihood of motion sickness but also play a vital role in assessing long-term health impacts caused by prolonged exposure to vibrations. Moreover, as the automotive industry moves towards automated vehicles, such models become increasingly important for optimizing ride quality, ensuring that future vehicles provide a smooth, comfortable, and health-conscious travel experience. By integrating these models into vehicle design and development, manufacturers can address a wide range of comfort-related issues, ultimately leading to higher consumer satisfaction and safer, enjoyable journeys.

2. Methods

A 12 DoF multibody biomechanical model of the human body, joint configuration, backrest support is depicted in Fig. 1. The model consists of four rigid masses 1-4 representing the anatomy of thigh-pelvis, lower torso, upper torso and head, respectively. The novel joints *J*i (3-DoF) comprises of rotational and translational spring-damper that allows relative motion between body parts. Equations of motion were derived using free body diagram analysis and the Newtonian method. The time-domain functions were then converted to the frequency domain using Laplace transforms.

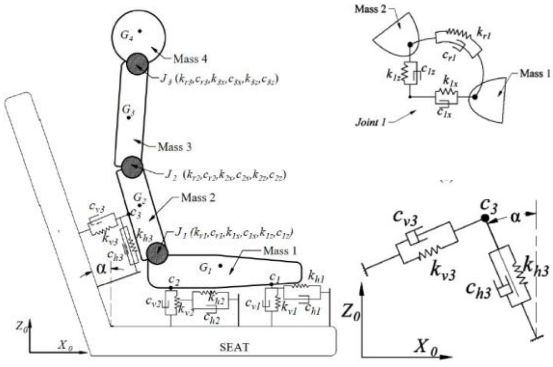

Figure 1 12 Dof human body model.

3. Results and Discussion

Optimization techniques were applied to refine the algorithm. The model was thoroughly validated against experimental data, specifically focusing on head direct and cross-axis seat-to-head transmissibility. This validation process ensured that the model's predictions align with observed data, as illustrated in Fig. 2. The successful comparison confirms the model's accuracy and reliability, demonstrating its effectiveness in capturing real-world seat-to-head vibration dynamics.

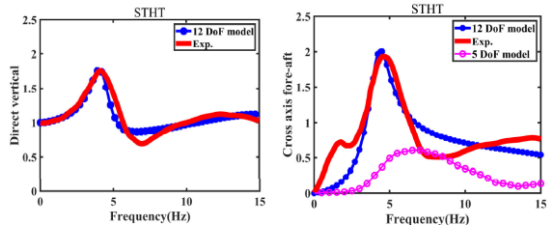

Figure 2 Model Validation.

4. Conclusions

This work presents a detailed 2D, 12-degree-of-freedom (DoF) multibody biomechanical model of the human body in a seated posture with an inclined backrest. The model parameters were optimized using a genetic algorithm and global criterion-based minimization to closely match experimentally observed head movements. The model serves as a valuable tool for studying the impact of different seating conditions and vibration environments on occupant comfort and health, with potential applications in the design of seating systems, particularly in the automotive and aerospace industries. Future enhancements could include expanding the model to 3D dynamics and integrating it with vehicle simulations to further optimize ride comfort, especially for automated vehicles.

References

Kim, E., Fard, M., & Kato, K. 2020. A seated human model for predicting the coupled human-seat transmissibility exposed to fore-aft whole-body vibration. *Applied Ergonomics*, 84, 102929.

Desai, R., Guha, A., & Seshu, P. 2021. Modelling and simulation of an integrated human-vehicle system with non-linear cushion contact force. *Simulation Modelling Practice and Theory, 106*, 102206.

***Corresponding author. Email: ae4514@coventry.ac.uk**

Initial Evaluation of Underrepresented Occupants in Highly Autonomous Vehicles using VIVA+ Human Body Model

A.Harrison[1]

[1] *Deutsches Zentrum fuer Luft- und Raumfahrt, Institut fuer Fahrzeugkonzepte, Pfaffenwaldring 38-40, 70569, Stuttgart, Germany*

Keywords*:* Occupant Safety; Autonomous Vehicle; Restraint System; Human Body Model; Injury

1. Introduction

To facilitate the development and employment of Highly Autonomous Vehicles (HAVs) to the road, there is an obligation to enhance occupant safety of all HAV-users. The unique challenges to safety systems are compounded by the greater user variety and seating configurations presented by HAVs. Therefore, as part of the EU project Aware2All, a preliminary investigation was conducted of state-of-the-art (SoA) and novel seat-integrated seatbelt configurations and their efficacy of reducing injury risk of underrepresented occupants via Finite Element Sled-test simulations were evaluated, using open-source models. The 50th percentile female was represented by the Human Body Model (HBM) VIVA+50F (50F) [1]. Additionally, the VIVA+50F was adapted to represent a 50th percentile female occupant with loss of a limb (50DF). The posture of the occupants was defined by seating measurement data of DLR's Urban Modular Vehicle People Mover (UMV PM) prototype vehicle with a full-frontal sled-pulse [2].

2. Methods

A 3-stage positioning strategy was established for rapid positioning and posture definition. This was a combination of pre-processor articulation to describe the posture and two-stage analysis to efficiently position the occupant in the seat (employing partially rigid-model to reduce computational demand) and transient analysis for contact convergence for realistic flesh and seat foam deformation. Assessments were conducted with varying seatbelt definitions, forming a test matrix of 7 studies that allowed performance evaluation of different restraint-system definitions for 50F and 50DF occupants. These consisted of a standard passenger 3-point seat-belt system, an advanced 3-point seatbelt system and a 4-point seatbelt with advanced pre-tensioners and retractors. The energy balance of each contact surface was evaluated as well as the macro-level injury risks sustained by the occupant. In addition, a qualitative assessment of the occupant was conducted to better understand the implications of an unsatisfactory restraint system control, in particular, between the 50DF and standard 50F female occupant. Lastly, a reclined seatback of 45° was assessed for viability of utilising the VIVA+ 50F and to provide an outlook for future restraint-system development.

3. Results and Discussion

It was found that for the same advanced 3-point seatbelt, the 50DF had increased risk of injury in multiple criteria in comparison to 50F, namely, BrIC (18%), rib fracture (28%) and 3+ rib fractures (11%). In each case without a foot support, the occupant suffered a 67% (±6%) increased likelihood of Proximal Femur fracture (PFf). It was noted that the PFf risk is independent of the disability or belt-system parameters. However, an observable difference between the left and right PFf risk (11%) is witnessed due to the position of the belt anchorage locations. Shoulder belt slippage is apparent in 50DF test-case with a 3-point harness resulting in poor restraint performance.

4. Conclusions

The limited load-path distribution permits greater occupant excursion, inducing increased torso and pelvic loading to the occupant. The injury risk of a physically disabled occupant is higher than that of a non-disabled counterpart with a greater risk of seatbelt slippage due to torso rotation. Advanced belt-systems show promise to mitigate abdominal and torso injuries.

Acknowledgments

The work conducted is funded under European Union's Horizon Europe research and innovation programme under grant agreement number 101076868.

References

John, J.; Klug, C.; Kranjec, M.; Svenning, E.; Iraeus, J., 2022, Hello, world! VIVA+: A human body model lineup to evaluate sex-differences in crash protection. Frontiers in Bioengineering and Biotechnology, Vol. 10, 19-07-2022. DOI: 10.3389/fbioe.2022.918904

Höschele, P.; Smit, S.; Tomasch, E.; Östling, M.; Mroz, K.; Klug, C., 2022, Generic Crash Pulses Representing Future Accident Scenarios of Highly Automated Vehicles. SAE International Journal of Transportation Safety, Vol. 10, No. 2, pp. 09–10–02–0010

***Corresponding author. Email: Andrew.Harrison@dlr.de**

Instrumentation of Finite Element Human Body Models for Simulating Tram-Pedestrian Collision Scenarios

O. Erian [1,2], M. Behr[1], P-J. Arnoux[1], W. Wei[1], E. Lequiniou[2], F. E. A. Njilie[2]

[1] *Laboratoire de Biomécanique Appliquée, Université Gustave Eiffel, Marseille, France*

[2] *Altair Engineering France, Antony, France*

Keywords*:* Tram-pedestrian accidents; Finite Element Human Body Model (FEHBM); Injury biomechanics; Collision dynamics; Pedestrian safety.

1. Introduction

The global expansion of tram networks has increased pedestrian collision risks (Lackner et al., 2022). Although the CEN/TR 17420:2020(E) standard improved tram safety, recent post-COVID data shows a rise in fatalities, underscoring the need to study injury mechanisms in tram-pedestrian collisions. Finite Element Human Body Models (FEHBMs) offer insights into injury biomechanics but require well-defined impact scenarios. This study analyzes tram-pedestrian accidents to inform FEHBM simulations and enhance pedestrian safety.

2. Methods

Tram-pedestrian accident data from the French National Road Traffic Accident Database (2005–2022), injury severity data from the Rhône registry (2001–2020), and tram velocity measurements from Marseille were analyzed. This provided insights into victim demographics, injury severity, and tram velocity variations, identifying the most frequent and severe collision scenarios.

Based on these findings, the THUMS AM50 Version 4.02 50th percentile adult male model was selected and implemented in the OpenRadioss solver. This model was chosen due to its anthropometric similarity to typical adult victims. Injury data guided sensor placement in critical regions (head, thorax, lower extremities) to capture relevant injury mechanisms during simulations.

Model validation involved recreating published experimental studies using post-mortem human subjects (PMHS) and anthropomorphic test devices (ATDs), focusing on body regions frequently injured in tram collisions. This confirmed that the model accurately simulates injury mechanisms in these regions.

3. Results and Discussion

The data showed that 72.2% of victims were adults, with older adults (35.8%) most affected. Fatalities were mostly among older females (60.6%), followed by adolescents (22.1%) and young adults (20.8%). Upper extremities (20.2%), head (19.9%), and lower extremities (17.1%) were the most frequently injured regions, while thoracic injuries, though less frequent (9.5%), accounted for 34.5% of severe cases (MAIS 3+), and head injuries contributed to 36.4% of severe cases.

These findings guided the selection of the THUMS AM50 model, aligning with the typical demographic of accident victims. Sensor placement in key injury regions enabled the simulation of injury mechanisms. Preliminary validation shows the model's ability to replicate injury patterns, with further refinements planned for tram-specific collision scenarios.

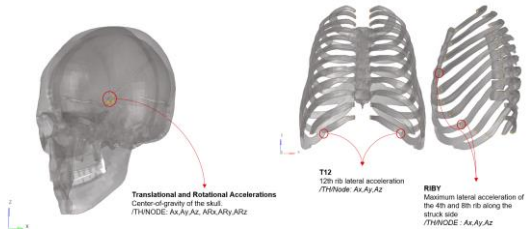

Figure 1: Sensor placement for most severely injured body regions

4. Conclusions

Key patterns in tram-pedestrian accidents were identified, informing the selection of the THUMS AM50 FEHBM. Preliminary validation confirmed the model's suitability for simulating critical injury regions. Future work will refine the model's predictive capabilities through further validation and tram-specific scenario simulations, contributing to improved pedestrian safety.

References

Lackner, C., Heinzl, P., Rizzi, M. C., Leo, C., Schachner, M., Pokorny, P., Klager, P., Buetzer, D., Elvik, R., Linder, A., & Klug, C. (2022). Tram to Pedestrian Collisions—Priorities and Potentials. Frontiers in Future Transportation, 3, 913887.

***Corresponding author. Email: oktobia.erian@univ-eiffel.fr**

Development of a Wearable Head Impact Monitoring Device for Bikers

Alaa Aldin Ghazal [1(*)] and S. G. Ganpule[1]

[1] *Department of Mechanical and Industrial Engineering, Indian Institute of Technology Roorkee, Roorkee, India*

Keywords*:* Concussion detection; Wearable device; Head impact monitoring; Real-time system; Healthcare

1. Introduction

Mild Traumatic Brain Injury (mTBI) resulting from head impacts with another object in a direct or indirect way, even when a person wears a helmet to protect his head from the direct impact, it cannot help in reducing the head kinematics which affects directly on the brain cells causing mTBI. After an accident, individuals may not immediately exhibit mTBI symptoms, leading them to underestimate their injury. This is particularly common among bikers involved in minor accidents. In the current era, where timely healthcare interventions can significantly reduce long-term consequences, there is a need for a wearable system that can instantly detect head impact severity and trigger automatic alerts to healthcare authorities. This study presents a low-cost, wearable head impact monitoring device designed for bikers' helmets. The system incorporates a high-g linear accelerometer (H3LIS331DL), a 9-axis Inertial Measurement Unit (MPU9250), and a GPS module (NEO-6M) for real-time geolocation monitoring, connected with an IoT development board (Wemos D1 Mini-based ESP8266), the device records the impact data whenever it is above specific threshold and sends alerts via WhatsApp and email containing the head kinematics data as attachment, allowing the authorities to know the location of the accident and helping doctors diagnose mTBI as early as possible using the recorded data.

2. Methods

The device should be attached to the helmet and connected to the internet using a Mobile Wi-Fi hotspot. When an impact force is applied to the helmet, it will send an alert notification to a mobile phone as a WhatsApp message alert text, and geolocation link of the person, in real-time. Simultaneously, it will send an Email with the geolocation link and the sensors data as an attachment, ensuring immediate and comprehensive reporting.

The system captures head kinematics, including linear acceleration and angular velocity, storing the data locally on an SD card and transmitting it via email and WhatsApp for rapid intervention. Validation was done using a linear impactor on a head surrogate, with the device demonstrating reliable impact detection compared to reference sensors. Figure 1 shows the hardware components.

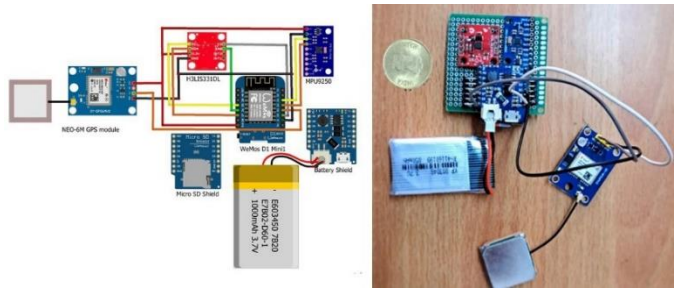

(a) (b)

Fig 1. Hardware Components and their Connections (a) connection diagram (b) Photo

3. Results and Discussion

The device was tested by applying sudden impact tests with the linear impactor, and the results confirmed that the system accurately recorded the linear and angular accelerations and sent the notification and data in real-time. In the calibration process, the peak values slightly varied from the reference sensors due to the limited specifications of the low-cost sensors. However, the device reliably triggered alerts and provided the required information.

4. Conclusions

A wearable system for bikers' helmets was designed and validated using a pneumatic linear impactor and calibrated using reference sensors on a head surrogate. It showed reliable performance in detecting and transmitting head kinematics in addition to the accident geolocation, which accelerates the process of finding the accident location and the diagnosis of the mTBI, the device is well-suited for public use, and offers a significant step towards proactive injury management, ensuring that individuals who might dismiss head trauma are promptly assessed by healthcare services.

References

O'Connor KL, Rowson S, Duma SM, Broglio SP. Head-Impact-Measurement Devices: A Systematic Review. J Athl Train. 2017 Mar;52(3):206-227. doi: 10.4085/1062-6050.52.2.05. PMID: 28387553; PMCID: PMC5384819

***Corresponding author. Email:** Alaa_ag@me.iitr.ac.in

Numerical reconstruction of a mountain biking 'over-the-bars' fall

S. Bonte[1,2], A. Thouzé [2], P-J. Arnoux[1], L. Thollon[1], W.Wei[1] & N. Bailly[1]

[1] *LBA UMRT24, Aix Marseille Université / Université Gustave Eiffel, Marseille, France*
[2] *Decathlon SportsLab, Lille, France*

Keywords*:* multibody model ; mountain biking ; spinal fracture ; injury risk ; video analysis

1. Introduction

Mountain biking (MTB) has become an increasingly popular sport and more and more ski resorts are turning into bike parks during the summer season. During MTB practice, spine and thorax are at risk with 20% of severe injuries (Injury Severity Score > 12) implicating trunk area [1]. To prevent these injuries, riders use back protectors. However, there is no standard evaluation of these protections specific to MTB, and there is very little data available on the impact condition of the back (impact speed, force involved, risk of injury) during an MTB crash. The aim of the present work is to investigate impact conditions leading to spinal injuries during an "Over-the-bars" (OTB) scenario, identified as the main situation leading to spinal injuries [2], to better design back protectors (area, structure, force absorption threshold).

2. Methods

A video of an OTB accident after jumping from a height has been analysed (Source : Pinkbike) using Kinovea and reconstructed in multi-body (MB) simulation with Madymo to validate a mountain bike and cyclist MB coupling. Then, the model has been used to investigate the influence of initial speed and slope angle changes (4 speeds and 3 slope angles) on head impact conditions like speed and force of impact. Additionally, the force on each vertebra was recorded to predict the risk of injury.

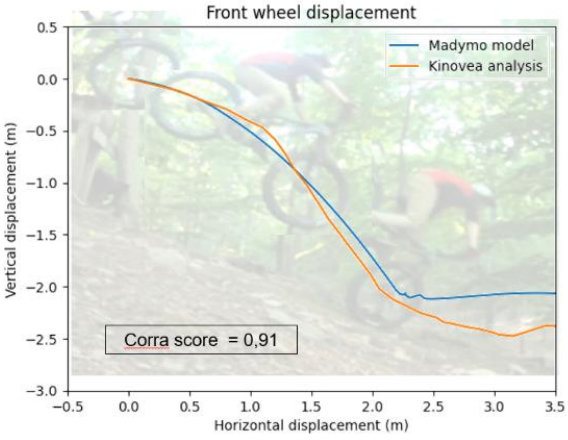

Figure 1 – Validation of the multibody model

3. Results and Discussion

In all scenarios, a head-first impact is observed with head-to-ground impact velocities ranging from 2 to 13 m/s, so higher values than the initial cyclist speed because of the momentum created by the OTB mechanism. An increase of the initial velocity or the landing slope angle reduces cervical spine force. In most simulations, spine injury thresholds are exceeded for cervical forces.

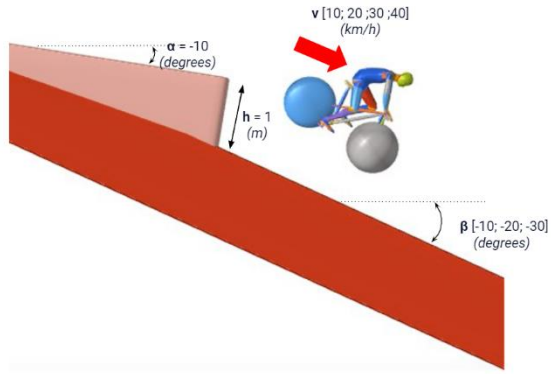

Figure 2 – Parametric study of an OTB after a jump

Velocity and slope angles variation change fall kinematics by influencing fall length and bike angle of impact. Thus, the head position at impact has a great influence on cervical loading with face impact leading to fewer strains in the cervical spine than top of head impacts [3]. However, for this OTB with a fall from a height, risks of cervical injury are observed for all cyclist speeds and slope angles, which highlights a real need to rethink back protectors to limit extension of the spine during head-first impact. Further investigation of OTB mechanisms with smaller height drops, ground hardness and friction coefficients must be considered.

References

[1] Dodwell and al. (2010), The Am J Sports Med

[2] Kim and al. (2006), J Trauma Acute Care Surg.

[3] Allen and al. (1982), Spine.

***Sophie Bonte. Email: sophie.bonte@univ-eiffel.fr**

Effect of brain personalization on the response of a finite element head model in a car accident reconstruction

Thais Manlius[3*], Clémence Delteil[1,2], Yves Godio-Raboutet[3], Pierre Simeone[4,5], Eric Wagnac[6,7], Nicolas Bailly[3], Lionel Thollon [3]

[1] *Forensic Department, Assistance Publique-Hôpitaux de Marseille, La Timone, 264 rue St Pierre, 13385 Marseille Cedex 05, France*
[2] *Aix Marseille Univ, CNRS, EFS, ADES, Marseille, France*
[3] *Aix Marseille Univ, Univ Gustave Eiffel, LBA, Marseille, France*
[4] *Aix Marseille University, AP-HM, Department of Anesthessiology and Critical Care Medicine, University Hospital Timone, Marseille, France*
[5] *Aix Marseille University, CNRS, Inst Neurosci Timone, UMR7289 Marseille, France*
[6] *Department of Mechanical Engineering École de technologie supérieure, 1100 Rue Notre-Dame Ouest, Montréal, H3C 1K3, QC, Canada*
[7] *Research Center, Sacré-Cœur Hospital Montreal, 5400 Boul Gouin O, Montréal, H4J 1C5, QC, Canada*

Keywords*:* Traumatic brain injury; Pathology; Finite element head model; Imagery

1. Introduction

Traumatic brain injury affects millions of people each year and is the leading cause of traumatic death. FEM models can be used to reconstruct impacts and predict brain deformation to understand injury mechanisms. Most models are generic, meaning that they represent average brain geometry and mechanical properties and don't account for thepatient specificity. Several approaches have been proposed to personalized the brain model: [1] Scaling**,** which adjusts the brain model based on volume without changing shape, and [2] Morphing, which adjusts both volume and geometry. This study will investigate the effect of geometrical personalization on the brain's mechanical response in a real crash scenario, comparing FEM predictions with actual injuries observed via MRI to evaluate accuracy.

2. Methods

A pedestrian-car accident, leading to a severe head injury, was reconstructed using a tetrahedral finite element mesh of the head and neck developed in HYPERMESH software. The impact conditions of the head during the crash were determined using a design of experiment approach, considering parameters such as impact zone, velocity, angle, and impacted area, with the aim of numerically reproducing the exact pattern of facial fractures observed in the case. Once the impact conditions were determined, three different brain model personalizations were evaluated: (1) a generic model based on Atlas HCP 1065, (2) a generic model with subject-specific internal brain structures, and (3) a scaled model with subject-specific internal brain structures.

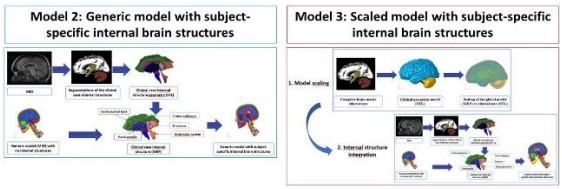

Figure 1: Stages of FE model personalization

Two analyses were performed: (1) the effect of personalization on mechanical responses (stress, strain), and (2) a comparison of response distribution with real injuries. The maximum principal strain threshold for brain injury was defined at 0.21 [3].

3. Results and Discussion

The selected impact condition was a head ground impact localized in left maxilla and with an impact speed of 6m/s. With this condition the simulated fracture closely match the fracture observed in CT scan. The models with different level of personalization presented different regional strain levels. All three models displayed regions exceeding the tolerance threshold (highlighted in red) at the mesencephalic level of the corticospinal tracts. This finding is consistent with the patient's MRI, explains the left hemiplegia. However, using this threshold, all three model overestimated the risk of lesion in the upper part of this corticospinal tracts. In the corpus callosum, the response of models differs with the scaled model best predicting the damaged zone observed at MRI.

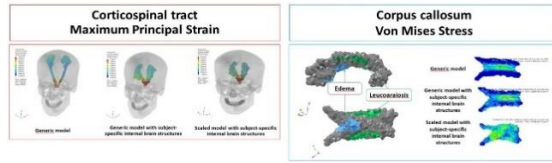

Figure 2: Corticospinal tract and corpus callosum Strain and stress distribution

4. Conclusions

This preliminary study demonstrates the effect and potential benefits of brain model personalization in accident reconstructions. Differences in stress, strain, and pressure were observed between varying levels of brain personalization, with the highest lesion prediction obtained from the most personalized model. However, all models tended to overestimate the risk of lesions in non-injured areas. Only geometric personalization was applied; in future work, it would be beneficial to also incorporate personalized mechanical properties.

References

[1] Wu et al. (2023), Biomech Model Mechanobiol.
[2] Li et al. (2021), Biomech Model Mechanobiol.
[3] Bain & Meaney (2002), Journal of Biomechanical Engineering.

***Thaïs Manlius. Email** : thais.manlius@univ-eiffel.fr

A Novel Anthropomorphic Biomechanical Model of the Human Body: a Pedestrian-Car Impact Study

G. Pascoletti[1(*)], G. Franceschini[1] and E. M. Zanetti[1]

[1] *University of Perugia, Department of Engineering, Via G. Duranti, 93, 06125, Perugia, Italy*

Keywords*:* ATB; Multibody analysis; Pedestrian; Impact mechanics; Forensic biomechanics

1. Introduction

Articulated Total Body (ATB) models are multibody (MB) models widely used in biomechanical human simulations. Inertial and geometrical properties of body segments, as well as joint properties are accurately reproduced to simulate the actual body behavior, while the outer geometry is usually roughly approximated. The authors have developed a novel passive ATB model, faithfully replicating an anthropomorphic shape[1], based on a Statistical Shape Model. In this work, the model was validated against experimental impact tests between cars and cadavers[2].

2. Methods

Experimental tests were performed on five different cadavers[2]; the corresponding MB models (Hexagon Adams Software) included the car and the android model. Cars were modelled as rigid bodies free to translate in the horizontal direction under the action of an initial velocity; a braking force took place after the first impact with the ATB model.

Cadavers' models were created according to the anthropomorphic ATB methodology[1]; the initial configurations were adjusted to replicate the respective experimental ones, prior the impact with the vehicle. Contact forces between body segments and the car or the ground were taken into account. Numerical and experimental results were compared both in terms of global kinematics and using the EEARTH[3] metric *E* for the head's time histories (displacements and velocities). The *E* score includes phase, magnitude and slope errors of a numerical curve compared to the respective experimental one and it can range from 0% to 100%: the higher its value the better the correspondence.

3. Results and Discussion

Numerical models well replicated impact kinematics for all the tests (Fig. 1 shows an example for test 2); the correspondence was good also for relevant impact timings, deviations keeping below 0.5 s. Referring to head's time histories, *E* scores above 80% (excellent agreement) were obtained for displacements. Good results were found also for horizontal velocities (v_y), with the lowest *E* reaching 65% for two tests; more critical values were found for the vertical velocity component (v_z). Major differences took place for v_z main peaks, produced by the head impact to the car and to the ground.

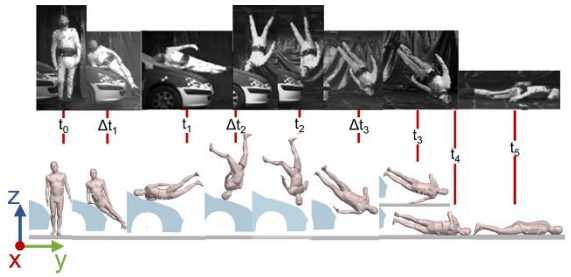

Figure 1. Global kinematic comparison (test 2).

Contact parameters have a significant impact on the dynamic response, and therefore these parameters were tuned to optimise the *E* score. Tests 2 and 5 achieved the highest improvement (E_{opt} in Table 1), while test 3 remained critical, due to absence of the head-car impact in experimental data.

Test	1	2	3	4	5
E	75%	66%	46%	71%	52%
E_{opt}	73%	72%	48%	73%	75%

Table 1. *E* and E_{opt} scores for v_z

4. Conclusions

The performances of a novel passive anthropomorphic ATB model were here investigated for a pedestrian-car impact. Comparison with experimental data showed that the mechanics of impact was well replicated by the model. The effect of proper contact definition on the velocity response was pointed out, and contact parameters optimised. The proposed model has demonstrated its ability to provide reliable information on the impact kinematics, resulting in a promising numerical tool for accident reconstruction and injury evaluation.

References

1. Pascoletti, G., Huysmans, T., Molenbroek, J.F.M., Zanetti, E.M., 2023, From an ellipsoid-based to an anthropomorphic articulated total body model for multibody applications. Int. J. Interact. Des. Manuf.
2. Shang, S., Masson, C., Teeling, D., Py, M., Ferrand, Q., Arnoux, P.J., Simms, C., 2020, Kinematics and dynamics of pedestrian head ground contact: A cadaver study. Saf. Sci. 127: 104684
3. Zhan, Z., Fu, Y., Yang, R.J., 2011, Enhanced error assessment of response time histories (EEARTH) metric and calibration process. SAE 2011 World Congr. Exhib.

***Corresponding author. Email: giulia.pascoletti@unipg.it**

Fracture toughness of an industrially supplied cancellous bone simulant

Muhammad Asfand Sohail, Peter Zioupos

Biomedical Engineering, School of Engineering, University of Hull, Kingston Upon Hull, UK.

Introduction

The human cancellous bone has a hierarchical structure that gives it its unique mechanical properties. The study of the mechanical integrity of bone is crucial in diagnosing and treating condition of bone loss such as osteoporosis. Fracture toughness of human cancellous bone is an important parameter when predicting bone strength, Over the last decade researchers (Cook, 2009) have applied the fracture mechanics calculations on human bone. This study provides us with fracture toughness and compressive strength of commercially available SAWBONES cancellous bone simulants. These blocks have wide range of applications in orthopaedic industry such as bone disease research and bone surgery practice. Thus, understanding their mechanical properties may enable us in development of better bone simulants.

Methods

A total of 14 Sawbones cancellous bone blocks having open cell, cellular and solid structures were acquired for this study. The densities of the blocks ranged from 0.07-0.81g/cc. The micro-CT scans were conducted using X-tech HMK160. Morphometric analysis was carried out suing VG Studio Max 2.1 software. Using ASTM standard E399-90 the blocks were cut into disk shaped compact specimen DC(T). FT and compression tests were carried out using mechanical tester Easy Test EZ-50.

Results & Discussion

The morphometric analysis of the samples showed that the BV/TV was the strongest predictor of strength which proves that with increase in bone quantity the mechanical strength increases. TbS showed an inverse relationship with bone strength. The fracture toughness results showed a significant increase with an increase in the bone density. The compressive strength of the samples also showed a positive relationship with bone density. Overall, in comparison to human cancellous bone the compressive strength of the Sawbones bone simulants was found to be lower.

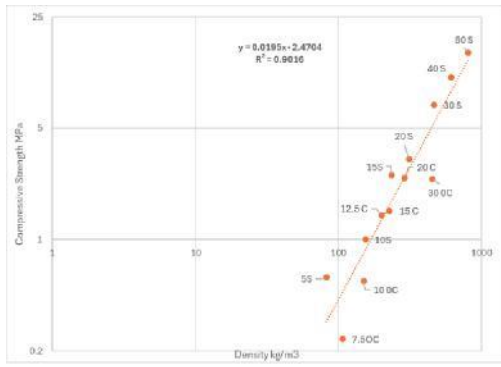

Figure 1 Compressive strength of Sawbones simulants in relation to apparent density

Conclusions

This study provides valuable insights into the fracture toughness and compressive strength of commercially available cancellous bone simulants, specifically Sawbones. By investigating their microarchitecture and correlating morphometric parameters with mechanical properties, it was found that material strength is closely tied to factors such as bone volume fraction (BV/TV) and apparent density, while trabecular separation (TbSp) is associated with weaker properties. These differences, driven largely by variations in microarchitecture and manufacturing techniques, highlight the importance of further refining bone simulants. This research has the potential to guide the development of advanced bone mimetics, which could play a crucial role in orthopaedic training and research, particularly given the challenges of sourcing large samples of biological bone. Ultimately, this work could contribute to enhancing the realism and applicability of bone simulants in both clinical and research settings.

References

Cook, R.B. and Zioupos, P., 2009. The fracture toughness of cancellous bone. Journal of biomechanics, 42(13), pp.2054-2060.

***-Corresponding author. Email: asfand.sohail5@gmail.com**

Three-Dimensional Simulation of Fracture Healing with Two Different Fracture Fixation Devices

G. Morgan[1 (*)], A. Ramasamy[1, 2, 3], and S. Masouros[1]

[1] *Department of Bioengineering, Imperial College London, UK*

[2] *Academic Department of Military Trauma and Orthopaedics, Royal Centre for Defence Medicine, ICT Centre, Birmingham, UK*

[3] *Trauma and Orthopaedics, Milton Keynes Hospital NHS Foundation Trust, Milton Keynes, UK*

Keywords: fracture healing algorithm; fixation device; in silico trial; callus; finite element

1. Introduction

Despite advancements in bone fracture treatment, the optimal fixation method for some fracture types remains unknown due to limitations in *in vivo* and *in vitro* trials [1]. *In silico* trials have previously been used to address clinical questions left unanswered by traditional research methods [2].

A recently developed and validated axisymmetric fracture healing algorithm is able to simulate the fracture healing sequence [3]. A finite-element model of the fracture and fixator is used to calculate the mechanical strains in the callus region. The healing algorithm determines the updated local callus tissue composition based on these strains. The FE model is re-run with updated material properties, and this simulation is performed iteratively.

This study expands the existing fracture healing algorithm to 3-D and applies it to two femoral fracture models to demonstrate the capability of the algorithm to capture differences in healing.

2. Methods

A previously described fracture healing algorithm was expanded to 3-D. FE models were developed of a human femoral shaft fracture idealised as a 5 mm osteotomy. One model was developed with an intramedullary nail fixator, which was represented with 6 single DoF springs. A laterally placed locking plate was modelled along with 6 locking screws. An axial load of 500 N was applied at the hip joint.

3. Results and Discussion

The bone concentrations of the simulations of the models of the intramedullary nail and locking plate fixated fractures at iterations 7, 14, 21, 35, and 100 are shown in Figure 1. The locking plate and screw outlines are visible in Figure 1b.

In the simulation of the locking plate model, the healing algorithm correctly predicts greater callus formation on the far-plate cortex. In the simulation of the intramedullary nail model, the callus has axisymmetric development.

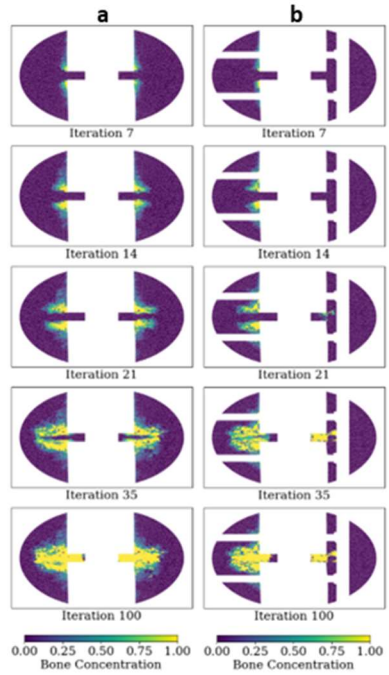

Figure 1: Coronal cross-sectional view of the callus with local bone concentration shown for the fracture treated with (a) intramedullary nailing (b) locked plate fixation.

4. Conclusions

A novel fracture healing algorithm was able to capture physiologically the difference in callus development caused by two different fixators. This study demonstrates the suitability of this algorithm for an *in silico* trial of fracture fixation treatment.

Acknowledgments

GM was supported by the EPSRC (EP/T51780X/1).

References

[1] Griffin, X. et al., *BMJ Open*, 2019; e026810.
[2] Sarrami-Foroushani, A. et al., *Nat Commun*, 2021; 12:3861.
[3] Morgan, G. et al., *Euro Soc Biomech 2024*.

***Corresponding author. Email: george.morgan16@imperial.ac.uk**

Vibration reductions in the use of Brush Cutter

Massimo Cavacece

Department of Mechanical Engineering University of Tor Vergata, Rome Italy

Keywords: Vibration reductions human whole body vibrations hand-arm system

1. Introduction

Back pain may depend on the mechanical vibrations produced by the tools during the manual processing of the worker. Prolonged and excessive mechanical vibrations represent loads applied to the whole body (WBV) and hand-arm system (HAV). Long workloads can lead to health problems. The damage caused to the man is pain in the hands, lower arm, back pain, and difficulties with lumbar disc herniation. Mechanical shocks on the whole body and hand-arm system characterize the activities of manual workers. Low back pain risk factors are posture and stress induced by electro-mechanical tools. In their daily work, a worker with manual skills can use one or more devices that can produce mechanical vibrations, such as the following portable power tools: brush cutter, chainsaw, and electric saw. Brush cutter's mechanical vibration emissions can generate a professional risk of mechanical vibration injury, which stresses the human body. Frequent exposure to whole-body vibration and hand-arm systems can deteriorate human body capabilities even with permanent effects. The spine is the central structural element that supports the upper part of the body and protects against spinal disorders that could generate neurological consequences. Spinal disorders may be the result of vibration exposure combined with other factors. Working posture, anthropometric characteristics, physical workload, noise, and individual susceptibility (age, pre-existing disorders) can produce disorders in the human spine. The intervertebral discs support high compressive loads and shear deformations, allowing flexibility and rotation. The intervertebral disc may be subject to ruptures and degenerative processes. Mechanical stresses applied to the disc can accelerate the development of degenerative changes. This research aims to study the transmissibility of vibrations of an instrument held and guided by hand by a worker. The study analyzes the vibration risks associated with using brush cutters to evaluate the effects of mechanical vibrations on the hand-arm system and the whole body. The research estimates the reduction of vibrations on the hand-arm system and the whole body.

2. Experimental set-up

The accelerations are recorded by a data logger AX6 activity. The measurement points are shaft of brush cutter and fingers, wrist, elbow, shoulder, back of worker. The brush cutter has the following characteristics 41.6 cc / 2.0 kW-2.7 hp/ 8.5 kg. The anti-vibration system has a multifunction handle, two-handed (adjustable without using tools), an engine with a petrol mixture, and a universal shoulder strap for cutting thick grass. The cutting head was driven by a rigid shaft, which transmitted engine power to the cutting attachment indirectly through the angle gear. Brush cutter can be used by a worker several times during a year. If the worker uses the brush cutter twice a year and has to cut the grass for an area of 5000 m2, assume a cutting time of 8 hours until you reach the 16 hours of exposure time. A brush cutter is a portable work machine with a cutting attachment mounted on a shaft over 1 m long. The brush cutter can cut wood and grass. Attachment types can be circular blades or nylon thread. Vibration changes depending on the state of operation of the motor, the type of cutting head, and the applied working technology. As before mentioned, the measuring points are the right hand, wrist, elbow, lumbar spine, and right shoulder to evaluate the frequency response functions on hand arm system and on human whole body.

3. Results

The maximum energy content is manifested at low frequencies.

4. Discussion

4.1 Hand arm vibration

The exposure limit value (ELV) is the maximum vibration value for an operator and a single day. The ELV parameter represents a daily exposure of 5 m/s2 A(8) for vibration on the hand-arm system. The action exposure value of 2,5 m/s2 A(8) means a high risk for workers. Workers should use vibration-damping gloves to protect themselves from HAV-prolonged exposure to white finger syndrome (WFS) or Raynaud syndrome.

4.2 The vibration of the whole body

Mechanical vibrations, acting on the feet or other parts of the body, produce mechanical vibrations to the whole body. Prolonged exposure to WBV can be associated with severe lumbar pain. For whole-body vibration, the ELV parameter allows a daily exposure of 1.15 m/s2 A(8), and the EAV allows 0.5 m/s2 A(8).

4.3 Biomechanics of the spine

Brush cutter is supported by a human operator on his shoulders and, simultaneously, on his back. The arms and hands control the brush cutter. The posture of human operators for the operation of mowing the grass is standing and slightly bent forward. The human spine is exposed to mechanical vibration in the following directions: according to shoulder direction and foot direction. The weight of the brush cutter is about 9 Kg providing mechanical stress on the human spine. Measurements were made only on the human body and under full load. The accelerometer was on the right hand.

4.4 Vibration reduction

The drive shaft, cutting attachment, and motor represent the parts that emit vibrations. Optimization of shaft construction reduces low-frequency vibration. Increasing the wall thickness of the shaft tube (but not its weight) in the area for mounting the crankshaft bearing and handles can reduce mechanical vibration by 20%-30%. The steering wheel handles from the materials have anti-vibration characteristics using elastomers.

4.5 Ergonomics of the handle

The diameter of the handle assures the operator to hold the tool with the hand opposite to the thumb, in order to use the muscle of the forearm. The shape of the handle has the shape of the hand to accommodate the anatomy of the operator's hand.

5. Conclusion

The objective of this research is to investigate the reductions of vibrations from an instrument that is held and guided by a worker. The drive shaft, cutting attachment, and motor are the components that emit vibrations. The thickness of the shaft tube in the area for mounting the crankshaft bearing and the ergonomics handles can reduce mechanical vibration by 20%-30%. Materials steering wheel handles can offer anti-vibration features using elastomers. The attenuation of vibration is noticeable from the fingers to the elbow, elbow and back of the worker.

*** Corresponding author. massimocavacece@icloud.com**

Modification of Psychophysical Laws in Auditory Intensity Perception

Massimo Cavacece

Department of Mechanical Engineering University of Tor Vergata, Rome Italy

Keywords: Psychophysical Laws Auditory Intensity Perception

1. Introduction

In most psychophysical experiments, the equation

$\psi = k\,\phi a$ (1),

accurately describes the relationship between sensory magnitude judgments and stimulus magnitude. This equation becomes highly inaccurate for weak stimuli near the absolute threshold. The logarithm of apparent magnitude, plotted against the logarithm of stimulus magnitude, appears linear (a power function) only at higher stimulus values. At stimulus values near the absolute threshold, the relationship becomes concave downward.

2. Methods

A slight modification to the equation eliminates the deviation from the power law. The power law holds for the entire range of perceptible stimuli, when a constant $\phi 0$ is subtracted from the values of. According to some investigators, the continuous represents the absolute threshold.

Thus, subtracting M from may be equivalent to specifying the stimulus ineffective units above the threshold rather than in units above the zero point on the physical scale. The general form of the power function becomes

$\psi = k\,(\phi - \phi 0)$ (2),

where $\phi 0$ is the value of the absolute threshold. The process of correcting the stimulus scale to match the zero point of the psychological scale has been successful in applying it to psychophysical scales such as brightness, temperature, cutaneous vibration, cutaneous apparent successiveness, and salt taste.

Elkman proposed another form of the law of power

$\psi=\psi 0+\phi ta$ (3),

where $\phi 0$ is the basic sensory noise to which the sensory magnitude produced by an external stimulus, ϕa

It is important to note that Equations (2) and (3) present two distinct hypotheses regarding how sensory magnitude changes with increasing stimulus intensity. In Equation (2), subtracting a constant from stimulus intensity suggests that sensation magnitude follows a power function of effective stimulation above the threshold.

Conversely, Equation (3) implies an adjustment for sensory noise rather than the threshold. Equation (3) suggests that sensation magnitude depends on stimulus intensity raised to power plus a constant to account for sensory noise.

Zwislocki's work in 1965 demonstrates the use of a specific modified power function to address the issue of auditory masking. In 1964, Hellman and Zwislocki conducted a detailed study on the loudness functions of a 1000-Hz tone presented to observers against different levels of background noise intensity. Zwislocki formulated the power law for loudness in the following way:

$Ls= k(Es+EN)\theta-EN\theta$ (4)

The loudness of the signal, , is equal to a Ls constant, k, times the sum of the energy of the signal, Es , and the energy of the noise, EN, raised to a power, θ, minus the energy of the noise raised to a power, θ.

Relation (4) considers the analytic properties of the auditory system to evaluate the loudness of the entire acoustic event, the random noise alone, or the signal. When we hear a signal in the presence of loud noise, the signal doesn't sound loud if it's barely audible above the noise, even if it's very intense. Zwislocki's formula enables us to calculate the loudness of a signal by subtracting the loudness of the noise from the combined loudness of the signal and noise.

Zwislocki's formula allows us to calculate the loudness of a signal by subtracting the loudness of the noise from the combined loudness of the signal and noise. Loud if it is barely audible above the noise background, even though it is very intense; yet the noise sounds loud, and the overall acoustic event sounds loud. Zwislocki's (1965) formula permits us to calculate the loudness of a signal by subtracting the loudness of the noise from the loudness of the signal plus noise.

If the noise is external, its energy can be measured and its value is specified in the equation. However, internal noise is produced by spontaneous activity If the noise comes from outside, its energy can be measured and its value specified in the equation. However, noise, generated internally by spontaneous activity in the sensory system, depends on terms of equivalent stimulus energy. Zwislocki (1965) has provided the means for making the necessary calculations. It is assumed that masking by internal noise determines the threshold of audibility for a signal presented in quiet external conditions.

Research in auditory psychophysics has conclusively revealed that when a tone is masked by noise, only the frequencies in the noise close to the frequency of the tone do the masking. The range of frequencies in the noise that surround the frequency of a tone signal and act as a masker is called the critical band. It has been determined that when a tone is barely audible against a noise background, the energy in one critical band is approximately 2.5 times that of the signal.

Zwislocki used these concepts, developed from experiments in which external noise was used to mask tones, to arrive at a procedure for calculating the equivalent sound energy of internal noise. It was proposed that the equivalent sound energy of internal noise is 2.5 times the threshold energy of a barely audible tone presented in quiet conditions.

The research proposes a comparison of results by applying the above mentioned reports to case studies.

*** Corresponding author. massimocavacece@icloud.com**

Predicting Early-Stage Damage in Pelvic Soft Tissues Using Hyper-Viscoelastic Modeling

A.S Caro[1(*)] and S. Iaquinta[1]

[1] *LMGC, IMT Mines Ales, Univ Montpellier, CNRS, Ales, France*

Keywords*:* perineal skin; hyperviscoelasticity; Mullins effect, Relaxation, Damage

1. Introduction

The pelvic floor supports pelvic organs but is prone to Pelvic Floor Dysfunctions, affecting up to 32% of women worldwide. Factors such as age, menopause, and traumatic events like perineal tears during childbirth significantly contribute to these dysfunctions (Jansson et al., 2020). Preventing these tears may be possible through anticipation. In our team, we aim to achieve this by monitoring the in-situ evolution of parameters (such as viscosity) and identifying indicators that could indicate pre-damage before it becomes visible (tissue degradation, holes). The first step, and the focus of this presentation, is to conduct cyclic tensile tests on porcine perineal tissues to characterize the hyper-viscoelastic behavior and the stress softening phenomenon.

2. Methods

Skin tissues were extracted after dissection from porcine perinea supplied by the local slaughterhouse in Alès (SEMAAC). Rectangular shapes were sampled from tissues of pig perineum. Instrumented pure-shear tests were conducted under a constant strain speed of $0.03s^{-1}$. The test consisted in applying cycles every 10% of elongation, each cycle being composed of traction, relaxation and unloading phases. Digital Image Correlation (DIC) enabled the evaluation of the in-plane strain tensor (Fig. 1)(Caro-Bretelle et al., 2016).

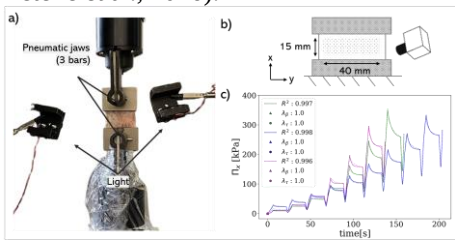

Figure 1 Device, sample geometry and pure shear stress versus elongation

A visco-hyperelastic incompressible constitutive model, which generalizes the Zener's model in large strain (Rebouah & Chagnon, 2014), allows us to express the global fitst Piola-Kirchhoff stress tensor in terms of hyperelastic ($\bar{\bar{S}}_{iso}$), viscous ($\bar{\bar{Q}}$) and volumic $\bar{\bar{S}}_{vol}$ components:

$$\bar{\bar{S}} = \bar{\bar{S}}_{iso} + \bar{\bar{Q}} + \bar{\bar{S}}_{vol}$$

with $\tau\,\dot{\bar{\bar{Q}}} + \bar{\bar{Q}} = \tau\beta\dot{\bar{\bar{S}}}_{iso}, \bar{\bar{Q}}(t=0) = 0,$
where τ is the relaxation time in second and β is an adimensional energetic parameter. The originality of this presentation is that the viscous parameters depend on the applied strain.

3. Results and Discussion

An optimization procedure allows us to fit experimental data with the proposed modelling. The evolution of the viscous parameters is shown in Fig. 2 for a testing on skin tissues from 3 different pigs.

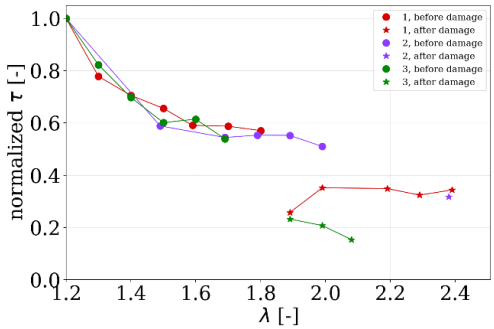

Figure 2 Time relaxation evolutions as a function of elongation

4. Conclusions

Evolutive viscous parameters appear to be effective in describing pre-damage in porcine soft tissues, as they provide good reproducibility and exhibit a change in behaviour as the tissue approaches a damaged state.

References

Caro-Bretelle, A. S., Ienny, P., et al,2016, Constitutive modeling of stress softening and permanent set in a porcine skin tissue: Impact of the storage preservation. Journal of Biomechanics, 49(13), 2863–2869

Jansson, M. H., Franzén, et al, 2020, Risk factors for perineal and vaginal tears in primiparous women, BMC Pregnancy and Childbirth, 20(1), 749.

Rebouah, M., & Chagnon, G., 2014, Extension of classical viscoelastic models in large deformation to anisotropy and stress softening. International Journal of Non-Linear Mechanics, 61, 54–64.

***Corresponding author. Email: Anne-Sophie.Caro@mines-ales**

A numerical musculo-skeletal model of the shoulder for the study of the biomechanics of the sternoclavicular joint

Talal Bin Irshad[1 (*)], Giulia Pascoletti[1], Elisabetta M. Zanetti[1]

[1] *University of Perugia, Department of Engineering, Via G. Duranti, 93, 06125, Perugia, Italy*

Keywords*:* Sternoclavicular joint; Range of motion; Muscle forces; Joint reaction forces; Multibody model

1. Introduction

Designing a prosthetic sternoclavicular (SC) joint is challenging due to limited biomechanical knowledge of this joint, often resulting in reduced mobility and joint instability after surgery. Experimental measurements of joint forces are invasive, making virtual models essential for studying joint biomechanics. The model presented here incorporates key bones, muscles, and ligaments of the thoracoscapular region, offering insights into joint movements and forces. The study uses shoulder movements as benchmarks to validate the model and extend to range of motions (ROMs) and joint forces assessment of the SC joint.

2. Methods

Ten healthy volunteers (three females, seven males) participated in this study to assess shoulder movement using musculoskeletal modelling (OPENSIM 4.4). Participants performed three types of motions: abduction-adduction, flexion-extension, and shrugging, with three trials for each. Movements were captured using four inertial sensors placed on the thorax, scapula, clavicle, and humerus (Figure 1a). The sensor positions were determined through preliminary testing to ensure optimal movement capture. The musculoskeletal model used, based on the Thoracoscapular Shoulder model from Stanford University [1], was scaled to each participant's using anthropometric data. Inverse kinematic analysis was applied to match experimental kinematics by minimizing the error between recorded and simulated motion. Static optimization was then used to calculate individual muscle forces by minimizing the sum of squared muscle activations.

Lastly, joint reactions were computed, calculating the forces and moments transferred at the SC joint during movements.

3. Results and Discussion

The model captured joint angles and muscle forces, reflecting the dynamic interactions of the clavicle and surrounding muscles. Sternoclavicular joint experienced peak reaction forces of 76% body weight during abduction-adduction, 70% during flexion-extension, and 55% during shrug movements (Figure 2b). Validation against previous studies [1] confirmed the accuracy of these results. This validation demonstrates the model's reliability in accurately simulating joint forces, supporting its use in prosthesis design and joint analysis.

a)

b)

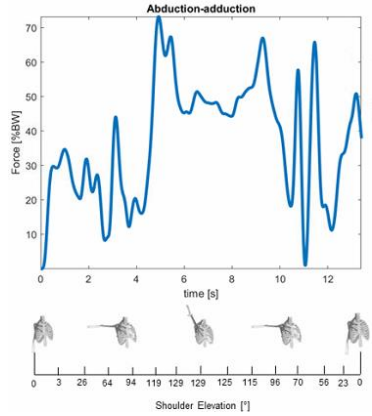

Figure 1. a) IMU Sensor placement on subjects for experimental data collection b) Joint reaction forces as percent of body weight during Abduction-adduction

4. Conclusions

The study explored the kinematic behavior of the sternoclavicular joint through abduction-adduction, flexion-extension, and shrug motions using a musculoskeletal model and IMU sensors.

Kinematic experimental data from ten subjects were collected and used for assessing the numerical model and providing valuable insights for artificial joint design. It highlights the need for broader studies and diverse movements to refine joint specifications and rehabilitation strategies.

References

1. A. Seth, M. Dong, R. Matias, and S. Delp, "Muscle contributions to upper-extremity movement and work from a musculoskeletal model of the human shoulder," Front Neurorobot, vol. 13, 2019, doi: 10.3389/fnbot.2019.00090

***Corresponding author. Email: talalbin.irshad@dottorandi.unipg.it**

Design of Cellular Hexagonal and Cancellous-like plates for laminectomy

Saheed Ademuyiwa, Gillian Pearce, Peter Zioupos

Department of Engineering, University of Hull, Kingston upon Hull HU6 7RX, UK

Keywords: Laminoplasty Plate, Honeycomb Structure, Mechanical Properties, Spinal Surgery, 3D Printing

1. Introduction

Laminoplasty and laminectomy are essential surgical techniques used to relieve spinal cord or nerve root compression caused by conditions such as spinal stenosis, herniated discs, and tumors [1]. These procedures often involve removing or altering portions of the vertebral lamina to reduce pressure, but they can destabilize the spinal column, potentially leading to complications post-surgery[2]. Traditional metal implants are typically used to provide structural support, yet issues like stress shielding and poor osseointegration remain significant challenges[3]. We propose here that, by using Computer-Aided Design (CAD) tools and 3D printing technology, we can design and develop a cancellous-like laminoplasty plate that combines flexibility, strength, and biocompatibility and one that better mimics the natural bone structure, improving surgical outcomes and patient recovery.

2. Methods

The laminoplasty plate was designed using **Solid Works** CAD software and the design feature is a hexagonal cellular structure, which emulates the porous nature of cancellous bone to balance mechanical strength with flexibility. A number of iterations of the plate were designed, each incorporating minor variations in cell size (ranging from 0.4mm, 0.8mm, 1.0mm, 1.2mm and solid plate) to optimize the biomechanical properties. They were fabricated in Polylactic Acid (**PLA) by 3D printing (AM).** The CAD-AM process allowed for the creation of complex geometries that would be difficult to achieve using traditional manufacturing methods. Multiple prototypes were printed for testing and comparison. Mechanical testing was conducted to evaluate the structural integrity of the plates in tension and compression and FEA was performed (SolidWorks) for predictions. The aim was to determine the plate's capacity to withstand physiological loads while maintaining structural stability.

3. Results and Discussion

The tensile strength testing of various laminoplasty plate designs, including honeycomb structures (0.4mm, 0.8mm, 1.0mm, and 1.2mm) and a solid design, revealed distinct mechanical properties in terms of stiffness, strength, and flexibility. The 0.4mm honeycomb design demonstrated the highest stiffness and load bearing capacity making it ideal for high-load applications with minimal deformation but limited flexibility. The 0.8mm design offered a balanced performance in stiffness and strength for regions requiring moderate flexibility. The 1.0mm plate, had the lower stiffness and load bearing, demonstrated increased strain tolerance (up to 0.156±0.0456) making it adaptable for dynamic spinal regions. The solid plate had the highest strain at failure (0.163±0.0474) and it was more flexible than the rest, but may be prone to stress shielding.

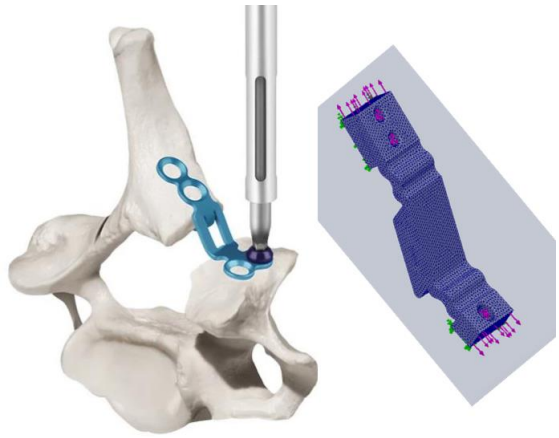

Figure 1: Commercial plate in-situ and our design of a custom made cellular body 3D printed plate with a honeycomb cellular structure.

4. Conclusions

The study demonstrated that the mechanical properties of laminoplasty plates are significantly influenced by design structures and honeycomb sizes. While solid and wider designs provide greater stiffness and strength, they often sacrifice the flexibility necessary for spinal integration and osteointegration. Some of our plates displayed high stiffness but limited flexibility, some had a good balance between strength and flexibility, one design the 1.0mm honeycomb was an optimal choice, providing a strong combination of stiffness and adaptability for spinal applications. Overall, the study emphasizes that the choice of design should be tailored to the specific needs of each patient and procedure.

References

1- doi: https://doi.org/10.1177/1947603520907665
2- doi: https://doi.org/10.1007/s10143-014-0565-3
3- doi: https://doi.org/10.1002/ar.b.10012

***corresponding author: p.zioupos@hull.ac.uk**

Development of a Musculoskeletal Model as an In-Silico Tool to Enhance Prosthesis Design in Mandibular Reconstruction

T. Bin Irshad[1], G. Putame[2,3*], G. Pascoletti[1], G. Franceschini[1] and E. M. Zanetti[1]

[1] *Department of Engineering, University of Perugia, Italy*

[2] *Department of Mechanical and Aerospace Engineering, Politecnico di Torino, Italy*

[3] *Polito[BIO]Med Lab, Politecnico di Torino, Italy*

Keywords: musculoskeletal; multibody; in-silico; temporomandibular joint, mandibular reconstruction.

1. Introduction

Nowadays, 3D-printed mandibular prostheses are increasingly employed following extensive bone resections and are typically designed by mirroring the contralateral healthy side. Often, design validation is based merely on assessing geometrical interference in various static positions of the mandible, overlooking the dynamic role of hard and soft tissues. This study aims to develop a multibody (MB) mandibular model to be applied in improving the design process of patient-specific prostheses by including biomechanical information, such as the estimation of range of motion, risk of dislocation, and potential overloading of anatomical structures.

2. Methods

Firstly, a MB model was created in Adams View (Hexagon AB, Sweeden) consisting of two rigid bodies, i.e., maxilla and mandible, with the main ligaments and muscle represented by point-to-point force vectors (Fig. 1a). The temporomandibular joint (TMJ) was modelled by a contact pair between the condyle and glenoid fossa. An inverse dynamic approach was implemented by imposing the opening/closing motion of the mandible, while the TMJ displacements were recorded (protrusion-retraction, depression-elevation, medio-lateral) and compared with experimental data available in literature [1] to validate the model (Fig. 1b). Thereafter, the analysis was repeated by including a unilateral mandibular prosthesis into the model (Fig. 1c), thereby enabling the assessment of surgical treatments.

3. Results and Discussion

The MB model has proven good performance in reproducing kinematic data reported for a generic patient. However, further validation will be performed by using patient-specific data. Notably, the introduced unilateral prosthesis resulted in overloading of the healthy side, ultimately causing an asymmetric mandibular opening. Such issue could potentially be addressed by optimizing the attachment points of residual muscles.

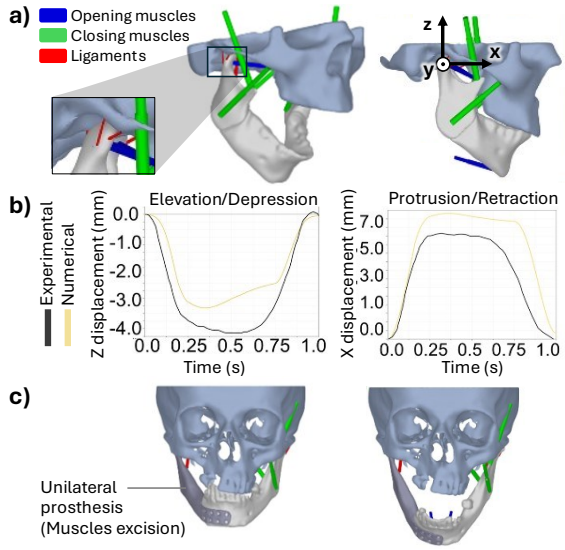

Figure 1: a) Multibody model; b) experimental vs. numerical displacements; c) asymmetric mandibular opening following prosthetization.

4. Conclusions

The presented MB model, once further validated, could enhance both the optimization of prosthesis design with respect to dynamic performance and the decision-making process during pre-operative planning, e.g., by simulating the positioning of the prosthesis or preserved muscles attachment points.

Acknowledgments

This work was supported by grant PNRR, Missione 4, componente 2 “Dalla Ricerca all'Impresa” – Investimento 3.3 “Introduzione di dottorati innovativi che rispondono ai fabbisogni di innovazione delle imprese e promuovono l’assunzione dei ricercatori dalle imprese” by NextGenerationEU.

References

1. Skipper Andersen, M., et al., 2017, Introduction to Force-Dependent Kinematics: Theory and Application to Mandible Modeling. J. Biomech. Eng. 139 (9):1-14

***Corresponding author. Email: giovanni.putame@polito.it**

Motion analysis of surgeons during ex-situ pressurized cadaveric liver left lateral sectionectomy to shorten the learning curve

P.G. Champavier[1(*)], R. Casanova[2], T. Guilbaud[1,3], D. Birnbaum[3], L. Beyer-Berjot[1,3], P.J. Arnoux[1]

[1] *Aix Marseille Univ, Univ Gustave Eiffel, LBA, Marseille, France.*

[2] *Aix-Marseille Univ, CNRS, ISM, Marseille, France*

[3] *Aix-Marseille Univ, Department of Digestive Surgery, Hôpital Nord, APHM, Marseille, France.*

Keywords*:* Laparoscopic liver surgery; Simulation training; Surgical education; Skill evaluation; Motion analysis

1. Introduction

The laparoscopic surgery is now considered as a safe approach for many specialties including liver surgery [(1)]. However, it requires delicate skills [(2,3)] and imposes a steep learning curve (LC) [(4)]. Hence, teaching programs have been developed, often using simulation. A realistic model is essential, yet not always sufficient to significantly shorten the LC. This paper thus aims to present a novel motion analysis system combined to a physical simulator previously developed.

2. Methods

Motion of surgeons with different levels of expertise was recorded during an entire left lateral sectionectomy in the Lap-Liver Trainer simulator thanks to Codamotion units, using infrared and active markers to track instruments. An algorithm was then developed to analyse motion metrics depending on the experience of the surgeon, but also on the step of the procedure.

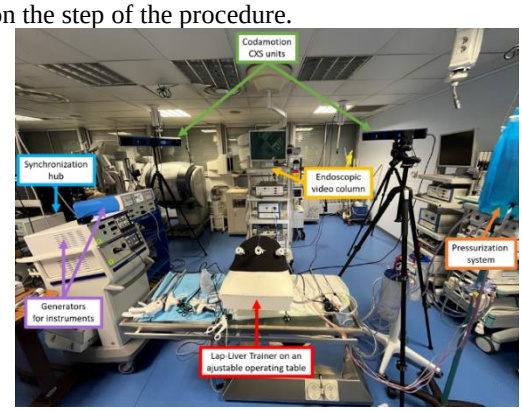

Figure 1. Experimental set-up for motion analysis.

3. Results and Discussion

The system developed presented a great feasibility, face and content validity. Significant differences were found for several metrics including duration of the procedure, electrosurgical instruments usage, gestures duration, total path length, working volumes or else instruments velocity. Breaking down the procedure step-by-step, differences were notably found during the parenchymal transection step, considered as the most difficult.

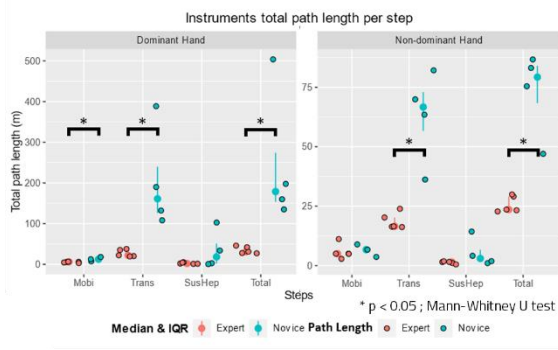

Figure 2. Path length comparison according to expertise

4. Conclusions

Our novel system recognized significant differences in several metrics according to the level of surgical experience and more precisely during the parenchymal transection. The motion analysis system developed could hence help novice surgeons to develop their skills and shorten their LC, by focusing on parameters to improve.

Acknowledgments

Thank you Max PY for your help during motion acquisitions.

References

(1) Viganò et al., 2009, Laparoscopic liver resection: a systematic review. J Hepatobiliary Pancreat Surg, 16:410:421.

(2) Crothers et al., 1999, Experienced laparoscopic surgeons are automated to the “fulcrum effect”: an ergonomic demonstration. Endoscopy, 31(5):365-369.

(3) Fuchs Weizman et al., 2015, Survey on Barriers to Adoption of Laparoscopic Surgery. J Surg Educ, 72(5):985–994.

(4) Guilbaud et al., 2019, Learning Curve in Laparoscopic Liver Resection, Educational Value of Simulation and Training Programmes: A Systematic Review. World J Surg 43(11):2710–2719

*** Corresponding author. Email: pierreguillaume1@orange.fr**

A Finite Element Model of a Post-Traumatic Ventricular Septal Defect in Asymptomatic and Symptomatic Hearts

D. Sweidy[1,2 (*)], W. Wei[1,2], F. El Louali[1,3], L. Kadem[4] and M. Evin[1,2]

[1] Laboratoire de Biomécanique Appliquée (LBA), Marseille, France; [2] Gustave Eiffel University, France; [3] La Timone Hospital, Marseille, France; [4] Laboratory of Cardiovascular Fluid Dynamics, Montréal, Canada

Keywords*:* ventricular septal defect; post-traumatic; finite element; car crash

1. Introduction

Post-traumatic Ventricular Septal Defect (VSD) is described in 5.5% of severe blunt chest trauma cases(1). It occurs mostly in the muscular part of the septum, near the apex(1,2). One mechanism explaining the defect would be a compression of the heart between the spine and the sternum, increasing the intracardiac pressure in either an isovolumetric systole or by the end of a diastole(3). However, the level of strain on the heart when compressed during the impact is still understudied. The objective of this study is to develop a detailed finite element model of the heart assessing the von Mises strain to which the septum is subject to during a car crash.

2. Methods

From an existing simulation database, two real car crash cases representative of 46 crash scenarios were analyzed. They were reproduced and simulated using Finite Element (FE) modeling with LS-DYNA (R11.0.0) and the Total Human Model for Safety (THUMS). For the 46 scenarios, the von Mises strains on the heart elements are extracted. The worst-case scenario is selected, where the magnitude of mean and the 95th percentile of strain reached a maximum of value. The force applied on the heart nodes of model (H1) by the external organs are saved and applied to a second numerical model (H2) as nodal forces. The nodal coordinates are also used to match the two hearts' (H1&H2) nodal forces.

A detailed numerical heart model (H2) (Figure 1) was previously developed in the laboratory. It includes the 4 cavities of the heart and simulates realistic heart contractions(4). It was adjusted to assess the morphological and material parameter which could influence a post-traumatic VSD: the septum as a component on its own in two sub-models (H2a&H2b), and a thinner circle (2/3 of the septal thickness) in the septum in one of the sub-models (H2b). The thin part replicates a fragile area, simulating a preexisting congenital VSD of 11.3 mm in diameter, in the muscular part of the septum, that has closed on its own. The myocardium is modeled with elastic material with a Young modulus of 4 kPa and a Poisson ratio of 0.4. In this preliminary study, only the structure is considered. Two types of boundary conditions were simulated: 1) the physiological contraction of the heart, modeled with an internal pressure load to simulate the ventricular contraction, and 2) the impact, imposed during peak left ventricular systole, is modeled with the nodal forces extracted from the first model (H1).

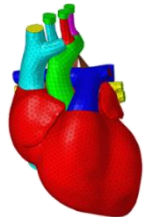

Figure 1. Heart model H2

3. Results and Discussion

The FE model, showing a strain increase during the systole, showed a cumulative strain peak when the impact occurs (Table 1). The thin part created in H2b did have an impact on the maximum strain values. Interestingly, the peak strain in all simulations was concentrated in the muscular part of the septum(1,2).

von Mises Strain	Crash+Diastole H2a&H2b	Crash+Systole H2a-H2b	
Max	0.32	0.52	0.57
95th perc.	0.10	0.22	0.22

Table 1. von Mises strain on septum H2a&H2b when subject to crash during diastole and systole.

4. Conclusions

This model is a first step toward numerically simulating a full beating heart during a car crash. The concentration of strain on the septum during the crash could induce a post-traumatic VSD.

Acknowledgments

We thank the iSafe project of the LBA and its team (CBR, MB, PJA) for the data provided.

References

1. Pruitt CM, Titus MO. Ventricular Septal Defect Secondary to a Unique Mechanism of Blunt Trauma: A Case Report. Pediatric Emergency Care. janv 2007;23(1):31-2.

2. Pierli C. Unusual localisation of a ventricular septal defect following blunt chest trauma. Heart. 1 juill 2001;86(1):6e-6.

3. Tochii M, Watanuki H, Sugiyama K, Futamura Y, Ishikawa H, Matsuyama K. Ventricular septal rupture after blunt chest trauma: a case report. surg case rep. déc 2022;8(1):94.

4. Wei W, Kahn CJF, Behr M. Fluid–structure interaction simulation of aortic blood flow by ventricular beating: a preliminary model for blunt aortic injuries in vehicle crashes. International Journal of Crashworthiness. 3 mai 2020;25(3):299-306.

***Corresponding author. Email: dorian.sweidy@univ-eiffel.fr**

Investigation the use of magnetic materials to align nerve fibres in severed nerves

Maz Aljunaydi1, Gillian Pearce2, Philip Langley1
School of Biomedical Engineering, Hull University, HU6 7RX
School of Engineering and Physical Sciences, Aston University, B4 7ET

1. Introduction

Peripheral nerve injuries are common in trauma, affecting 2.8% of patients with multiple injuries (Benga et al., 2017). While nerves attempt self-repair, surgical intervention is often necessary to reconnect the damaged sections (Sebastin, 2013). Advanced repair techniques, such as nerve grafts, growth factors, scaffolds, and electrical stimulation, have been developed, though challenges like revascularisation, donor site selection, and tension management remain (Javeed et al., 2021). Studies by researchers such as Bhandari (2019) and Song et al. (2021) highlight the importance of proper nerve bundle alignment for effective repair.

2. Methods

Our research explores the use of magnetic materials inserted into the fatty tissues surrounding the fascicular bundles within peripheral nerves. To assess nerve alignment with these materials in situ, we use a simple electrical circuit that allows current flow when proper alignment is achieved.

We modelled the nerve using Polycraft T15 silicone rubber, with one model replicating the human sciatic nerve, the thickest nerve in the body at about 20 mm in diameter (Davis et al., 2021). Neodymium magnets were chosen for their strength and lightweight properties (Knoepfel et al., 2004). We compared the use of magnetic materials for aligning the opposing sections of the nerve model to the epineural nerve repair method.

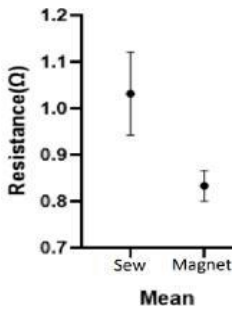

Figure 1 shows the resistance vs Sew and magnet repair method.

3. Results and Discussion

Our findings indicated that the use of magnetic materials resulted in better nerve alignment compared to epineural nerve repair. This suggests that magnetic materials have the potential to aid in nerve repair. Figure 1. Resistance in Ohms (mean values in several readings) measured for conduction of current through the nerve when magnetic materials are used in the classic suturing technique for nerves (using our nerve model).

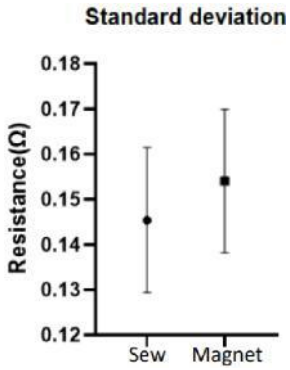

Figure 2 shows the resistance vs Sew and magnet repair method

4. Conclusions

Our research suggests that magnets resulted in better nerve alignment compared to traditional repair methods. Magnetic materials show promise in aiding nerve repair, especially when combined with scaffolds, magnetic gradients, or external magnetic fields. Neodymium magnets proved effective, but further research is needed to optimise their field strength and composition.

Although our study used a synthetic nerve model, the results present a novel approach to nerve repair with magnetic materials, warranting further investigation.

References

Benga, Andreea, et al. Indian Journal of Plastic Surgery, 2017;
Bhandari, P.S. Journal of Clinical Orthopaedics and Trauma, 2019;
Davis, David, et al. “Sciatica.” 2021;
Javeed, Saad, et al. Interdisciplinary Neurosurgery, 2021;
Knoepfel, H. and Kurz, J., 2004. Handbook of Magnetism and Advanced Magnetic Materials. John Wiley & Sons.
Lavdas, A.A, and R Matsas. ScienceDirect Topics 2014;
Sebastin, Sandeep J., et al. The Journal of Hand Surgery 2013;
Song, Shang, et al. Biomaterials, 2021

***corresponding author: gpearce2011@gmail.com**

Improving the care of patients with severe lower limb trauma using a Bayesian Network

T. Cloake[1,2,*], A. Daneshkhah[2], J. Ward[1], C. Neal-Sturgess[3], J. Hardwicke[2], C. Bastien[2]

[1] *University Hospitals Coventry and Warwickshire NHS Trust*

[2] *Coventry University*

[2] *University of Birmingham*

Keywords*:* open fracture; limb salvage; machine learning

1. Introduction

Open fractures of the lower limb are devastating injuries that are associated with considerable morbidity and mortality. The pivotal decision when treating severe lower limb trauma is between limb reconstruction and amputation, and it relies upon a detailed understanding of the interaction between a diverse range of variables. Contemporary analysis of outcome data suggests that making a timely and accurate decision about managing open limb fractures conveys significant clinical and functional benefits. Several injury classification and severity scores exist to aid clinicians in decision-making; however, they are limited by unacceptable interobserver variability, heterogeneity within classes, and delayed (post-debridement) application. Recent advances in computational engineering have led to the development of sophisticated algorithms capable of harnessing patterns in datasets. Machine learning (ML) methods have shown promise as the basis of modern clinical decision-support tools. This work aims to improve the care of patients with open lower limb fractures by developing an ML clinical decision support tool that can be applied at the first injury assessment.

2. Methods

A clinical dataset was populated through a local database search; the primary outcome of interest was limb salvage. Model input variables were defined through a systematic literature review, an expert opinion panel and a data-driven feature selection algorithm. A Bayesian network (BN) structure was derived from the dataset and refined by incorporating subject experts' knowledge. The predictive performance of the BN was evaluated using cross-validation performance measures and the area under the curve (AUC). The BN's predictions were compared to current injury scores.

3. Results and Discussion

Results of the hybridised variable selection identified ten influential factors for predicting limb salvage. The clinical dataset was populated with 481 cases with an overall limb salvage rate of 94%. A pedestrian trauma reconstruction model was developed, but a lack of detailed accident data limited its application. A Bayesian Network (BN) was selected as the superior model with an accuracy of 97% and an area under the curve (AUC) of 0.823. The BN's performance offered improved accuracy in outcome prediction compared to the Mangled Extremity Severity Score (92%) and Orthopaedic Trauma Association Open Fracture Classification (96%).

4. Conclusions

This work concludes that the decision support tool permits accurate predictions for patient outcomes following severe lower limb trauma in advance of contemporary systems. Displaying the model as a network clearly demonstrates the relationships between the influential variables and provides an opportunity for causal inference. This innovative application of Bayesian theory has the potential to improve clinical and functional outcomes for patients with open lower limb fractures by supporting early treatment decision-making. Moreover, the model's predictions may facilitate communication with patients about the severity of their injuries. Further work is required to validate the model with external data and explore enhancing clinical injury datasets through trauma reconstruction.

***Corresponding author. Email: cloaket@uni.coventry.ac.uk**

Endorsed by

European Society of Biomechanics

The European Society of Biomechanics (ESB) was founded at a meeting of 20 scientists from 11 countries in Brussels on May 21, 1976. Biomechanics is defined as "The study of forces acting on and generated within a body and of the effects of these forces on the tissues, fluids or materials used for diagnosis, treatment or research purposes". The primary goal of the ESB is ***"To encourage, foster, promote and develop research, progress and information concerning the science of Biomechanics"***.

https://esbiomech.org

Sponsored by

CELLBOND

Cellbond specialises in the design, development, and manufacture of passive safety testing products and equipment. This includes the full range of deformable aluminium crash test barriers, energy absorbers, crash test dummies, impactors, and test equipment.

Our global customer base includes vehicle manufacturers and leading organisations including EuroNCAP, IIHS, NHTSA and ARAI, plus test facilities and proving grounds such as Horiba-Mira and Millbrook. Cellbond is driven by innovation, introducing product initiatives and new technologies through close collaboration with our customers.

In 2023, we celebrated our 35-year anniversary, and in 2024, Cellbond Japan reached its 10-year milestone, and Cellbond Korea was launched.

www.cellbond.com

Oasys
LS-DYNA ENVIRONMENT

Oasys Ltd is the software house of Arup, a global firm of designers, consultants and experts dedicated to sustainable development. We have been working with the developers of LS-DYNA, for over thirty years, using the software for our own consulting work as well as distributing to clients in the UK, Europe, Asia, and North America. Our in-depth knowledge has enabled us to create the Oasys LS-DYNA Environment – tailored tools to prepare models, interpret results, and share solutions. They are at the leading edge of pre- and post-processing software and are used by LS-DYNA customers worldwide. Our suite of products plays a pivotal role in enabling our clients to deliver projects that might not otherwise be achievable without complex analysis. With operations globally, our team of experts' support users to bring products and ideas to life.

LS-DYNA Software | Oasys Suite

dyna.support@arup.com

ALTAIR

Altair is a global leader in computational intelligence that provides software and cloud solutions in simulation, high-performance computing (HPC), data analytics, and AI. Altair enables organizations across all industries to compete more effectively and drive smarter decisions in an increasingly connected world – all while creating a greener, more sustainable future. To learn more, please visit

www.altair.com

Since 2022, Altair Radioss - an industry-proven finite element analysis (FEA) dynamic simulation code – is available as open-source technology under the name OpenRadioss. To learn more visit

www.openradioss.org

JSOL

JSOL supports industries with state-of-the-art simulation technology. Industries are facing intensified market competition, grappling with challenges that range from cost and quality to safety, environmental concerns, and reduced time-to-market. Recently, societal focus has shifted toward the policies and ethics of product development within companies, emphasizing not only product performance but also designs that prioritize safety and environmental considerations. To address these challenges, the role of CAE (Computer-Aided Engineering) in product development is becoming increasingly vital. JSOL offers a wide range of solutions in the CAE field, including software development, technical support, and consulting services.

www.jsol-cae.com/en/

Proceedings SimBio-M 2024

Cottingham Road,
Kingston upon Hull
HU6 7RX, UK
https://www.hull.ac.uk/

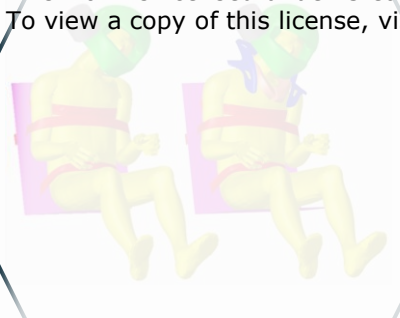

University of Hull

BEng/MEng Biomedical Engineering Course

MSc Biomedical Engineering course

Coventry University

Mechanical Engineering MEng/BEng (Hons)

Coventry University Masters Degrees in Engineering

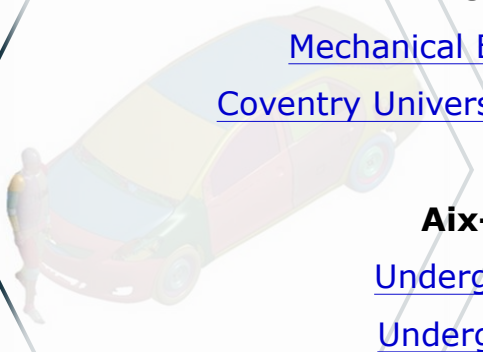

Aix-Marseille Université

Undergraduate course in English

Undergraduate course in French

Masters Degree Programs

Université Gustave Eiffel

Courses at Université Gustave Eiffel

Applications Bachelors and Masters

ISBN - 978-1-906422-44-8